Development of the ceramic dispersion strengthened 316L steel composites

Haroune Rachid Ben Zine

Ph. D. dissertation

Supervisors:

Dr. Csaba Balázsi
Dr. Katalin Balázsi

Óbudai Egyetem

Doctoral School of Materials
Science and Technology
Óbuda University

Thin Film Physics Department
Institute of Technical Physics and Materials Science
Centre for Energy Research, Hungarian Academy of Sciences

Budapest, 2019

Acknowledgement

Firstly,

I would like to thank and show my sincere gratitude to my supervisors **Dr. Csaba Balázsi** and **Dr. Katalin Balázsi,** whom I always felt and consider them as my family due to their continuous support, motivation and specially patience and understanding, where they believed in me when I even lost hope in myself, honestly, I wouldn't be here today without their help-at least not at this time of my life. Their guidance showed me the right path during the research work, I will never be able to thank them enough for what they did for me.

I would like to thank **Dr. Judit Borsa** for her help and support during my Ph.D. studies. Also, I thank all my teachers for their valuable efforts to enlarge my scientific knowledge.

I thank **Dr. Ákos Horváth** for his support and motivation specially during the last period of my PhD work.

I would like to thank **Dr. Béla Pécz** for his cooperation and support by providing me with access to all needed facilities in the MFA.

I thank **Prof. Dr. Filiz Cinar Sahin** for her collaboration and help in sintering the composites.

I thank **Dr. Zsolt Czigány** for his collaboration and help in TEM investigations.

I thank **Dr. Zsolt Horváth Endre** for his collaboration and help in XRD investigations.

I thank **Dr. Zsolt Fogarassy** for his help in the interpretation of TEM results and his support during my PhD

I am grateful to all dear colleagues in MTA EK MFA for their collaboration and help, specially **Viktor Varga**, **Andor Kovács**, **Levente Illés**, **Sándor Gurbán, Andrea Jakab** and **Erzsébet Dódony.**

Table of Content

List of Acronyms

316L	Low carbon stainless steel
ASP	Active Screen Plasma
CDS	Ceramic Dispersion Strengthened
DC	Direct Current
DLD	Direct Laser Deposition
DM	Digital Microscope
F/M	Ferritic-Martensitic
FSP	Friction Stir Process
GNG	Gradient Nano-Grained
HIP	Hot Isostatic Pressing
HP DLD	High-Power Direct Laser Deposition
HPT	High-Pressure Torsion
HV	Vickers hardness
LTC	Low Temperature Carburizing
MA	Mechanical alloying
MM	Mechanical milling
ODS	Oxide dispersion strengthened steels
PCS	Poly-Carbo-Silane
PIM	Powder Injection Modeling
Si_3N_4	Silicon nitride
SiC	Silicon carbide
SLM	Selective Laser Melting
SMRT	Surface Mechanical Rolling Treatment
SPS	Spark Plasma Sintering
SS	Stainless Steel
TEM	Transmission Electron Microscopy
UCFT	Ultrasonic Cold Forging Technology
UF	Ultrafine
UTS	Ultimate Tensile Strength
Y_2O_3	Yttria
ρ	Density

1. Introduction and motivation

316L based oxide dispersion strengthened steels have attracted attention for advanced nuclear applications such as fast and fusion reactors as other commercially available materials. These materials can be used in harsh environments at high neutron doses and elevated temperatures [1]. Japan, Europe and the United States have developed this steel material for fusion and fission nuclear applications as well [2, 3]. Novel designs for future generation fusion reactors have demanding requirements for the structural materials. A new class of Oxide dispersion strengthened steels (ODS) materials which are currently being developed have a high chance of meeting these requirements [4]. Nanostructured ferritic, martensitic or austenitic ODS alloys are ideal candidates for high temperature applications such as high temperature heat exchangers or nuclear power plants [5–9].

The production of the 316L based ODS steels involves many technological processes. The mechanical alloying, degassing, hot extrusion, and heat treatments are the most used technological methods. It was shown that powder metallurgy process helped the dispersion of the big oxide particle´s agglomerations during conventional casting processes [10].

The goal of my PhD work was the study of the effect of milling parameters and different submicron sized ceramics (Si_3N_4, SiC, Y_2O_3) addition on the structural, mechanical and tribological properties of final 316L based composites prepared by attrition milling and spark plasma sintering. These results demonstrated that the small amount of ceramic addition have influence on the final properties of composites and open the new routes for various novel applications.

2. Literature review

In this chapter, the fundamental knowledge on 316L based oxide dispersion strengthened steels are briefly reviewed with focus on preparation methods and properties of final material. Nowadays, powder mixing, mechanical alloying, degassing, canning, hot extrusion or heat treatments are most used technological methods for the production of the 316L based ODS steels.

The stainless steels remain not easily replaceable taking into consideration their high mechanical characteristic (strength, hardness and impact resistance) what their offer to be used in significant fields such as the nuclear power, the storage of the chemical products.

2.1. 316L austenitic steel (316L)

The 316L steel is an austenitic chromium-nickel stainless steel where the 2-3 % molybdenum content increases the corrosion resistance and increases the strength at high temperatures. The "L" stands for "low carbon content" which is under 0.03 %, this increase its resistance to carbides precipitation and improves the corrosion resistance specially after welding. The 316L stainless steel has a density of 8000 kg/m^3, an elastic modulus of 193 GPa and a tensile strength 485 MPa [11]. 316L austenitic stainless steel (316L SS) is generally employed as a structural material in numerous industrial applications such as a transport or energy production. 316L SS has attracted attention due to its good mechanical properties at high temperatures, good corrosion resistance, and good weldability, which can be an effective solution for several industrial applications [12–14]. The Fig. 2.1 shows the typical structure of 316L steel, where the presence of dislocations and some twins is noticeable in the equiaxed grains of this alloy.

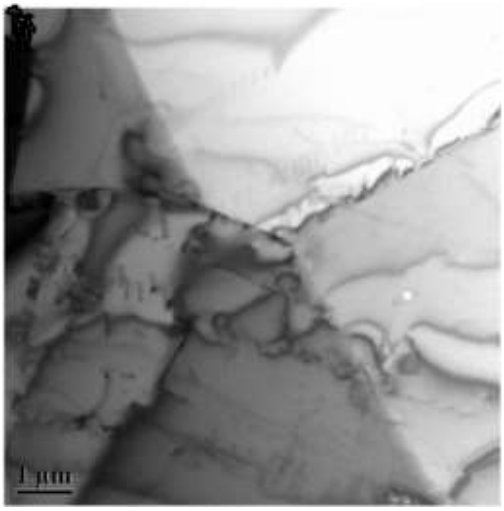

Fig. 2.1. *TEM image of a 316L stainless steel [15].*

2.2. Oxide dispersion strengthened steels (ODS)

The ODS steels are designed to withstand extreme working conditions such as high temperatures (above 700 C°), high pressure, high neutron radiations. The idea behind the ODS steels is to sustain or slow down the deformation/degradation of steel under the mentioned conditions by blocking/pinning the dislocations and grain boundaries mobility/migration. Employing nanoparticles enriched with oxygen have been found to be promising solution unlike the conventional employment of precipitates in the steel matrix, which degrades the mechanical properties of steel furthermore at high irradiations and high temperatures because of their relatively large size [16]. Different type of ODS steels are being experimentally investigated for better understanding of the formation process of the oxygen enriched nanosized particles and their interaction with dislocations [16]. The mostly investigated ODS steels are the austenitic and the ferritic/martensitic (F/M) steels.

The Fig. 2.2. shows an example of typical microstructure of an austenitic ODS steel. The nanosized ceramic particles are dispersed homogenously within the steel matrix and along the grain boundaries.

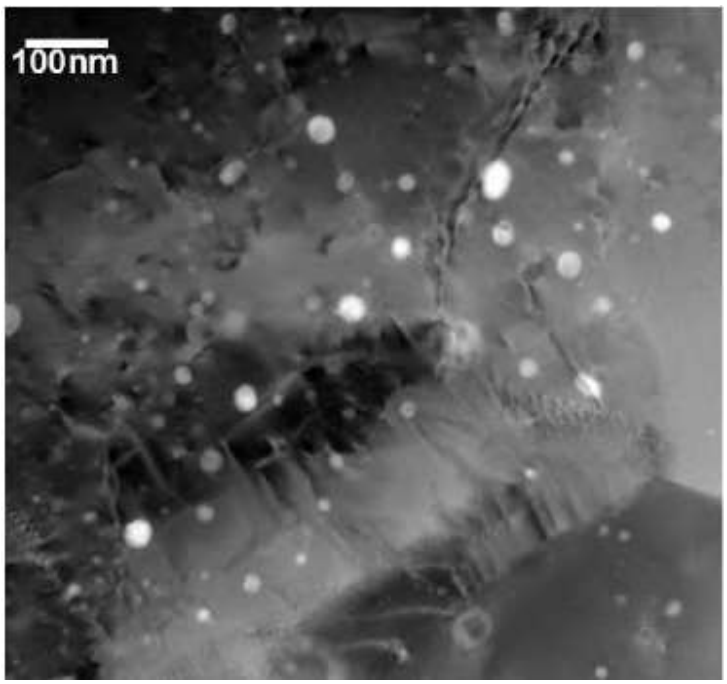

Fig. 2.2. *STEM image showing microstructure of ODS stainless steel [16].*

Nowadays, the investigation of the employment of ceramic nitride, carbide nanosized particles instead of the ceramic oxides particles has a great interest [17].

2.3. Preparation methods of 316L based ODS

The manufacturing route primarily determines the materials properties. Some previous works studied the development of 316L stainless steel powders by using different techniques such as selective laser melting (SLM), hot isostatic pressing (HIP), and high-power direct laser deposition (HP DLD) with large size and excellent mechanical properties [18]. On the other hand, the mechanical alloying (MA) is attracting for researchers due to its unique advantages and large scale availability. Ni-based oxide dispersion strengthened (ODS) steels have been developed by this technique in early 1960s [19]. In their study about the effect of surface enriched chromium and grain refinement by ball milling on corrosion resistance of 316L stainless steel *L. Jinlong et al.* showed the possibility to enrich grain's surface of the 316L stainless steel during the ball milling process, which improved the corrosion resistance by cancelling the negative influence of the α-martensite [20]. *N. Kurgan et al.* founded that cold pressing under 800 MPa and sintering at 1300°C for 30 minutes in nitrogen atmosphere was more suitable for the 316L powders [21].

Spark plasma sintering (SPS) has been successfully used for the densification of a wide variety of materials (ceramic [22, 23], metals and alloys [24, 25], polymer and composites [26, 27]). *C. Balázsi et al.* realized as first the nanostructured 316L steel compacts and austenitic stainless steel based composites by spark plasma sintering (SPS) [28].

2.4. Structural and mechanical properties of 316L based ODS

N. Jahanzeb et al. studied the effect of the microstructure on the hardness heterogenity of the dissimilar metal joints between 316L stainless steel and hot rolled steel (SS400). It was found that the strain distribution was locally heterogeneous at higher strains due to the unequal patterns of the γ phase transformation to α' in 316L stainless steel. The deformation twinning was the dominant mechanism for the 316L during uniaxial tension [29].

80% compressive strain can improve the 316L´s hardness with 150% due to the grain refinement and the massive creation of twin boundaries and dislocations [30]. *J. Gubicza et al.* showed that 10 turns of High-Pressure Torsion (HPT) of a ~ 42 μm duplex coarse-grained microstructure result in ultrafine grain size reduced of ~ 45 nm. During this process, the ɣ phase transformed to ε-martensite then to the α′-martensite. This martensitic phase showed exceptional high dislocations density [31].

M. Ziętala et al. studied the properties of the 316L steel fabricated by laser engineering net shaping (LENS) [32]. The fully dense samples without structural defects have been obtained. The samples had a higher content of Mo and Cr in the grain boundaries. A lower Ni content has been observed, which allowed the formation of the delta ferrite on the subgrain boundaries. The δ-FeCr phase has been observed [32]. This study showed better mechanical and corrosion properties due to the formation of the ferrite phase and the formation of the passive oxide layer caused by the presence of the chromium in the bulk. The structural characterization showed a heterogeneous microstructure with elongated austenitic fine grains oriented along the thermocapillary convection

direction. This heterogeneous structure of the 316L steel fabricated by LENS had a clear impact on the mechanical properties.

The evolution of the structure during the direct laser deposition (DLD) was influenced by the time interval between deposited layers. In the case of long local time intervals, fine microstructures were obtained due to the higher cooling rates. The reduced laser penetration depths resulted in widespread porosity and less integral metallurgical bonds in locations further upward from the build plate. In the case of the short time intervals, which increased the bulk temperature, samples with coarser structure have been obtained due to lower cooling rates [33]. *Zhong et al*. studied 316L samples fabricated by electron beam melting for nuclear fusion applications [34]. In their study, the structural characterization showed a mixture of irregular shaped submicron sized structure, solidified melt pools and columnar grains. Precipitates enriched in Cr and Mo have been observed at the grain boundaries, while no sign of element segregation was shown at the sub-grain boundaries.

The porosity in the 316L samples made by powder bed laser fusion is affected by the laser energy density; at high laser energy density, the pores are rounded and randomly distributed, unlike in the case of low laser energy density where the pores are irregular and highly directional [31]. Over 1‑5% porosity range angular porosity was found to reduce the Young's modulus by 5% more than rounded porosity [35].

M. Hajian et al. studied the structural and mechanical properties of friction stir processed 316L. They showed that the friction stir process (FSP) exhibited ultrafine grained structures at relatively low rotational speeds [36]. It has been observed that the grain structure evolution of the 316L samples made by FSP was mainly dominated by discontinuous dynamic recrystallization. A significant reduction of twin boundaries fraction in the stir zone was observed in comparison to the base metal.

316L prepared by selective laser melting (SLM) exhibited good mechanical properties at high temperatures [37]. This preparation improved the strength of the 316L by the formation of complex microstructure with large angle boundaries, a combination of brittle and ductile fracturing behavior has been observed.

One of the novel preparation technique is the Spark Plasma Sintering (SPS) technique. In this technique, the current passes through the lowest resistance areas which can result in heterogeneous sintering of powder samples [38]. *A. B. Kale et al*. studied the deformation and fracture behaviour of 316L stainless steels fabricated by SPS technique under uniaxial tension and showed the high densities of sintered materials. However, the samples were not sintered homogeneously, therefore, two different fracturing mechanisms have been observed. Firstly, ductile fracture in the fully sintered regions, secondly powder/matrix interface decohesion in the partially sintered regions [39]. The investigations demonstrated that the fracture was started from the partially sintered regions [39].

C. Keller et al. studied the influence of SPS conditions on the sintering and functional properties of an ultra-fine grained 316L stainless steel obtained from ball-milled powder [40]. The study showed that the use of powder metallurgy technology and the SPS is suitable for the elaboration

of AISI SS 316L with ultrafine (UF) grains size. High density values can be obtained by SPS. The elaboration of 316L alloy by ball milling and SPS increases the formation of chromium carbides on the sample surface, also it increases the formation of oxides in the material. These oxides can represent around 10% volume fraction [40]. The sintered samples by SPS has a homogeneous microstructure without preferential grain orientation. The refinement of the grain size increases strongly the samples hardness.

Not only the sintering, the milling process had an influence to the final structure of the materials. Homogeneous interfaces with less pores have been found after 5 hours milling time. Longer milling time leads to less homogenous joint distribution and it was not optimal for obtaining graded interfaces because more micro-cracks, holes and intermetallics were created [41]. The selective laser melting (SLM) process provides considerably finer microstructure than the conventionally manufacturing processes [42]. SLM densified specimens have a fine-grained microstructure with elongated grains in build-up direction, but no preferred crystallographic orientation, such as in cast and HIP conditions [43]. During SLM process, the produced samples showed different properties in the case of using different combinations of processing parameters even if these different combinations are presenting similar energy density [44]. *J. D. Majumdar et al*. confirmed that the hardness and the wear resistance of the AISI 316L may be improved by dispersion of the SiC in the matrix, the precipitation of the Cr_2C_3 and the Fe_2Si or by the grain refinement [45].

F. Akhtar et al. showed that the addition of more than 2 wt% Si_3N_4 to the stainless steel resulted in a decrease in the sintered density and tensile strength values [17]. The Si_3N_4 dissociated to silicon and nitrogen which gives the nitrogen much higher content than its solubility limit in steel and the nitrogen diffuses out of the matrix leaving pores. Near full densified 316L with 5 wt% Si_3N_4 has been achieved by liquid phase sintering using high temperature vacuum furnace. The study showed that the Si_3N_4 was not stable above 2 wt% and it was dissolved in the 316L matrix. The dissociation of much higher amount of Si_3N_4 caused the decreasing of the density due to the diffusion of nitrogen out of the steel matrix [17].

Many researchers studied the effect of yttria (Y_2O_3) addition on the structural and mechanical properties of the steel where it was found that ultrafine yttria particles can improve significantly the hardness of steel, also its strength at high temperatures [46]. Composites with small particles exhibit higher strength because of their higher joining zone which is an effective heat source [47]. The interaction between the yttria and the steel matrix increases the diffusion of this last which increases the densification of steel. It was confirmed that 12 wt% or higher content of yttria will not improve the densification due to the agglomeration of yttria [48]. Oxides with Y and Cr are influencing the porosity having a direct effect on the oxidation rate in steel composites [49]. A composite composition with high content of yttria nanosized particles results in a delay in the 316L sintering. The yttria nanoparticle´s agglomerates are created at sintering temperature bellow 1300°C [50]. The oxide phase can enhance the upper temperature limit in mechanical creep strength with 100 C° at least [51]. *R. Lindau et al.* studied the effect of 0.3 wt% and 0.5 wt% yttria on the mechanical properties of the EUROFER 97 at high temperatures. It was found that the yttria

improved the yield strength, ductility and the creep strength as well [52]. *S.-W. Baek et al.* studied the hydrogen susceptibility of nanosized Y_2O_3 dispersed strengthened 316L austenitic steel, they found that hydrogen didn't affect the yield strength and the elastic modulus of the 316L [53]. *P. Hutař et al.* studied the small fatigue crack propagation in Y_2O_3 strengthened steels [54]. They found that it has insignificant effect on the small fatigue crack propagation. *P. K. Kumar et al.* investigated the effect of Y_2O_3 and ZrO_2 on the microstructure and mechanical properties of nanostructured ODS [55]. The hot pressed Y_2O_3 ODS steels showed higher tensile strength (UTS) comparing to the ZrO_2 containing ODS. ODS/Y_2O_3 showed even higher tensile strength values compared with ODS/ZrO_2. The yttria content under 0.6 wt% improves the oxidation resistance by forming a stable oxide scale and improving the adhesion, while higher amounts of yttria results in segregation of this last. The yttria addition tends to decrease the bending strength and the hardness of the steel [56].

A. J. London et al. developed ODS alloys (Fe / 0.3 wt% Y_2O_3, Fe / 0.2 wt% Ti / 0.3wt% Y_2O_3 and Fe /14 wt% Cr /0.2 wt% Ti / 0.3 wt% Y_2O_3) prepared by ball milling and then hot extrusion to find the effect of Ti and Cr on the size, distribution, crystal structure and composition of the nanosized oxide particles. The median particle sizes were 9.6 nm, 7.7 nm and 3.7 nm for the Fe /Y_2O_3, Fe/Ti/Y_2O_3 and Fe/Cr/Ti/Y_2O_3 alloys, respectively. The presence of Ti resulted in a significant reduction in oxide particle diameter and the addition of Cr gave a further reduction in size [57]. Fe/25 wt% Y_2O_3 composite powders fabricated by mechanical milling (MM). The milling periods of 4, 8, 12, 24, 36, and 48h, respectively were applied for milling of the Fe powders with average size 100 μm and Y_2O_3 nanoparticles in an argon atmosphere. The experimental results showed that the crystalline size of MM powders decreased with the increasing of the milling time. All elements distributed homogenously after 48h milling time. The lattice constant of the matrix α-Fe kept constant with the milling time, and no solid solution took place during MM process [58]. Novel sintering techniques have been used for preparation of ODS. A Fe/14 wt% Cr/ 0.4 wt% Ti and 0.25 wt% Y_2O_3 alloy was fabricated by mechanical alloying and subsequently consolidated by SPS. The densification of these alloys significantly improved with an increase in the sintering temperature. Structural observations revealed that SPS-sintered at 1150 °C under 50 MPa for 5 min. had a high density (99.6%), the random grains orientation and a bimodal grain size distribution (< 500 nm and 1–20 μm) [59].

H. Oka et al. studied the effect of milling process and alloying additions on oxide particle dispersion in austenitic stainless steel in order to understand the minor alloying elements on the dispersoids distribution [60]. They found that 6 hours are enough to disperse the Y_2O_3 in the steel matrix, also it was found that the usage of 0.2 – 0.3 wt% Zr or 0.6 wt% Hf increased the hardness of the steel by improving the finer oxides distribution in the matrix. Ball milling can be used to obtain nanosized grains, this refinement of the grains size increased the composites hardness despite the formation of the oxides.

F. Akhtar et al. improved the sintering densification of the 316L by adding $MoSi_2$. The investigations showed that the Mo and Si segregated at the grain boundaries and the excess formed separate phases. The best mechanical properties were found for samples with 5 wt% $MoSi_2$ [61].

The potential of the pitting corrosion has been decreased due to the presence of submicronic grains [62]. *B.Al Mangour et al.* investigated the in situ formation of TiC particle reinforced stainless steel matrix nanocomposites during ball milling up to 35 hours [63]. During prolonged mechanical alloying the grains are just flattened after 10h, become larger (coarsening) after up to 24h and the grains refinement took place at the end of the process. The final powder mixture showed the homogeneously dispersed TiC particles in steel matrix. It has been found that 5 hours of milling provides better interface in the case of 316L-50 tungsten (W) comparing to 10 hours milling. The interface formation in the case of 316L-50W/W showed uncompleted reaction which is related to the presence of residual pores. The excessive milling decreases the joint homogeneity and it was insufficient for graded interfaces [64, 65]. The volume fraction of tungsten (W) in the 316L matrix was the main factor for improving the hardness of 316L-W composites [65].

2.5. Tribological properties of 316L based ODS

Friction is the natural response of all tribosystems [66]. The fabrication process has great influence on the microstructure. This last property has great and direct influence on the tribological properties of the material. *J. Menga et al.* investigated the tribological properties of the 316L made by powder injection modeling (PIM) sliding against AISI 52100 steel at low loads [67]. The formation of carbide phase during the sintering in vacuum improved the tribological properties of the stainless steel, where a lower wear rate and friction coefficient have been recorded. The wear mechanism has been influenced by a combination of the formation of tribolayer and various iron oxides. In case of the sintered samples in hydrogen, severe worn marks have been observed on the surface [67]. *F. Bartolomeu et al.* found that the 316L stainless steel made by SLM show better tribological properties in comparison to the conventional casting and hot pressing (HP) because of its finer microstructure [68]. For this, SLM is a promising process to produce 316L SS with improved wear resistance. *Y. Li et al.* studied the tribological behavior of the oxynitrided austenitic stainless steel produced by Active Screen Plasma (ASP) [69]. They have found 95% decrease of the wear rate in the case of the oxinitrided samples, where abrasion marks and oxidation have been slightly observed on the worn surface. In the case of untreated samples, a plastic deformation and intense adhesive wear have been observed. *D. Guan et. al.* investigated the polycarbosilane (PCS) reinforced 316L made by SPS [70]. In their study the 3% PCS samples show the best wear resistance, where 86% decrease of the wear rate have been observed comparing to the pure 316L. In the same time higher microhardness values have been observed with the increase of PCS content. *P.F. Wang et al.* investigated the tribological properties of a gradient nanosized grained (GNG) layer fabricated by Surface Mechanical Rolling Treatment (SMRT) on a 316L [71]. In the both cases, the sliding tests have been performed at room temperature in dry and oil lubricated conditions and confirmed that the GNG layer enhanced the wear resistance in both cases. *Y. Wang et al.* studied the effect of the surface nanocrystallization on tribological properties of 316L stainless steel by ultrasonic cold forging technology (UCFT) under different lubrication conditions

[72]. It has been found that the low friction and antiwear performances of samples are influenced by the synergistic effects of the surface nanocrystallization. *F. Rotundo et al.* investigated the low temperature carburizing (LTC) influence on dry sliding tribological behavior of the 316L stainless steel at high and room temperature [73]. The LTC increased the hardness of the 316L significantly which in turn improved the tribological properties of the steel when tested at room temperature. In the case of high temperature testing, the tribological behavior of steel became similar to the untreated steels. This fact can be explained by the structural changes in the carburized layer due the high temperature combined with friction heating, and the formation of an oxide protective layer in the case of non-treated 316L [73].

3. Experimental methods

The attrition milling and spark plasma sintering are in the bases of this Ph.D work, the same milling and sintering parameters have been used to produce all of the studied composites.

3.1. Attrition milling

The attrition milling is the process of grinding materials using a mill with agitated media (balls) in order to reach very fine grinding. This last is a result of a combination of shearing and impact forces generated during the milling process. The agitator rotates at high speed creating irregular movement of the grinding media, resulted the impact between the agitator and the grinding balls or also by the impact of balls with each other. The irregular movement of the grinding media cause the shearing force, where the balls are rotating in different directions and speeds (Fig. 3.1) [74].

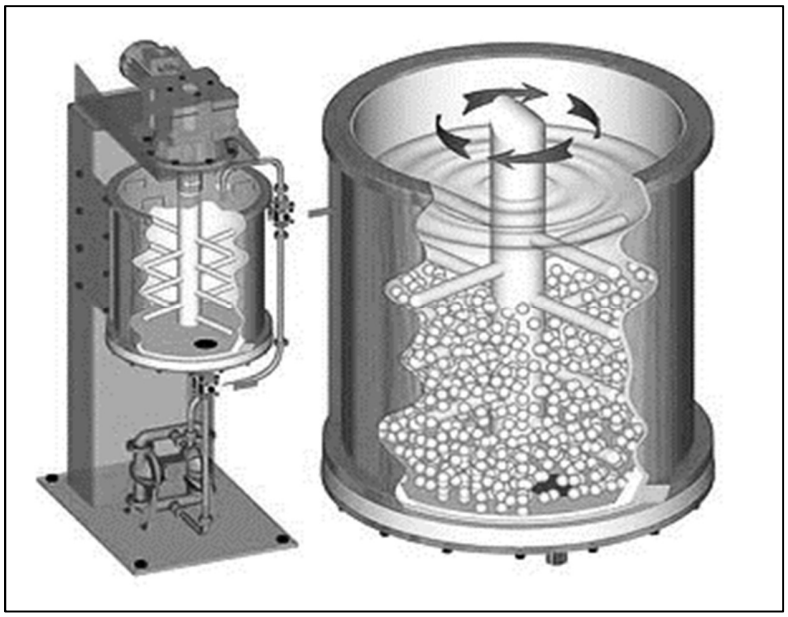

Fig. 3.1*. Schematic view of an attrition milling process [75].*

The attritors can be categorized as follow [74]:

- dry grind attritors
- wet grind attritors
- regular speed attritors
- high speed attritors

Some of the main features of the attritor mills [74]:

- jacketed grinding tanks for cooling or heating usage
- sealed covers for controlling the milling atmosphere
- cryogenic milling setup

3.2. Spark Plasma Sintering (SPS)

The Spark Plasma Sintering (SPS) is a rapid sintering method for production of homogeneous nanostructures and high-density composites. It is also known as the Pulsed Electric Current Sintering (PECS) [76]. The principle of the SPS is based on the very high heating and cooling rates of the composite/material in order to prevent grain growth and suppressed powder decomposition, for this, uniaxial pressure and a pulsed electrical direct current (DC) under low atmospheric pressure are applied [77]. The pulsed current is passing through the powder and graphite die (Fig. 3.2) producing a heating power at the macroscopic level (from the graphite die) and at the microscopic scale (at the contact points of the powder particles). The material transfer path during the SPS process (Fig. 3.3), where the diffusion mechanisms are defined as follow:

1) vaporization and solidification,
2) volume diffusion,
3) surface diffusion,
4) grain boundary diffusion.

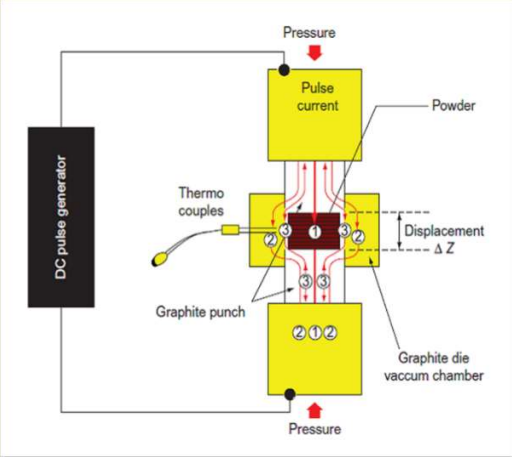

Fig. 3.2. *Schematic view of the SPS process [78].*

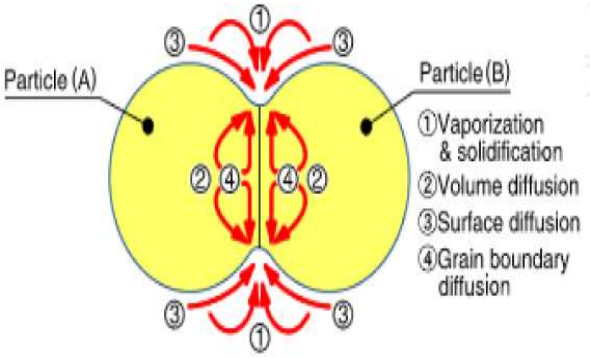

Fig. 3.3. *Material transfer during the SPS process [77].*

SPS process is attracting attention in the last two decades for showing successful sintering of nanosized composites which have been a big challenge using the conventional techniques such as Pressure Less Sintering (PLS) and Hot Pressing (HP) [79]. The SPS process is also used to elaborate high density nanostructural composites, thermo-electric semiconductors, fine ceramics, wear-resistant materials, functionally graded materials and biomaterials [80].

3.3. Density measurement

The density measurement of materials and composites is essential for optimizing the processing parameters [81]. Archimedes method is one of the most commonly used methods. The principle of Archimedes states that an object partially or totally immersed in fluid is lifted (buoyed) by an equal force to the weight of the displaced water. This can be used in the determination of the object density. The kind of fluid used during the measurement have a huge effect on the normalized sensitivity coefficients, also, the density measurements should be repeated multiple times for samples less than 10 g for better precision and reliability [82].

3.4. Vickers microhardness measurement

Microindentation is a commonly used technique for the determination of the materials hardness [83]. In the case of Vickers measurement, a small load is applied on a pyramid-shaped diamond (Fig. 3.4) indenter for a specific short period of time against the tested material in order to make an indentation on it. The diagonals of the indentation are used for the calculation of the microhardness values. The microhardness values are not affected by the indentation time but are affected by the indentation loads [84]. Measurements were performed in respect to the ISO-6507-1. Vickers microhardness was measured using the following formula:

$$HV = \frac{189 * F * 10^3}{d^2} \tag{3.1}$$

Where "F" is the applied load (N) and "d" is the diagonal's length (μm)

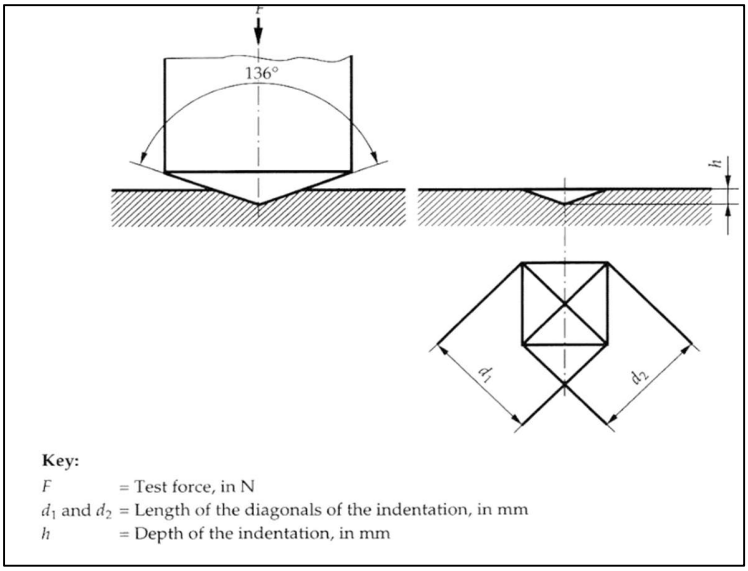

Fig 3.4. *Vickers microhardness indentation [85].*

3.5. Tribological measurements

Tribology is the study of friction, wear and lubrication of interacting surfaces in relative motion between room and high temperatures. This measurement is very essential for technologies with vast applications [86]. The testing of the tribological properties can be performed using a linear or circular relative motion modes. The pin-on-disc is circular relative motion arrangement (Fig. 3.5) where generally a hard material ball (ex: Si_3N_4, Al_2O_3) is fixed on the tip of a pin. The pin is pressed by a perpendicular load against the rotating disc which is holding the sample/material with adjustable shift from the rotation axis. The friction coefficient and the penetration depth are recorded automatically. The wear rate can be calculated using the wear volume or the weight loss. A decrease of the wear volume dependence on the sliding distance is noticeable below 1250 m, where the opposite is observed at distances above 1250 m as a result of the onset of the microchipping wear mechanism [87].

The wear rate is calculated using the following equation:

$$w_d = \frac{V}{F_n l} \tag{3.2}$$

Where, w_d is the wear rate, F_n is the Normal Force (N) , l is the Distance of the test (m)

The wear Volume is calculated using the following equation:

$$V_{disc} = 2\pi R[r^2 \sin^{-1}\left(\frac{d}{2r}\right) - \left(\frac{d}{4}\right)(4r^2 - d^2)^{\frac{1}{2}} \tag{3.3}$$

Where R is the wear track radius, d is the wear track width, r is the ball radius.

The tribometer has been calibrated before testing the composites.

Fig. 3.5. *Real photo of tribological measurement.*

3.6. 3-point bending test

The 3-point bending test is mechanical testing method used for the determination of the flexural stress, flexural strain, elasticity modulus of the material. The shape of tested sample is essential for result analysis, therefore, samples in the form of a cylindrical rods or rectangular bars are used for easy calculations. The tested sample is placed on two cylindrical rods, where a third rod transfers the applied load to the middle of the upper surface of the sample (Fig. 3.6) creating a stress peak at the middle of the sample causing it to flex, this creates three different strains and forces on different regions of the sample: 1) tensile strain on the convex side of the sample, 2) shear forces along the middle plane, 3) compressive strain on the concave side of the sample. In the case of the 3-point bending test, the flexural strength values are higher comparing to the 4-point bending test. This fact is resulted of the smaller involved zone in the 3-point bending test contains fewer defects [89]. In the used setup during the experimental work L_0 =20mm.

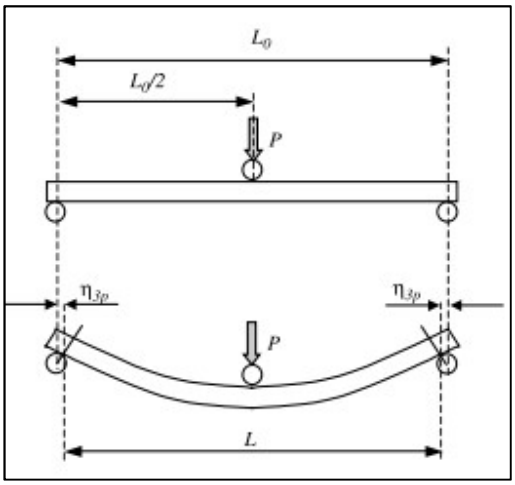

Fig. 3.6. *Schematic view of the 3-point bending test method [88].*

3.7. Scanning Electron Microscopy (SEM)

Scanning Electron Microscopy (SEM) is a characterization technique that employs the interaction between the specimen surface and the accelerated and focused electrons beam in order to generate topological images at the microscopical level. Basically, the SEM contains five main and essential components: 1- electron source, 2- column containing the electromagnetic lenses, 3- electron detectors, 4- sample chamber, 5- computer (Fig. 3.7). The interaction of the electron beam with the specimen results manly in the production of different type of electrons; secondary electrons, backscattered electrons, characteristic X-Ray, Auger electrons [90].

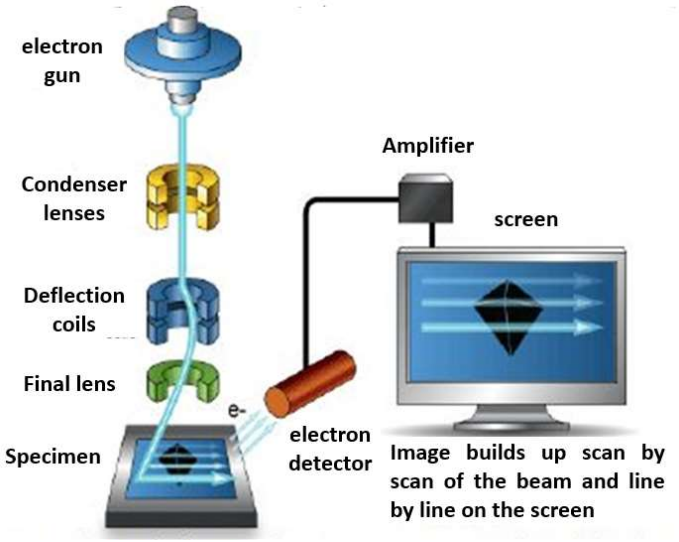

Fig. 3.7. *Method of SEM measurement [92].*

There are two main imaging modes in the SEM; secondary electrons imaging mode and the backscattered electrons imaging mode. Other imaging modes like "specimen-current image" and "voltage contrast" can be used in some cases [91]. Conductive samples don't require any preparation. The surface of sample must be clean to avoid contamination. In the case of insulating materials, a thin conductive layer (Au or Pt) can be deposited on the sample to eliminate the charging effect.

3.8. Energy Dispersive X-ray Spectroscopy (EDS)

The Energy Dispersive X-ray Spectroscopy (EDS) is an analytical technique based on the analysis of the X-ray generated from the interaction between the electron beam and the tested sample (Fig. 3.8). Two main types of X-rays are produced by the interaction of the electron beam with the sample; characteristic X-rays and continuum X-rays [93]. Usually EDS is mounted on SEM for qualitative or quantitative analysis and elemental mapping Overlaps of

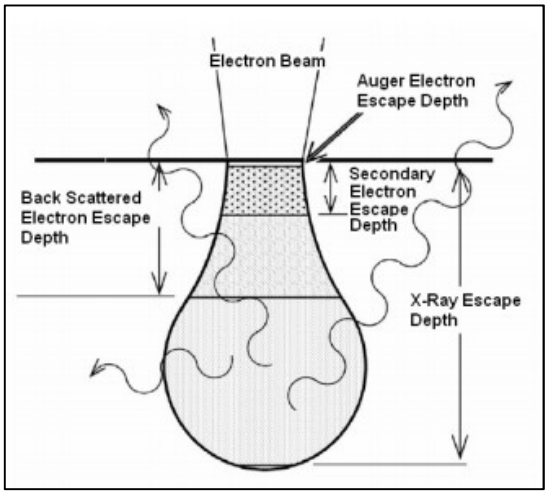

***Fig. 3.8**. The electron beam interaction volume [94].*

different elements may occur specially at high energies. The overlap makes the distinguish/ identification of the elements difficult, in this case, peak separation can be used or decision of considering only the elements with presence possibilities based on the sample elaboration history [95].

During this study, the Scanning Electron Microscope (SEM) LEO 1540 XB equipped with a Röntec Si(Li) EDS detector has been used to investigate all of the starting powders, milled composites, sintered composites and the broken surfaces after 3PB test. The SEM is equipped with InLens secondary electron detector, Eerhart-Thornley detector. The vacuum pressure inside SEM chamber was 10^{-7} mbar. The EDS measurements were performed using the Esprit 1.9 software. The samples were fixed on steel and aluminum sample holders using carbon tape.

3.9. X-Ray Diffraction (XRD)

The X-ray diffraction (XRD) is a nondestructive characterization technique employed in analyzing crystalline materials [96]. The XRD provides the information about the crystal structure, crystal phases and orientation or grain size. The generated X-rays by the cathode tube are filtered into a monochromatic radiation and concentrated, when Bragg's Law conditions are satisfied. A constructive interference is generated as a result of the interaction of the incident rays and the specimen. All the possible diffractions of the lattice should be detected by scanning the specimen through a range of 2θ angles, the diffractions are processed for the identification of the material by comparing the diffraction peaks with the standard reference patterns. The X-rays are generated as a result of an electron moving to lower energy orbit in order to fill a gap (Fig. 3.9a). The generated X-rays are divided into two different types: 1- characteristic X-rays, 2- continuum (Bremstrahlung) X-ray (Fig. 3.9b).

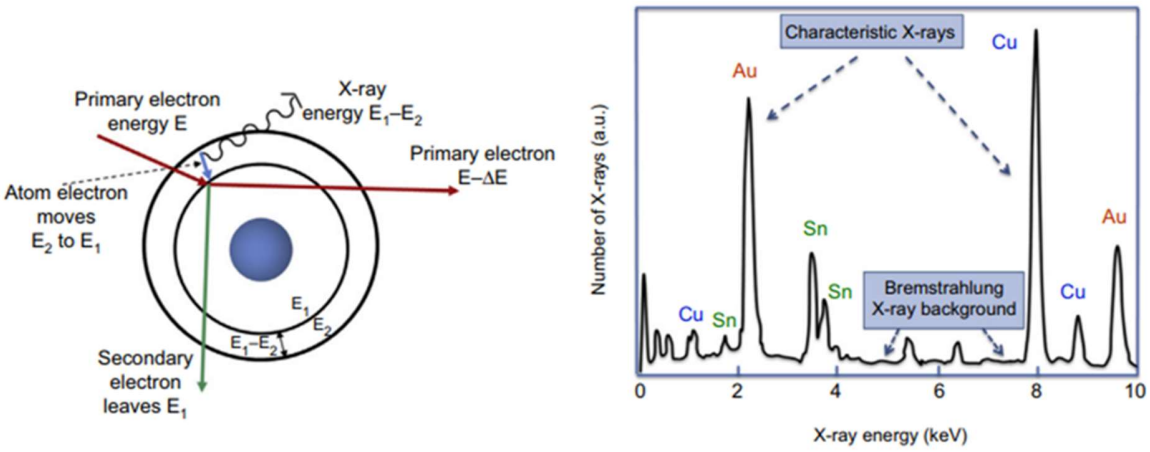

a) **b)**

Fig 3.9. *Electron-induced X-ray emission. a) characteristic X-ray generation, b) schematic of an energy dispersive X-ray (EDX) [97].*

The X-ray diffractometry (XRD) measurements were performed using a Bruker AXS D8 Discover diffractometer equipped with Göbel-mirror and a scintillation detector with Cu Ka radiation. The X-ray beam dimensions were 1 mm * 5 mm, the 2q step size was 0.02°, scan speed 0.5°/ min. We used the Diffrac.EVA program and the ICDD PDF database for phase identification.

3.10. Transmission Electron Microscopy (TEM)

The Transmission Electron Microscopy (TEM) is a very powerful characterization technique that uses a transmitted electron beam with high energy to acquire structural and chemical information about a specimen (Fig. 3.10). Special sample preparations are needed in order to make it supper-thin and transmittable by the electrons beam. The electron beam is generated using a cathode/anode system, where cathode is a filament and cap setup. The heated tungsten or LaB6 emits electrons and the negative cap confines the electrons into a focused beam. The positive potential anode accelerates the electron beam then the electromagnetic lenses and apertures focuses it tightly. The focused electron beam with a very well-defined energy interacts with the atoms of the sample while transmitting it providing structural information. In TEM two modes are used; imaging mode and diffraction mode. The TEM provides high resolution images, information about the crystal structure, dislocations, grain boundaries and chemical analysis.

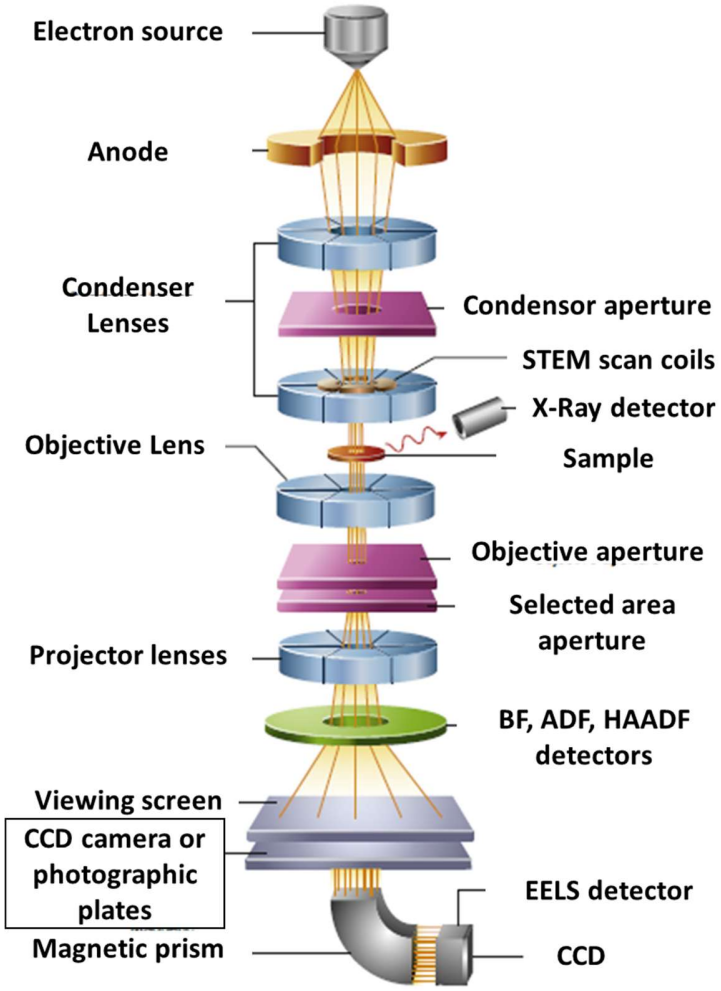

***Fig. 3.10**. Schematic view of a TEM [97].*

The Philips CM20 Transmission Electron Microscope (TEM) operated at 200 kV acceleration voltage has been used to investigate the composites microstructures. The discs with 3 mm diameter and 50 μm thickness in the centre have been prepared by mechanical thinning, polishing, and dimpling. Technoorg Linda ion mill has been used to reach electron transparency thickness (~ 10 – 100 nm), 10 keV Ar^+ ions at an incidence angle of 5° with respect to the surface. In the final period of the milling process, the ion energy was decreased gradually to 3 keV to minimize ion-induced structural changes in the surface layers. The TEM images were taken in plan view.

4. Preparation of samples and parameters

4.1. Milling and sintering of 316L reference and composites

I used the commercial 316L stainless steel powder (Höganäs company) and various ceramic additions for novel CDS composite development. The submicron sized α- Si_3N_4 (UBE), the grade "C" Y_2O_3 and the SiC (H.C. Starck) were used for the powder mixtures (Fig. 4.1).

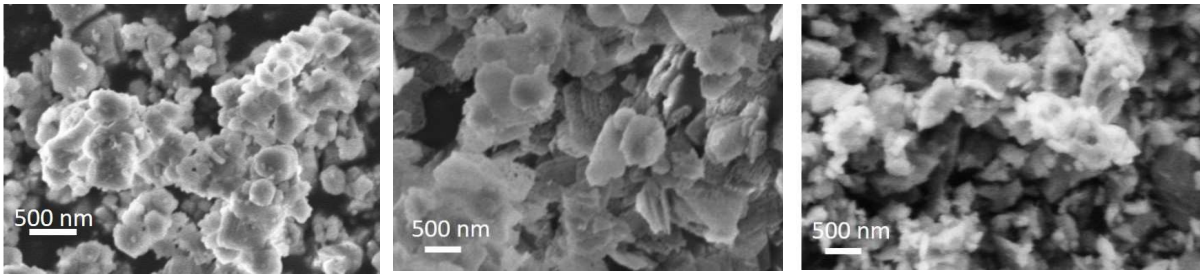

a) b) c)

Fig. 4.1. *Structure of starting ceramic additions. a) α- Si_3N_4 (UBE), b) the grade "C" Y_2O_3, c) SiC (H.C. Starck).*

The 316L powder has an apparent density (Hall) of 4.5 g/cm^3 and a flow rate of 18.2 sec/ 50 g. The elemental composition of starting powder is shown in Tab. 4.1.

Table 4.1. *Elemental composition of the 316L stainless steel starting powder.*

Element	Fe	Cr	Ni	Mo	Mn	Si	C
wt %	balance	17	12	2.3	0.1	0.9	0.015

The Tab. 4.2. shows the composition of the composites. In order to have a clear and reliable results of research work the composites were investigated before and after every step of the experimental work, from the starting powders (SEM, EDS, XRD) to the tested sintered samples (SEM, EDS, XRD, TEM, density, hardness, 3-point bending strength and friction coefficient) as it is represented in the experimental work diagram (Fig 4.2) .

The high efficient attritor mill (01-HD/HDDM, Union Process) has been used for efficient dispersion of submicron sized ceramic powders (SiC, Si_3N_4, Y_2O_3) in 316L steel matrix. A stainless steel setup (jar, crossbar agitator, 3 mm diameter milling balls) has been used in order to minimize the powder contamination.

Table 4.2. *Summarized data of composition of the developed composites.*

Nr.	milled 316L (wt%)	SiC (wt%)	Si_3N_4 (wt%)	Y_2O_3 (wt%)	milled powder (kg)	diameter of sintered sample (cm)
1	100	0	0	0	1.2	10
2	99.67	0.33	0	0	1.2	10
3	99	1	0	0	1.2	10
4	99.67	0	0.33	0	1.2	10
5	99	0	1	0	1.2	10
6	99.67	0	0	0.33	1.2	10
7	99	0	0	1	1.2	10

The milling was performed at 600 rpm in ethanol for 5 h for grain size reduction and homogenization of powder mixtures (316L and addition). Based on our previous experimental works, these parameters are suitable for efficiently assure both good distribution of the additives and reducing the size of the steel grains [28].

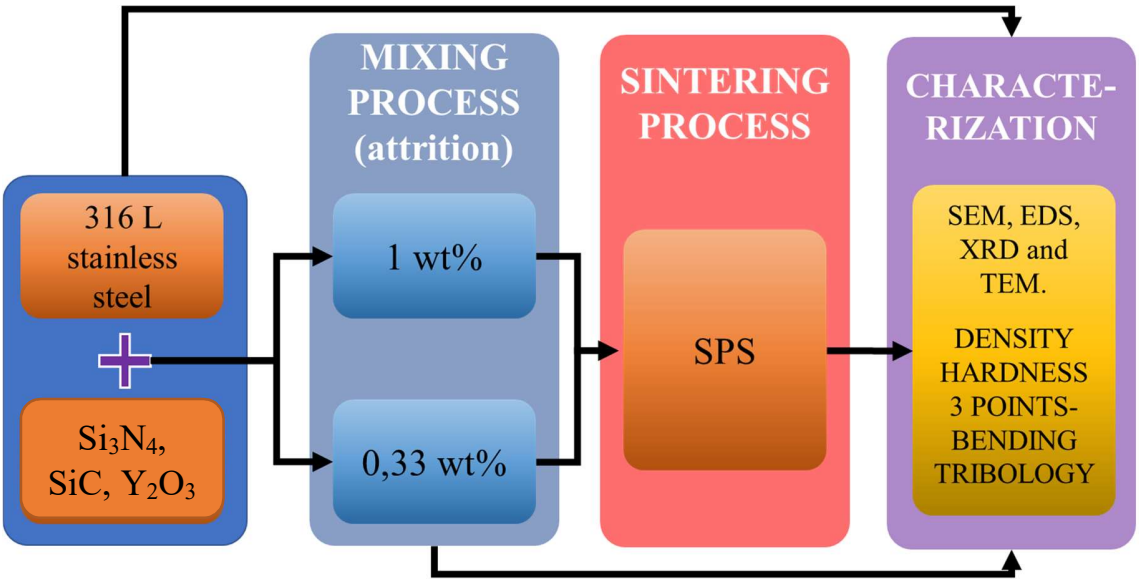

Fig. 4.2. *The schematic view of the experimental work diagram.*

The powders have been dried at 70°C, sieved for particles separation and stored well sealed boxes in order to avoid oxidation. The necessary powder amount for making two large sintered discs is 1200 g. The milling jar was relatively small, I could only mill 300 g at a time, as a result 4 batches were prepared from each composite. Samples from every batch were taken for studying the structural and morphological changes after the attrition milling.

The spark plasma sintering process was performed in collaboration with Prof. Dr. Filiz Cinar Sahin from the Department of Metallurgical and Materials Engineering, Istanbul Technical University in Turkey. SPS (Sinter-SPS-7.40MK-VII) was used for sintering of the milled powders at 900°C under 50 MPa mechanical pressure for 5 minutes dwelling time in vacuum. Sintered solid disks with ~ 100 mm diameter and ~ 9 mm thickness have been obtained.

4.2. Cutting of the sintered discs

Seven different large solid discs have been obtained after the spark plasma sintering. The discs surfaces were rough and hard due to the enrichment with carbon from the graphite mold during the SPS process, therefore, the removal of the discs outer layer was necessary in order to obtain a clean and smooth surface for precise cutting and easier samples preparation. For the removal of the outer layer I used a mechanical lathe machine (Fig. 4.3). During the removal of the disc surface, water has been used as a cooler to avoid over heating the composite. After the removal of the exterior layer the large discs needed to be cut into rectangular bars for density and mechanical properties testing, waterjet cutting machine has been used in order to assure precise cutting of the samples. The rectangular bars (Fig. 4.4) have dimensions of 4 mm x 50 mm x 9 mm, some of the bars have been cut into smaller bars of 4 mm x 25 mm x 4 mm for the 3-points bending test.

In the case of the large samples, the possibility of having anisotropic properties is high due to the possible nonhomogeneous heat during the sintering process or the cooling time, therefor, the samples number: 1-4, 10-12 (Fig. 4.4) have been selected in order to cover most the disc area and to assure reliable structural and mechanical properties results.

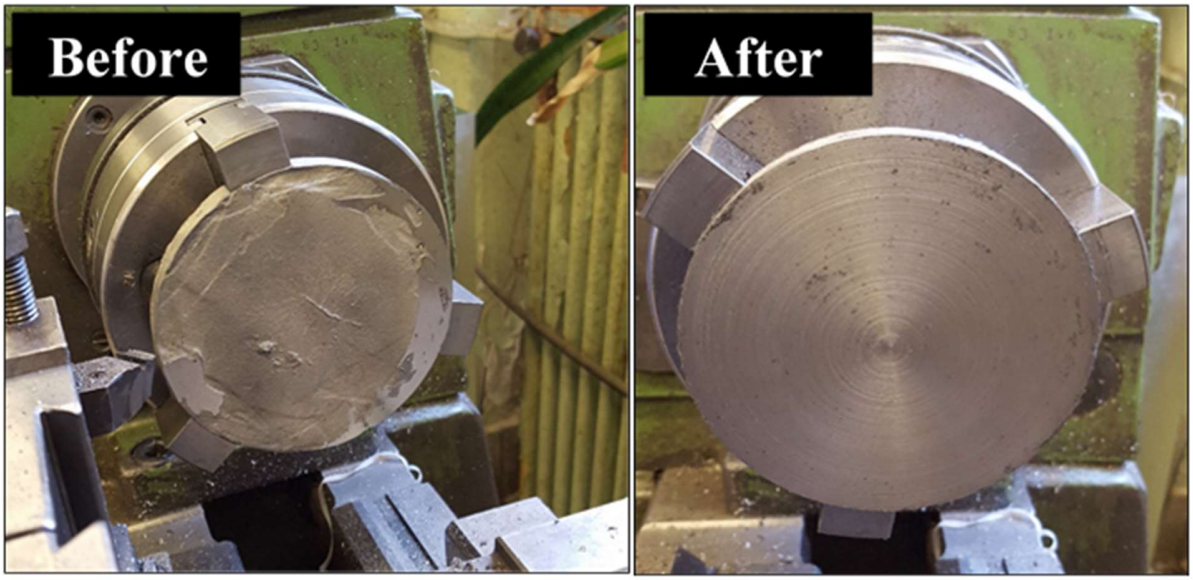

Fig. 4.3. *Photo of the sintered 316L composite disc. a) before and b) after the removal of the exterior surface.*

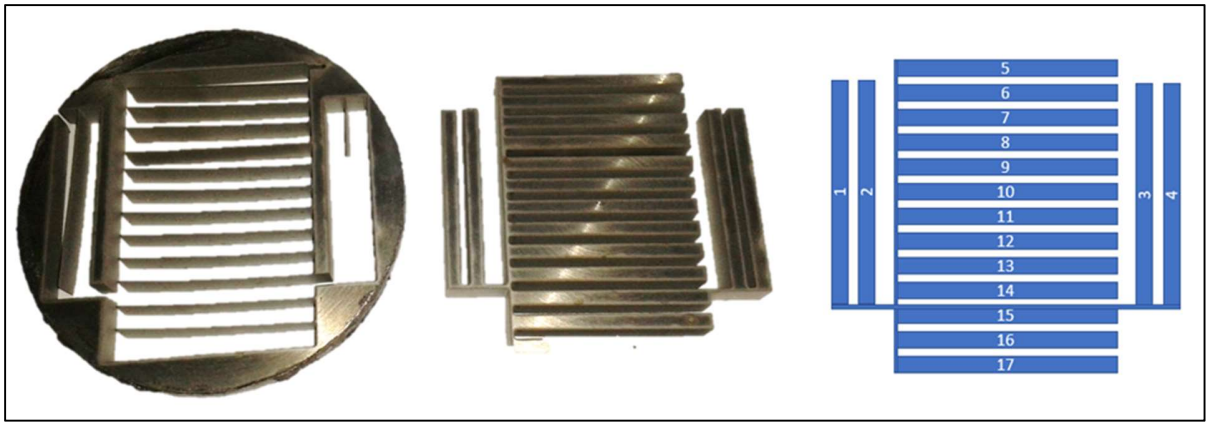

***Fig. 4.4**. Photo and schematic view of the sintered composite after waterjet cutting.*

4.3. Density Measurement

The samples were not polished before density measurements to sustain the surface state and abolishing any possibility of closing open porosities. In the cases where contamination (with organic fluids) was suspected, I cleaned these samples by ethanol using ultrasonic cleaning device for approximately 2 minutes then dried immediately.

The dimensions, the weight of dry samples, weight in water, water temperature and the weight after immersion in water for 72 hours were measured in order to calculate the density using the Archimedes equation

$$D_s = \frac{m_0}{\mathrm{m_1 - m_2}} * \rho_{water} \qquad (4.1)$$

Where

D_s: density of the sample
m_0: mass of the sample in air before immersion in water
m_1: mass of the sample in air after immersion in water
m_2: mass of the sample in water.

4.4. Vickers Microhardness

I polished all samples using abrasive SiC paper-starting with P120 and finishing with P1000- in order to have a clear surface for precise measurements and better observation of cracks in case they exist. The hardness equipment (LEITZ WETZLAR GERMANY model 721 464) by Vickers diamond pyramid tip was used for determination of microhardness of reference and composites according to international standarts. I measured every sample 10-15 times taking in considerations

keeping 5 times the diagonal width of the microhardness print as indentations mark spacing as shown in Fig. 4.5**.** 5N load applied for 30 seconds was sufficient to make a clear and measurable indentation on all composites.

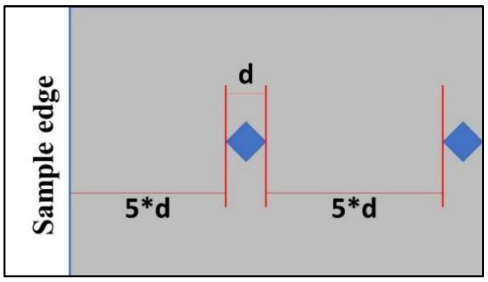

Fig. 4.5. *The principle of the microhardness indentations mark spacing, d: diagonal width of the microhardness print.*

4.5. 3-point bending test

8 small bars with the dimensions of 4 mm x 25 mm x 4 mm from each composite were polished with sanding papers (P120-P1000) and their edges were rounded (Fig. 4.6) in order to minimize the possibility of crack initiating from a superficial crack. All the spots on the samples surfaces where a crack may start have been marked before testing in order to follow the crack propagation. The 3-point bending test has been performed using the INSTRON 2500 equipped with a special 3-point bending test setup, according to international standards.

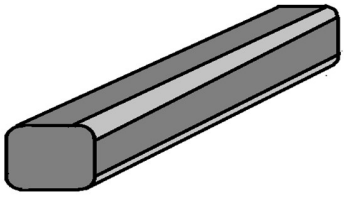

Fig. 4.6. *The schematic representation of a rounded edges and polished sample.*

4.6. Tribological measurements

The samples have been polished by sanding papers (P120- P1000) in order to have similar surface roughness before testing the tribological properties. The tribology test has been performed at room temperature using a CSM+ HT Tribometer in dry conditions (no lubricant). A 5 mm Si_3N_4 balls have been used as counterpart during the test. 5 N normal load was applied on the Si_3N_4 ball against the sample surface with 1mm shift from the rotation axis. The samples were tested at linear speed of 0.07 m/s where the humidity ranges from 55% to 63%.

5. Results and Discussion

In this chapter, the preparation and various properties of 316L reference and novel composites with SiC, Si_3N_4 and Y_2O_3 addition are discussed. The microstructure evaluation was studied by scaning electron microscopy (SEM) and transmission electron microscopy (TEM). The roughness and surface changes after tribological and mechanical measurements were investigated by digital microscope (DM). The mechanical properties (hardness and bending strenght) were determined by Vicker hardness measurements and Instron mechanical testing machine.

5.1. Investigation of 316L reference material

Commercial 316L stainless steel (Höganas) with composition of 17Cr12Ni2.3Mo0.1Mn0.9Si and average size ~ 70 μm was used as reference material (Fig. 5.1a).

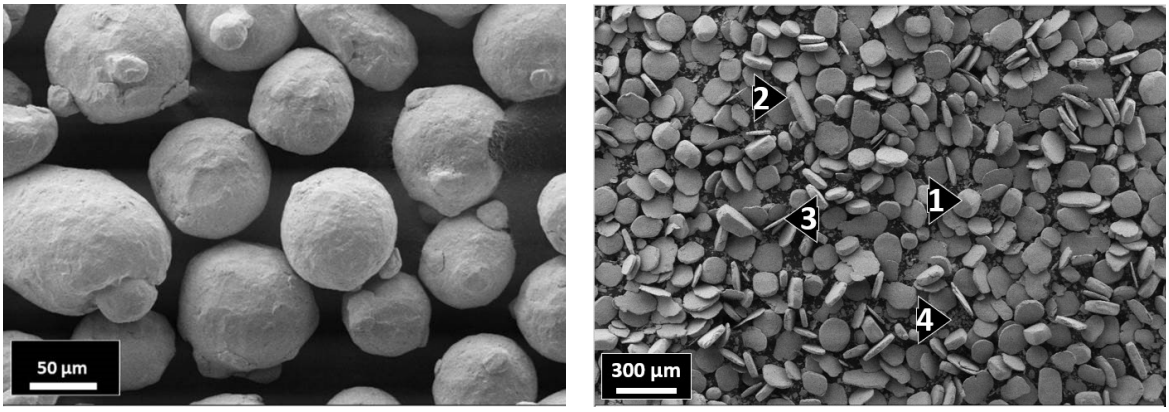

a) b)

Fig. 5.1. *SEM images of 316L. a) starting powder, b) after high attrition milling.*

The starting powders transformed mainly from globular to flattened (2) and flakelike shape (3) with the presence of few slightly damaged grains (1) after 5 hours wet milling in ethanol (Fig. 5.1b). Some of the thin flake-like grains broke down into the very small particles (4) shown in Fig. 5.1b). The average grain size increased due to the grains flattening. The milling was not as efficient as we expected most probably due to the simultaneous increase in the grain's hardness and plasticity. Therefore, the morphology of resulting powder is characterized by both flattened or partially transformed globular shape. However, the induced shape transformation by the attrition milling in 5 hours is much efficient comparing the induced transformation by planetary mill in 8 hours [101,102].

The investigation of the chemical composition by EDS confirmed the detailed 316L composition provided by Höganäs company (Fig. 5.2a). The milling process changed the morphology and grain size of powder, not the phase composition as it is shown on Fig. 5.2b.

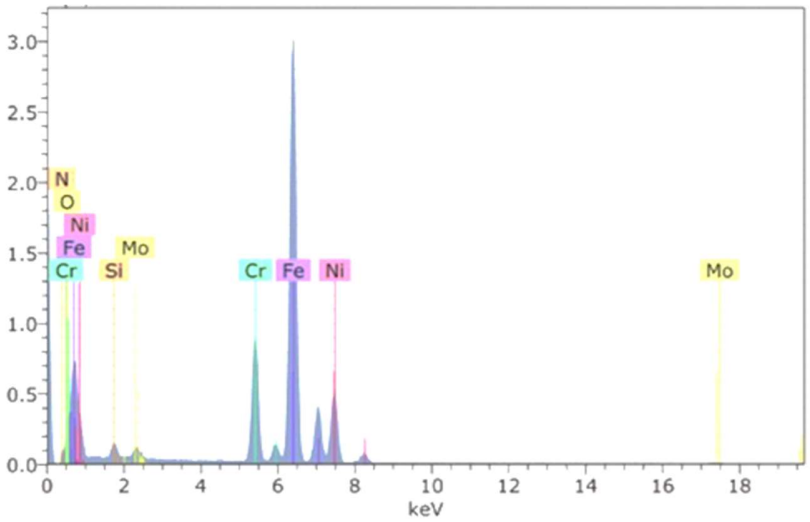

a)

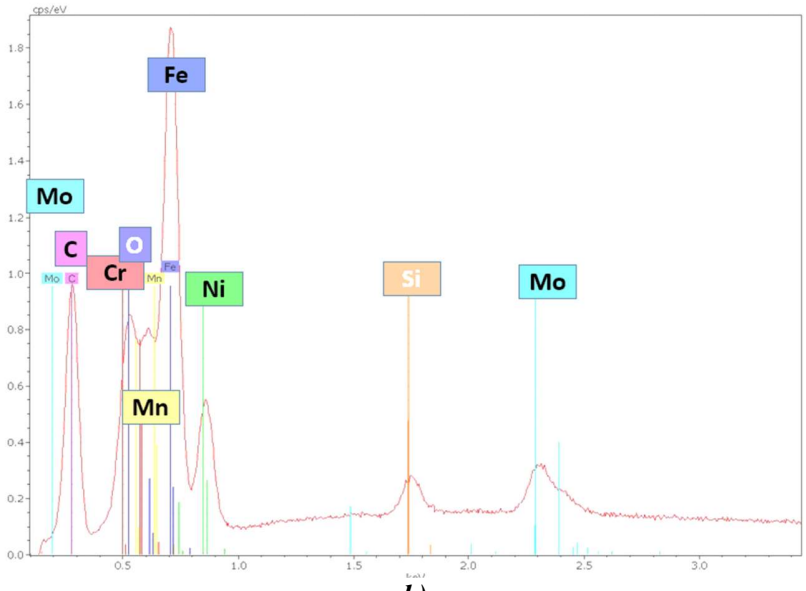

b)

Fig. 5.2. *EDS analysis of a)316L powder of the starting powder, b) 316L powder after Attrition milling.*

Spark plasma sintering (SPS) was used for compactation of milled powders. The detailed sintering process with parameters was described in Chapter 4. The structural investigations of the sintered samples revealed the presence of randomly dispersed grains (dark spots) in the steel matrix (Fig. 5.3a). The elemental analysis of the selected spots showed that the selected spots are zones with high content of the manganese (Mn), silicon (Si) and chromium (Cr) oxide phases (Fig. 5.3b). The formation of these oxides occurred during the SPS process.

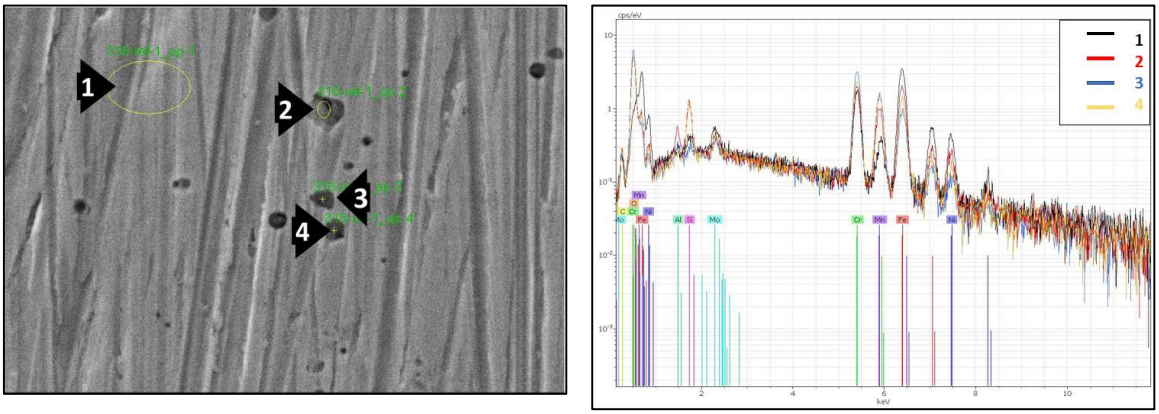

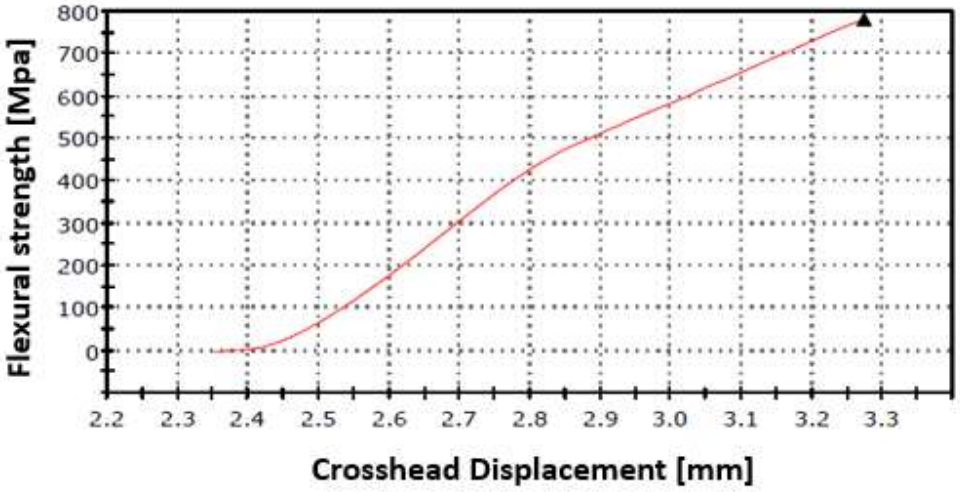

c)

Fig. 5.3. *Investigation of sintered 316L. a) SEM images of milled and sintered 316L reference, b) EDS measurement of 316L reference sample, c) 3-point bending test results.*

The Fig. 5.3c shows a 3-point bending test result of a sintered 316L sample, the samples were bent and didn't show any tendency to break, the testing had to be stopped when the setup limits have been reached.

The structural investigation of the sintered 316L by TEM revealed the presence of dislocations and twins patterns in the steel matrix (Fig. 5.4).

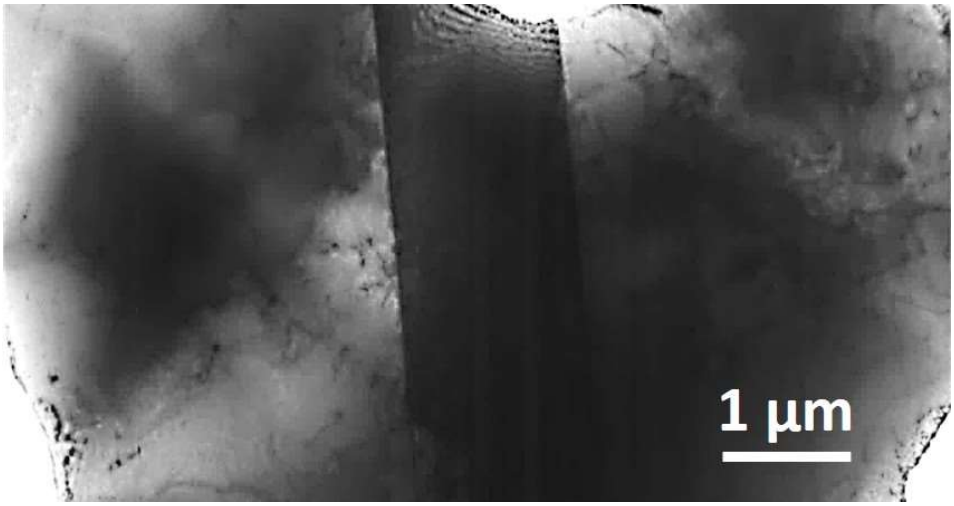

Fig. 5.4. *TEM image of sintered 316L reference.*

The XRD measurements confirmed the main lines of 2θ°= 43.532°, 50.705°, 74.535° in the case of milled and sintered sample as well (Fig. 5.5). There was no phase transformation detected after the SPS process. No open porosities have been clearly observed during the SEM investigation of the sintered 316L samples.

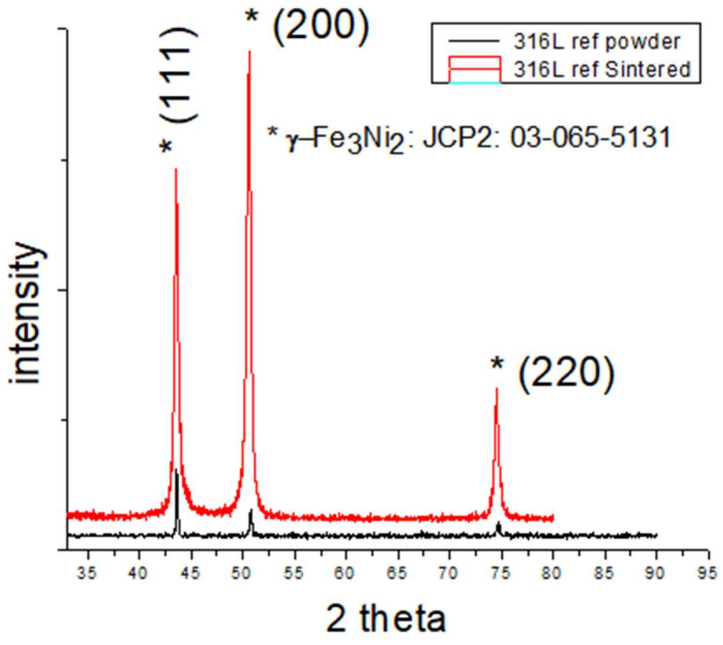

Fig. 5.5. *XRD measurements of 316L after milling and sintering process.*

The sintered sample showed an average density of 7.93 g/cm^3 which is 99.17% densification comparing to the 8 g/cm^3 theoretical density. The density of the 316L reference sample is in agreement with literature [35]. The samples sintered by SPS process are showing higher density values compared to the sintered 316L sintered in special furnace [17, 21, 63, 100,

101, 102] or selective laser melting (SLM) [98,99,102,104]. The mechanical properties of 316L were studied. The hardness (HV) was 1.75GPa.

The tribological properties of sintered 316L confirmed the friction coefficient (μ) ~ 0.962 ± 0.108 in dry conditions. 316L sample and the counterpart (Si_3N_4 ball) have been also damaged. The damaged surfaces study confirmed the formation of tribofilm (Fig. 5.6a). The wear track is uniform and takes a curved shape relatively matching the curvature of the counterpart (Fig. 5.6b). The elaborated 316L stainless steel showed a wear rate of ~1.36E^{-4} m^2/N.

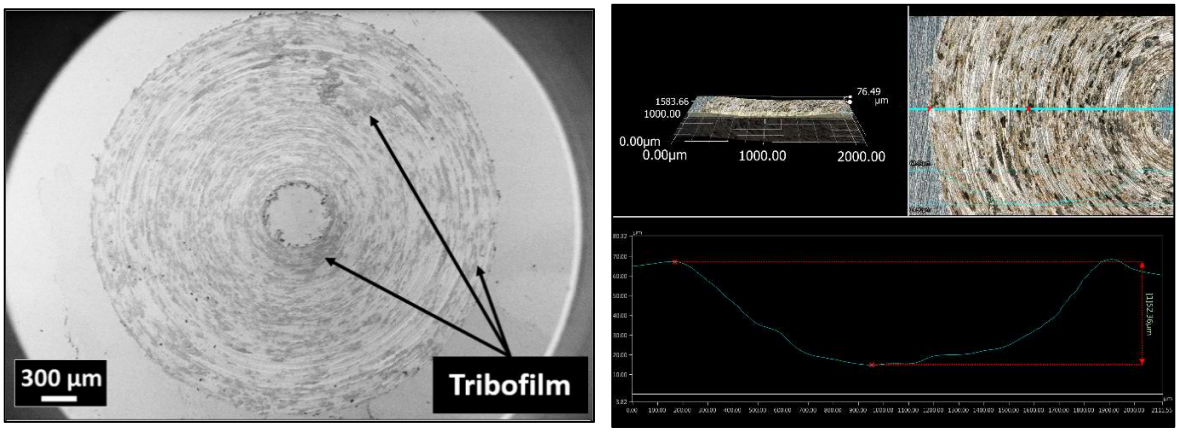

a) b)

Fig. 5.6*. Tribological measurements of 316L reference. a) digital image of surface after tribology maesurement, b) morphology of wear track.*

.

5.2. Investigation of 316L/SiC composites

In this work, the 316L austenitic steel (Fig. 5.1a) based milled and sintered composites with 0.33 wt% and 1 wt% SiC nanoparticle (Fig. 4.1c) addition were prepared. The investigation of the milled powders revealed a total morphological transformation.

The 316L steel grains in the case of the milled 316L/0.33 wt% SiC powder mixtures have been transformed from globular shape with satellites to considerably larger steel grains with 100 - 200 µm in diameter and ~ 1 µm in thickness (Fig. 5.7a). The presence and the good distribution of the SiC particles on the 316L grains surface and a difference in the size of the SiC particles have been confirmed by SEM (Fig. 5.7b). A homogeneous coverage of flat steel grains by ceramic particles can be noticed. In the case of the 316L/1 wt% SiC, a similar morphological transformation has been observed (Fig. 5.8a). The Fig. 3b shows the presence and the uniform distribution of the SiC particles on the surface of the flat steel grains.

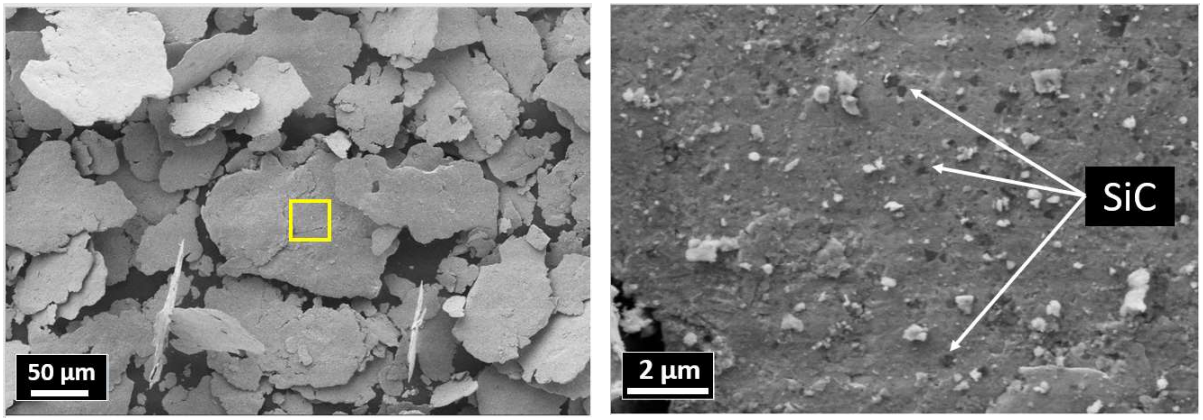

a) b)

Fig. 5.7. *SEM images of the milled 316L/0.33 wt% SiC. a) milled powders, b) higher magnification of the selected area in Fig. 5.7a.*

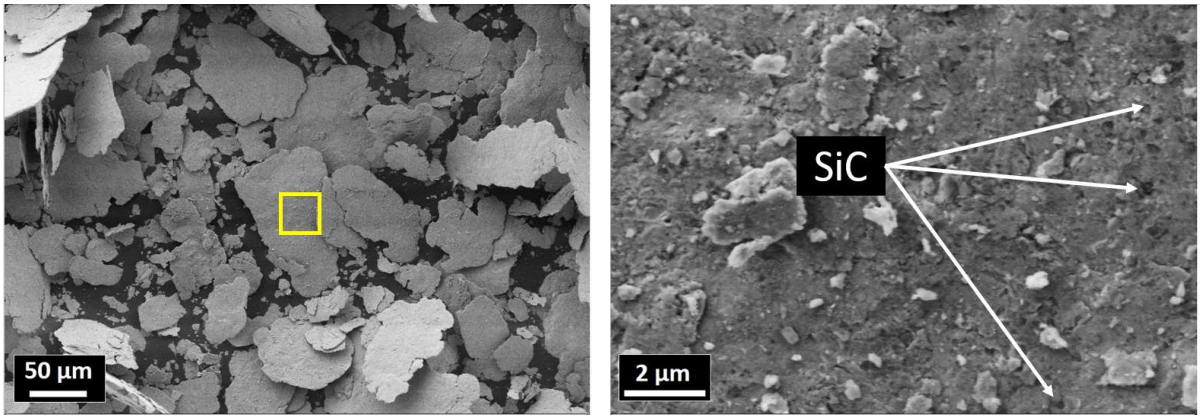

a) b)

Fig. 5.8. *SEM images of the 316L/1 wt% SiC. a) milled powders, b) higher magnification of the selected zone in Fig. 5.8a.*

SiC particles are covering the steel grains and in the same time show a tendency to agglomerate. This feature can be observed both on the surface of the 316L/1 wt% SiC grains (Fig. 5.8b) and on the 316L/0.33 wt% SiC grains (Fig. 5.7b). The structural investigations of the milled powders with composition of 316L/0.33 wt% SiC and 316L/1 wt% SiC by SEM and EDS confirmed the presence of the SiC particles on the surface of the metallic grains (Fig. 5.9 and Fig. 5.10). The relatively lower intensity of peaks related to presence of Fe, Cr and Ni in the selected dark spots shows the good and efficient coverage of the steel grains by the SiC particles.

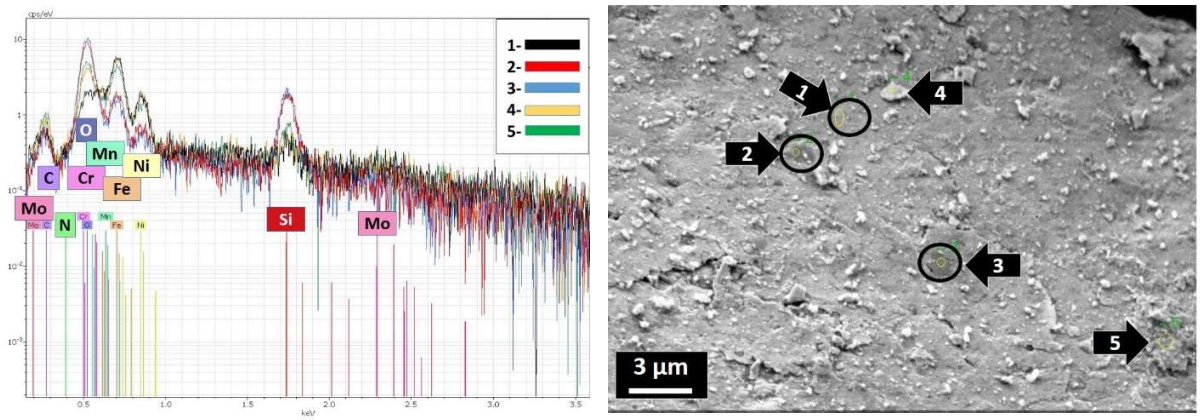

a) b)

***Fig. 5.9**. Investigation of the 316L/0.33 wt% SiC composite, a) EDS spectra b) SEM image showing the EDS spots.*

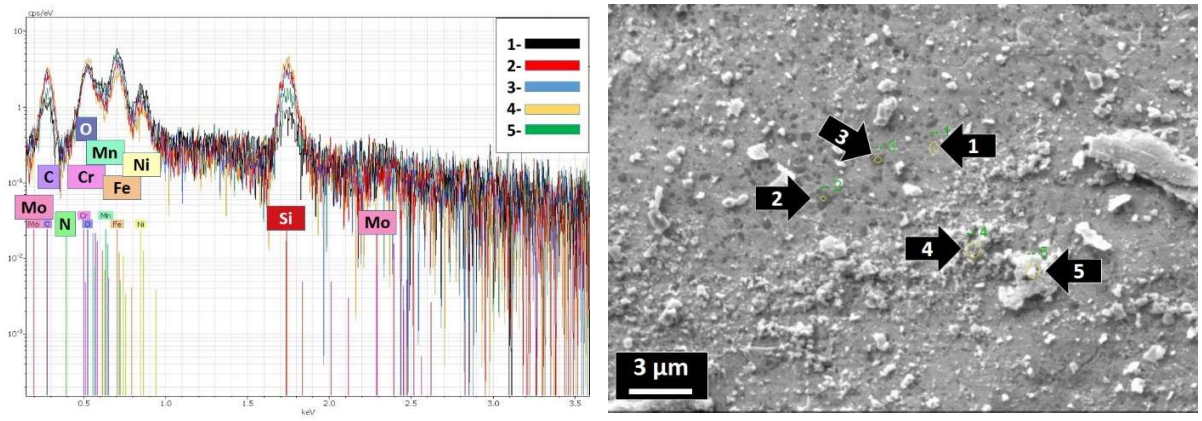

a) b)

***Fig. 5.10**. Investigation of the 316L/1 wt% SiC composite, a) EDS spectra b) SEM image showing the EDS spots.*

The phase composition of the milled 316L and 316L/SiC composites have been investigated by XRD. In the case of the milled 316L (reference) the analysis confirmed the austenitic stainless steel γ-Fe_3Ni_2 phase (JPC2:03-065-5131) with main lines 2θ = 43.532°, 50.705°, 74.535° (Fig. 5.11a). In both cases, 316L/0.33 wt% SiC and 316L/1 wt% SiC composites,

two phases have been observed. The dominant phase is the same γ -Fe_3Ni_2 austenitic phase in addition to the ferrite α-Fe phase (JCP2: 03-065-4899) with main lines of 2θ = 44.663°, 65.008°, 82.314° (Fig. 5.11a). The XRD diffractogram of the sintered composites (Fig. 5.11b) shows that the ferrite α -Fe phase has been transformed to the austenitic γ-Fe_3Ni_2 phase during the sintering process.

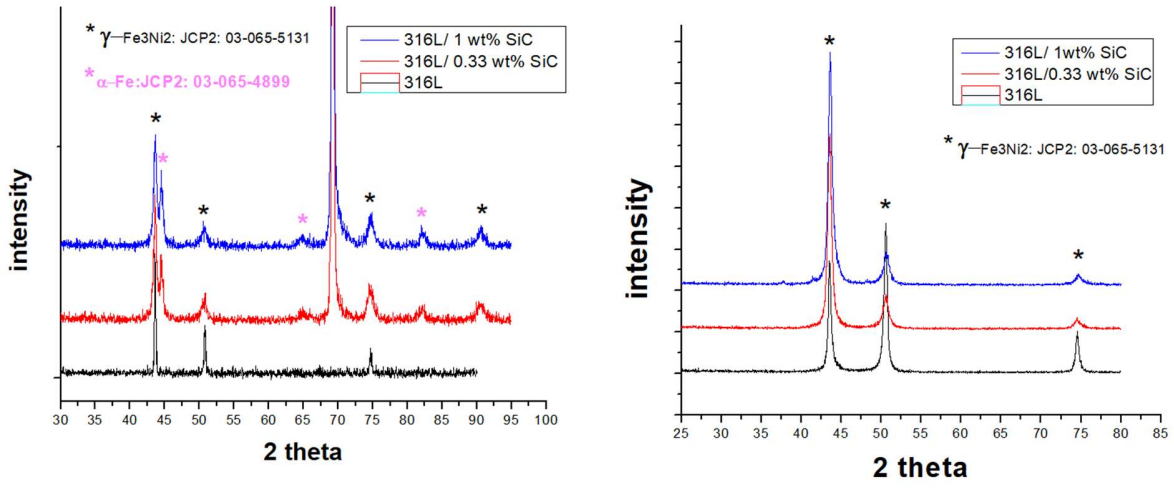

a) b)

Fig. 5.11*. XRD diffractograms of 316L /SiC. a) the milled powder mixtures in comparison with the 316L powder, b) the sintered composites in comparison with the sintered 316L sample.*

The investigations of the sintered steel composites surfaces by SEM (Fig. 5.12) and EDS (Fig. 5.13 and Fig. 5.14) showed most probable of SiC particles with oxygen contribution (the dark spots distributed in linear form, white and black parallel lines). The high level of oxygen content in the areas where the SiC particles are distributed indicates the possible oxidation of added SiC particles. Larger silicon oxide particles have been observed in the case of 316L/0.33wt% SiC composite as it shown in Fig. 5.12a and Fig. 5.13a.

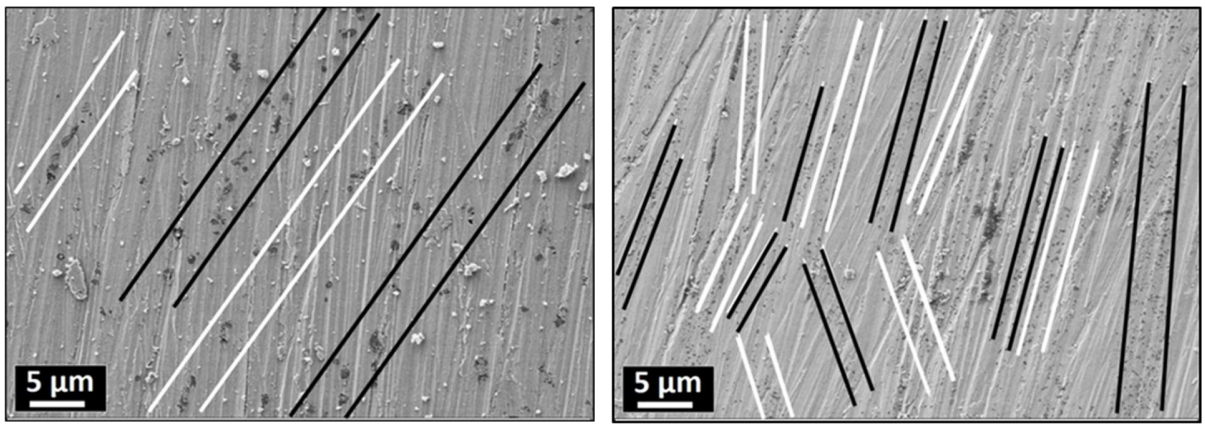

a) b)

Fig. 5.12. *SEM images of the sintered composites. a) 316L/0.33wt% SiC, b) 316L/ 1wt% SiC.*

An indication for this is the higher peak intensity of the silicon and oxygen in the EDS spectra (Fig. 5.13b) comparing to the peaks in case of the 316L/1wt% SiC (Fig. 5.14b).

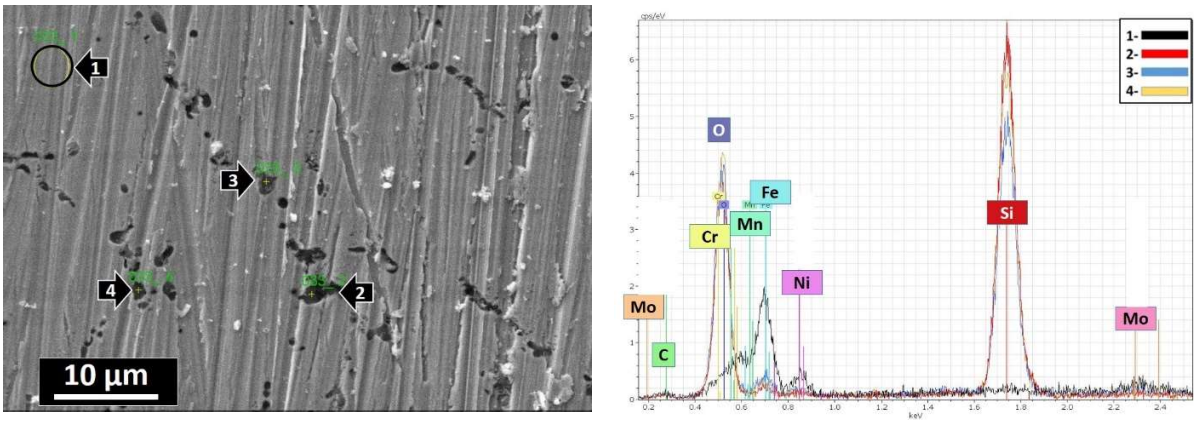

a) b)

***Fig. 5.13**. Structure of the 316L/0.33wt% SiC. a) SEM and b) EDS.*

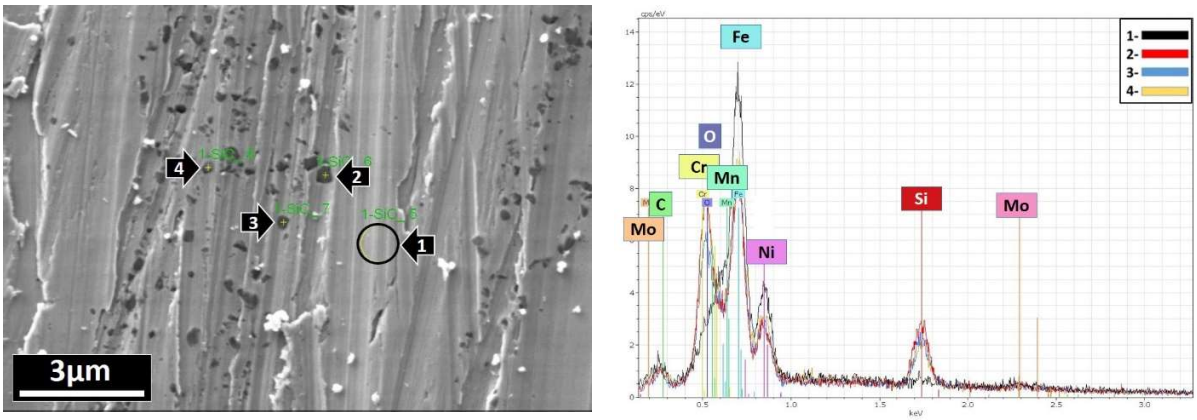

a) b)

***Fig. 5.14**. Structure of 316L/1wt% SiC. a) SEM and b) EDS.*

The density and microhardness of the sintered reference sample 316L and composites are shown in Fig. 5.15. The relative density of 99.17%, 96.66% and 95.2% have been achieved respectively for the 316L reference samples, 316L/ 0.33 wt% SiC and the 316L/ 1 wt% SiC. The density decreased with the increasing of the SiC amount in the steel matrix. Both composites showed higher microhardness (2.98 GPa and 2.79 GPa for the 0.33 and 1 wt% SiC respectively) values compared to the reference sample (1.75 GPa) and even to those sintered in furnace [21, 61,102], SLM [98,103 and 105] and SPS [106, 117]. The lower microhardness value in the case

of the 316L/ 1 wt% SiC composite (2.78 GPa) compared to the 316L/ 0.33 wt% SiC (2.98 GPa) is due to its lower density.

The 3-point bending test results of the 316L/ 0.33 wt% SiC composite are shown in Fig.5.16a. The samples were just bended and didn't break, very small cracks occurred on the samples' corners during the test. As soon the applicable load limit has been achieved the measurement had to be stopped in order to prevent damaging the used equipment (similar as 316L reference sample).

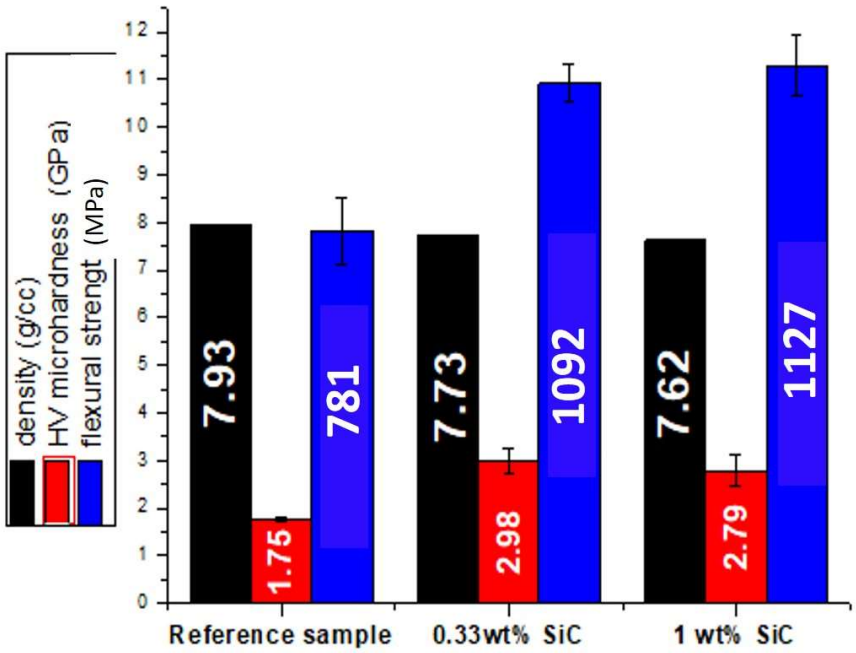

***Fig. 5.15**. Comparison of the microhardness (Hv, [GPa]), density [g/cc]and the flexural strength [MPa] of the sintered composites.*

In the case of the 316L/ 1 wt% SiC composite (Fig. 5.16b), the samples were broken and showed an average flexural strength of 1127 ± 10 MPa which was higher than for the 316L steel found in literature [21]. The investigation of the broken surface by SEM (Fig. 5.17) revealed cracking behaviour/mechanism of the composite, which is a mixture of transgranular and intergranular, as it is illustrated in the Fig. 5.18. The metallic bridges have been formed between the lamellar steel grains during the sintering process and it is clearly shown in Fig. 5.17 (insert). Complex grains boundaries have been observed.

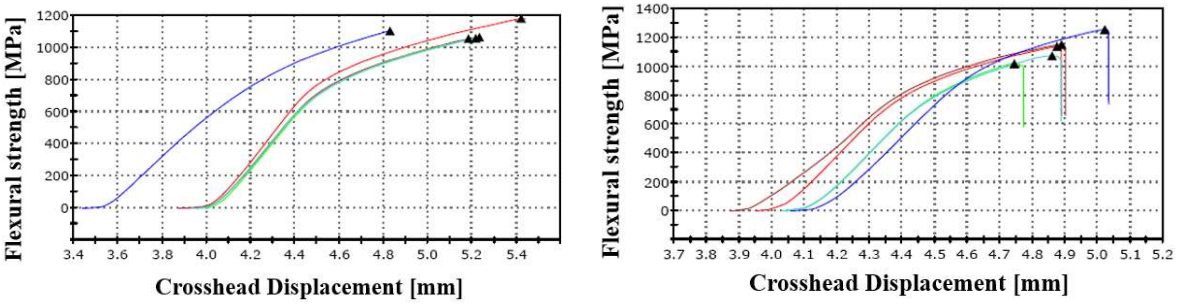

a) b)

Fig. 5.16. *3-point bending test results. a) 316L/ 0.33wt% SiC, b) 316L/1wt% SiC.*

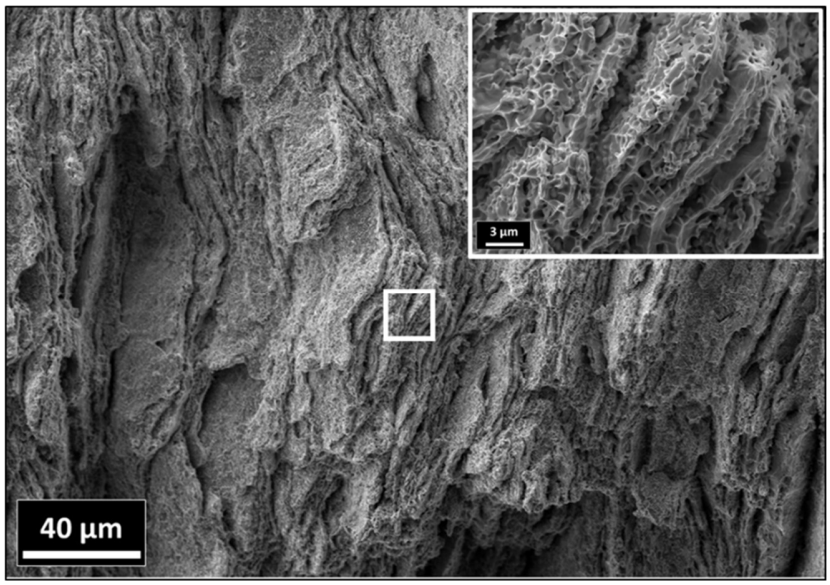

Fig. 5.17. *SEM image of the 316L/1wt% SiC fractured surface.*

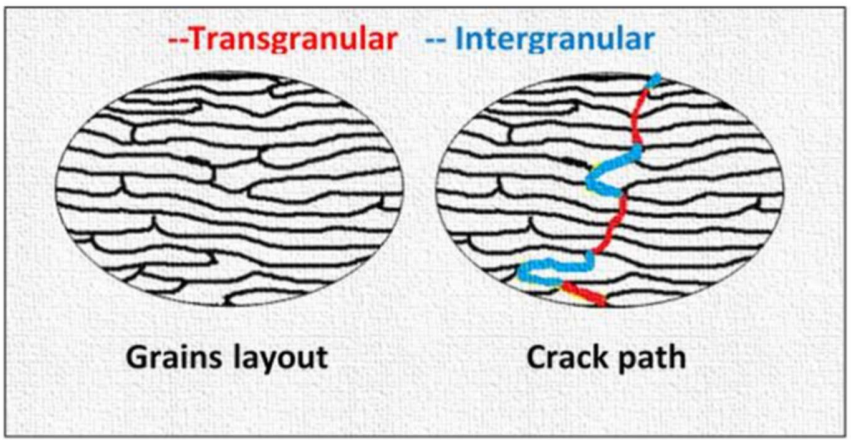

Fig. 5.18*. Schematic representation of the cracking behaviour of the 316L/1wt% SiC.*

Tribological properties of the sintered composites have been studied as well. The friction coefficients of 0.962, 0.879 and 0.930 have been determined respectively for all composites (sintered reference sample 316L, 316L/ 0.33wt% SiC and the 316L/ 1wt% SiC). In all cases, the erosion has been noticed on the tested surface and the Si_3N_4 ball counterpart, as well. The investigation of the damaged and eroded surface showed the formation of tribo-layer on the steel's surface (Fig. 5.19). The tribo-layers most probably consist of the crystalline or amorphous mainly Si_3N_4 originating from the counterpart (ball). The higher friction coefficient ~ 0.930 in case of the 316L/ 1wt% SiC composite (Fig. 5.19a) compared to 0.879 of the 316L/ 0.33 wt% SiC (Fig.5.19b) was due to its lower density and lower hardness. The structural observations of the sintered 316L/0.33 wt% SiC and 316L/ 1wt% SiC composites are shown in Fig. 5.20.

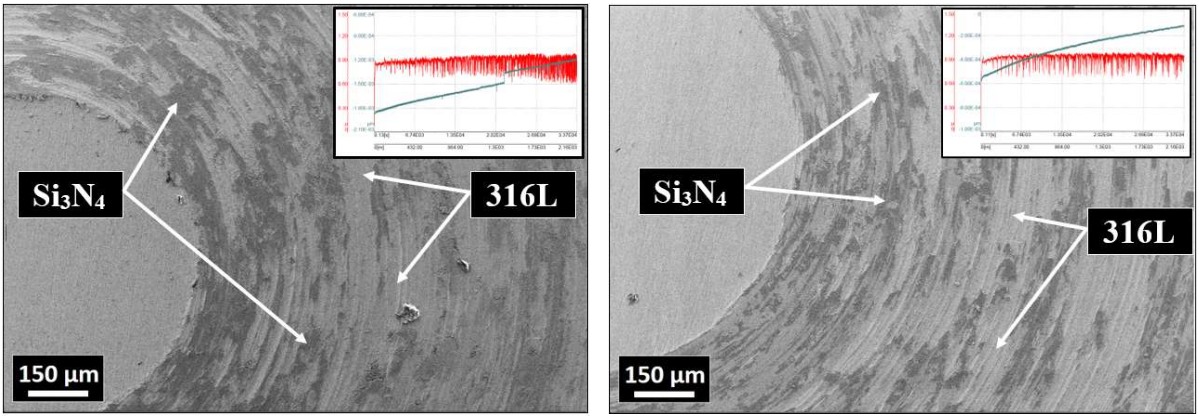

a) b)

Fig. 5.19. *SEM images of the damaged surface of the 316L/SiC after tribology test and friction coefficient curve (insert). a) 1wt% SiC, b) 0.33 wt% SiC.*

It was confirmed that the ceramic particles with average size ~ 50-100 nm particles (white rounded spots) were embedded into micrometer sized steel grains (Fig. 5.20). A better distribution of ceramic particles was observed for the 1 wt% SiC addition.

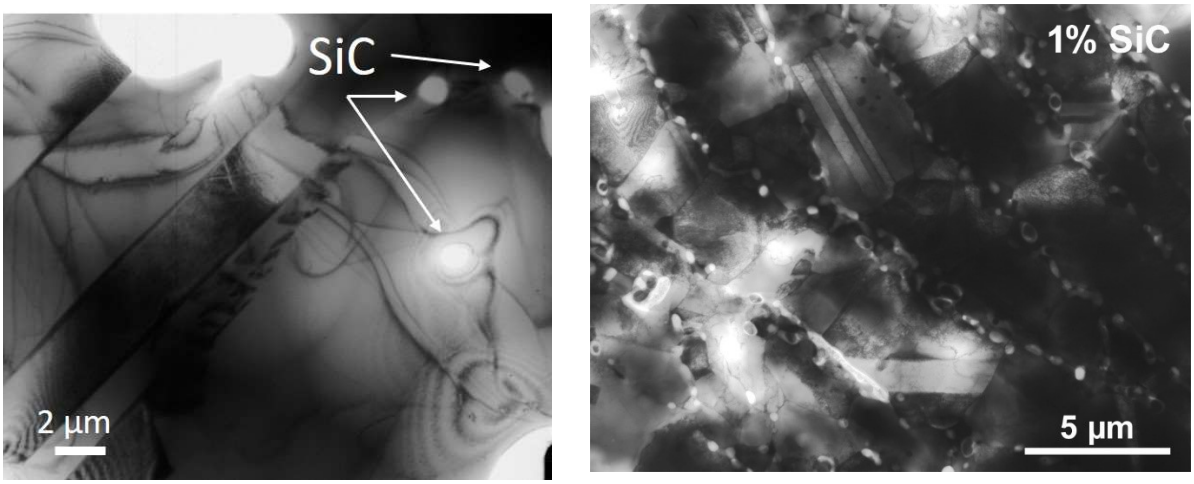

a) b)

Fig. 5.20. *Bright field TEM images of the sintered 316L/SiC composite. a) 0.33 wt% SiC, b) 1 wt% SiC.*

Conclusions

The preparation of ceramic dispersion strengthened steel (CDS) with different compositions of SiC powders was successful. The distribution of the SiC particles was homogenous in both composites. A ferrite phase have been detected in the milled powders due to austenite-martensite transformation or contamination from the milling setup. This ferrite phase has been transformed to the γ-Fe_3Ni_2 during the sintering process. Densification of 99.17%, 96.66% and 95.2 % have been achieved respectively for the reference, 316L/0.33wt% SiC and 316L/1wt% SiC samples. The density decreased with higher amount of SiC addition to steel matrix due to its lower density and the presence of more porosities. The SiC addition increased the hardness of the 316L matrix. A simultaneous transgranular and intergranular fracture behavior have been observed after the 3-point bending test of the 316L/1wt% SiC composite where an average bending strength of 1127.4MPa has been recorded. In the case of the 316L/0.33wt% SiC the samples didn't break due to their higher ductility. Tribological properties of the sintered composites have been studied. I observed that the addition of the SiC improves the tribological properties of the 316L stainless steel. The lowest friction coefficient 0.930 have been measured for the 316L/ 1wt% SiC composite. The structural investigation of the sintered composites by confirmed the distribution of the ceramic particles on the grain's boundaries.

5.3. Investigation of 316L/Si_3N_4 composites

In this work, the 316L austenitic steel based milled and sintered composites with 0.33 wt% and 1 wt% Si_3N_4 nanoparticle addition were prepared. The morphology investigation of the starting powder confirmed the steel grains with average size ~ 70 μm with globular form (Fig. 5.21a) and ~ 300 nm sized Si_3N_4 nanoparticles (Fig. 5.21b).

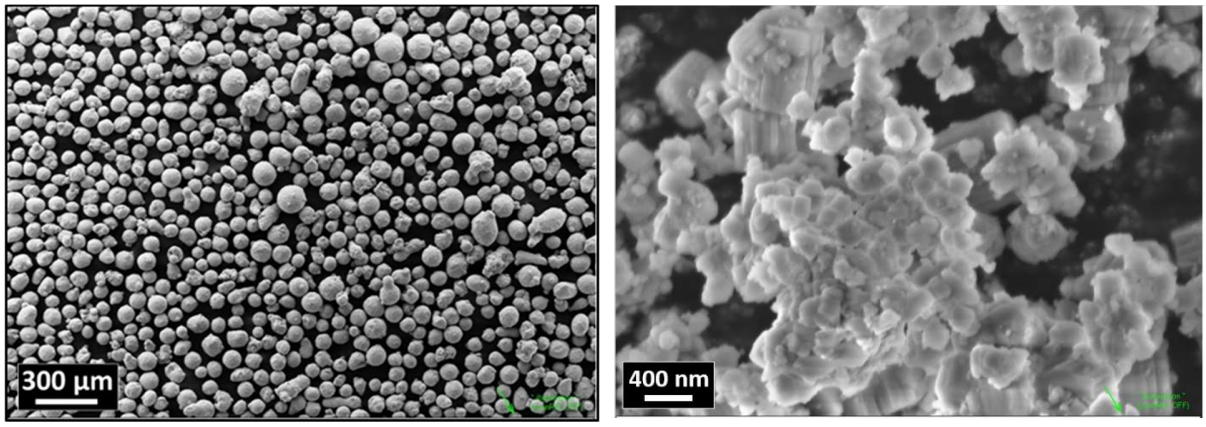

a) b)

Fig. 5.21. *SEM images of the starting powders. a) 316L b) Si_3N_4.*

The morphological investigations of milled powders and sintered composites are shown in Figs. 5.22 and 5.23, respectively. The 5 hours long wet milling induced striking morphological changes in the composite with 0.33 wt. % Si_3N_4 addition. The steel grains transformed from a globular (Fig 5.21a) to lamellar shape with two typical average sizes (Fig 5.22a); 100 μm and 40μm. The Si_3N_4 addition was distributed homogeneously and covered the surface of steel grains (Fig 5.22b). The morphology of ceramic addition before and after milling is similar (Fig. 5.21b and Fig. 5.22), only the average size is ~ 2 times smaller after milling. In the case of 1 wt% Si_3N_4, the milling was not so effective than in the case of lower ceramic addition (0.33 wt% Si_3N_4). The presence of three grain morphologies was demonstrated: lamellar (~1 μm thin and ~150 μm long), faceted (~25 μm thick and ~50 μm in length) and globular (~50 μm in diameter) (Fig. 5.22c). Due to the milling process, the submicrometer sized Si_3N_4 grains are fully distributed on the 316L grains surface (Fig. 5.22d). The higher amount of ceramic (1 wt% Si_3N_4) additive prevented the deformation and fracturing of the steel grains during the milling process. Two different effects were observed after milling process. First, the steel grain size reduction efficiency decreased and evolution of flat morphology or shaping of 316L grains is suppressed as the result of Si_3N_4 coverage that behaves like the shielding of each steel particle. The EDS measurement confirmed the presence of Si_3N_4 in the selected spots (marked by arrows in Fig. 5.22b and Ig.5.22d). The elemental composition measurements confirmed two almost similar high peaks of Si and N (due to the presence of Si_3N_4) in both mixtures. The decreases in the peak intensities of the 316L stainless steel elements (Fig 5.22e) is due to the good and homogenous coverage of the steel grains by Si_3N_4 particles. The better coverage in the case of 1 wt% Si_3N_4 resulted in enhanced decrease in the peaks intensities of the 316L grains.

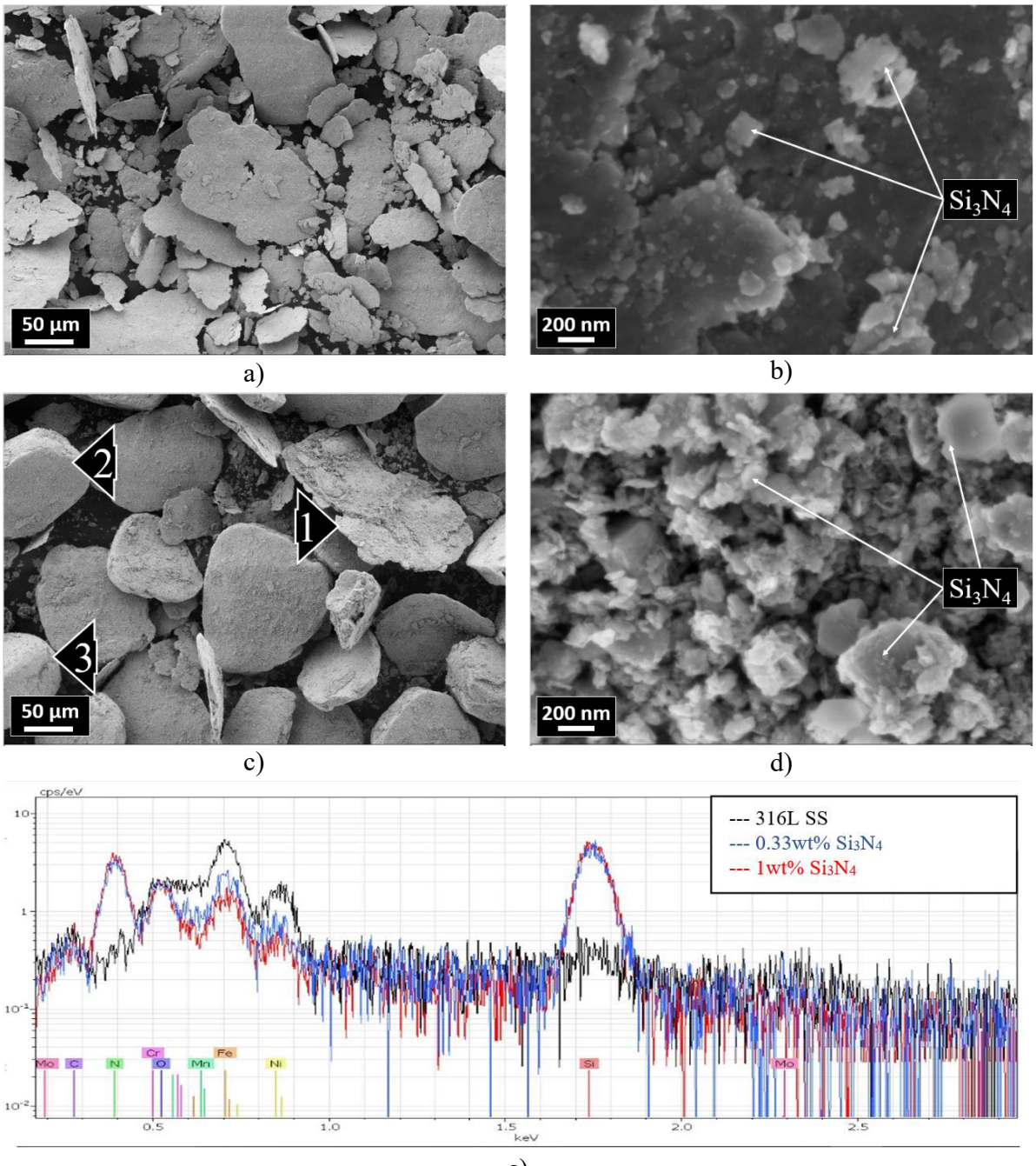

Fig. 5.22*. SEM images and EDS spectra of milled powders. a) 316L /0.33 wt% Si_3N_4, b) Si_3N_4 distribution on the surface of 316L/0.33 wt% Si_3N_4, c) 316L/1 wt% Si_3N_4 (1, lamellar grain; 2, facetted grain; 3, globular), d) Si_3N_4 distribution on the surface of 316L/1 wt% Si_3N_4, and e) comparison of EDS spectra (316L, 316L/0.33 wt% and 316L/1 wt% Si_3N_4 powders).*

Morphological investigations on fractured surfaces (at room temperature) of sintered 316L/0.33 wt% Si_3N_4 and 316L/1 wt% Si_3N_4 after sintering are shown in Fig. 5.23. In the case of 316L/0.33 wt% Si_3N_4 (Figs. 5.23a and 5.23b), the analysis of the resulting fractured surface after

3-point bending test by SEM revealed the dominance of the transgranular fracturing behavior with the presence of intergranular fracturing in some parts.

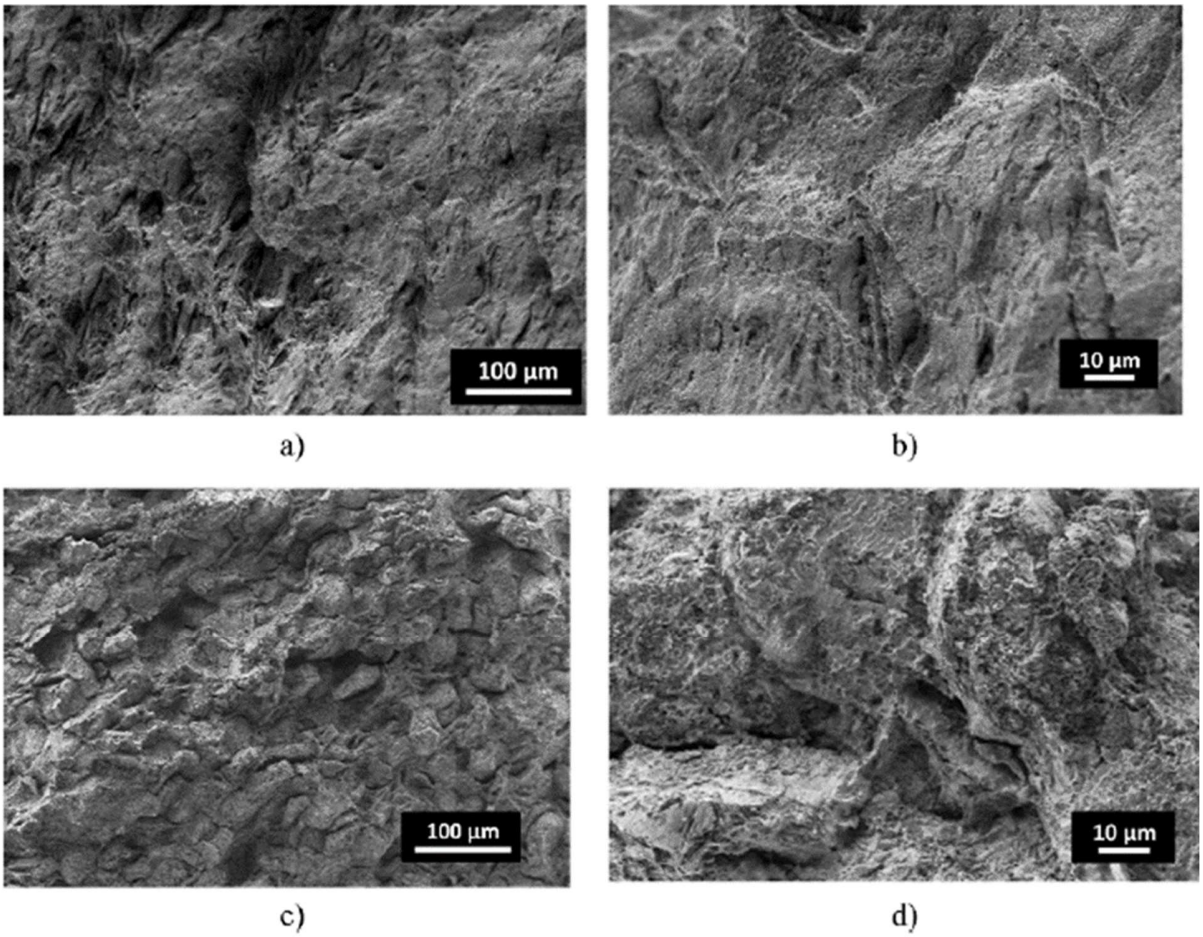

***Fig. 5.23**. SEM images of sintered composites fractured surfaces. a) and b) CDS with 0.33 wt. % Si_3N_4; c) and d) CDS with 1 wt. % Si_3N_4.*

This fracturing behavior is caused by the complex grain boundaries formed by large and thin lamellar grains (Fig. 5.24). In this case, the fracture is propagating both through intergranular or transgranular paths as shown in Fig. 5.24a. Unlike in the case of 1 wt% Si_3N_4, the slightly damaged globular grains covered with Si_3N_4 particles clearly affected the fracturing behavior as the SEM images show a dominance of the intergranular fracturing with the presence of very few transgranular fracturing (Fig. 5.23c and Fig. 5.23d). The required energy for transgranular fracture is greater than the intergranular fracture in the case of the 1 wt% Si_3N_4 due to the presence of thicker grains, therefore, the dominant fracturing behavior was intergranular as it is represented on Fig 5.24b.The average loads measured by 3-point bending test were 2627 N for 0.33 wt% Si_3N_4 whereas 2582 N resulted for 1 wt% Si_3N_4 addition. The first mixture (316L/0.33 wt% Si_3N_4) has been investigated by EDS in order to check presence and the dispersion of the ceramic particles on the surface of the steel grains.

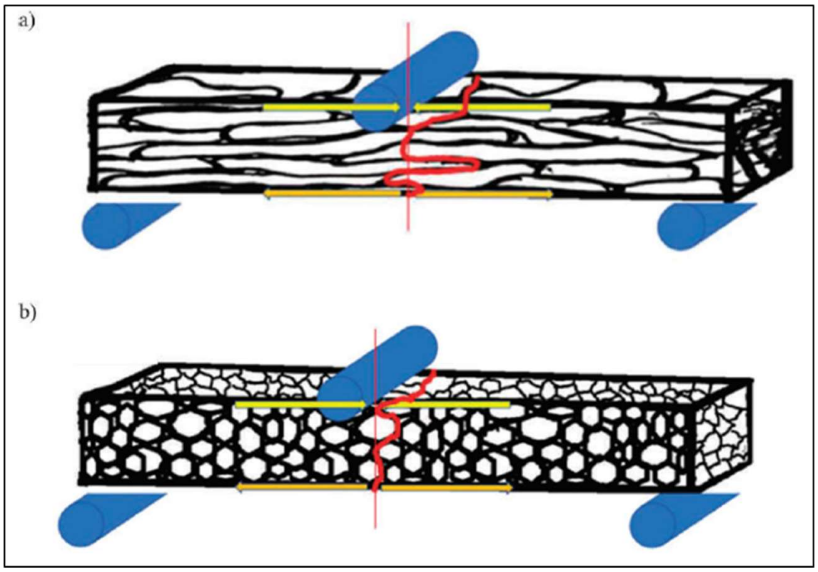

***Fig. 5.24**. Schematic representation of the dominant fracturing behavior. a) 316L/0.33 wt% Si_3N_4; b) 316L/1 wt% Si_3N_4.*

The EDS spectra combined with SEM image with selected spots for EDS are presented in Fig. 5.25. The good dispersion and coverage of the nanosized ceramic particles (Si_3N_4) on the surface of the stainless steel grains were investigated by electron microscopy. Spot 1 represents the 316L matrix. Presence of small particles (spot numbers 2 and 3) embedded in the steel grains surface is shown by SEM, the EDS spectra confirmed that these dark spots are a mixture of Si_3N_4, and oxides are also present (Fig 5.25). The small bright particles on the grain surface (spot numbers 4 and 5) are steel particles as it is shown in the EDS spectra.

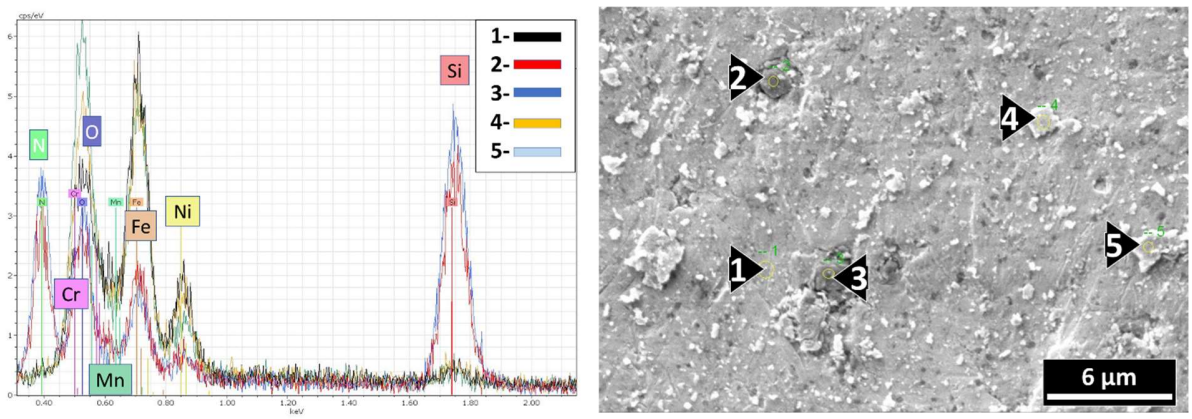

a) b)

***Fig. 5.25.** Investigation of the 316L/0.33 wt% Si_3N_4 composite: a) Elemental composition measurements by EDS, b) SEM image.*

In the case of the second mixture (316L+1wt% Si_3N_4, Fig. 5.26), I also noticed the good dispersion and coverage of the nanosized Si_3N_4 on the surface of the stainless steel grains but with

the presence of minor distributed phase (dark spots; spot number 2, 3, and 4) embedded in the steel grains (spot 1) as it is shown in the Fig. 5.26. The EDS spectra showed that this phase is a mixture of Si_3N_4 and possible silicon oxide. The bright spot (number 5) has lower amount of Si_3N_4 and higher amount of oxide phases as shown by EDS.

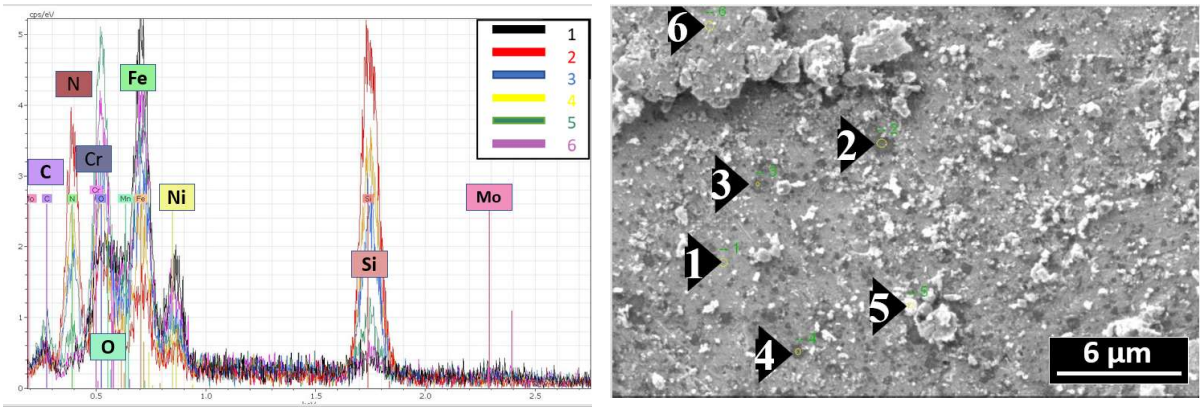

a) b)

***Fig. 5.26**. Investigation of the 316L/1 wt% Si_3N_4 mixture: a) Elemental composition measurement by EDS, b) SEM image.*

The EDS spectra (Fig. 5.27a) and SEM image (Fig. 5.27b) are showing the surface of the sintered 316L/0.33 wt% Si_3N_4 where spot 1 is the 316L matrix and spot 2 is silicon nitride with small amount of oxygen (silicon oxide). The spot 3 and 5 were confirmed as silicon oxide (dark phases) with a small amount of nitrogen and carbon presence. In spot 4, no nitrogen was detected only silicon and oxygen which resulted some oxide phase. I noticed an increase in the dark spots size due to the agglomeration of the silicon nitride and silicon oxide during the sintering process.

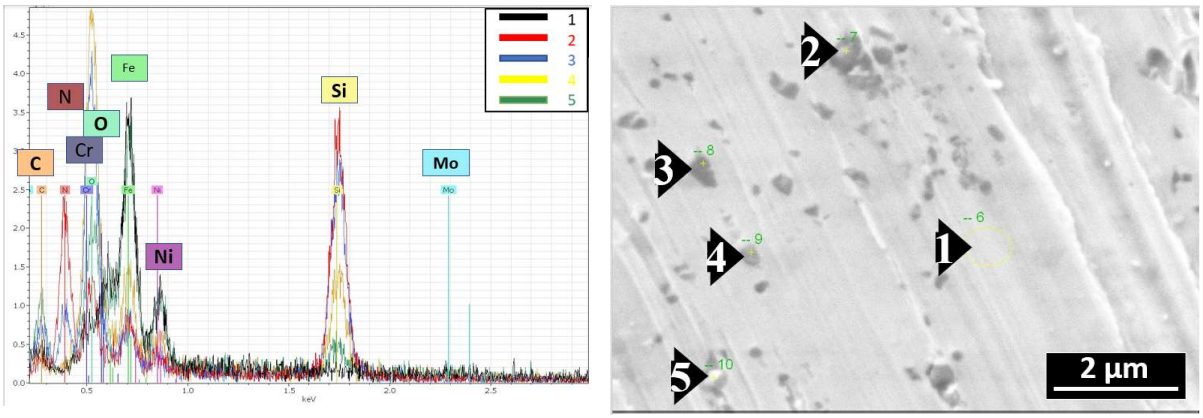

a) b)

***Fig. 5.27.** Investigation of the 316L/0.33 wt% Si_3N_4 sintered sample's surface. a) elemental composition measurement by EDS. b) SEM image.*

In the case of the 316L/1 wt% Si_3N_4, I noticed the increased presence of well distributed minor phase (dark spots). The EDS spectra (Fig. 5.28a) and fracture surface observed by SEM (Fig. 5.28b) showed the presence of silicon, nitrogen, oxygen, and carbon elements.

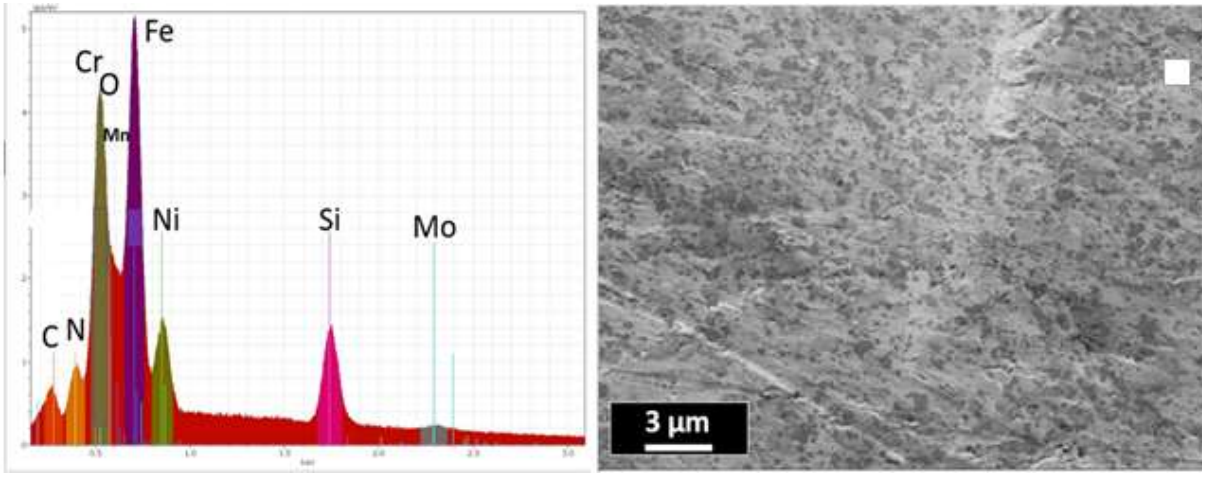

a) b)

Fig. 5.28. *Investigation of the 316L/1 wt% Si_3N_4 sintered sample's surface. a) elemental composition measurement by EDS. b) SEM image.*

Fig. 5.29a shows the microstructure of the 316L/1 wt% Si_3N_4 composite in more detail. I observed the presence of two different phases (A'and A"). It is interesting to compare the micro-hardness of the two phases (Fig 5.29a); an average of HV ~ 2.53 ± 0.17 GPa has been measured for the A' phase and 7.03 ± 0.41 GPa for the A" phase. In order to define the two phases and understand the microhardness results, I investigated the boundary between the two phases (as in the yellow square in the Fig. 5.29a-b and EDS elemental mapping in Fig. 5.29c). The side 1 (A') of Fig. 5.29c shows the austenitic 316L steel with good distribution of silicon, nitrogen and very small amount of oxygen; however, the side 2 (A") of Fig. 5.29c shows a very high concentration of the silicon, nitrogen, and oxygen. From this elemental composition I resulted that the phase (A") is a combination of silicon oxide and silicon nitride and these phases explained its higher hardness results.

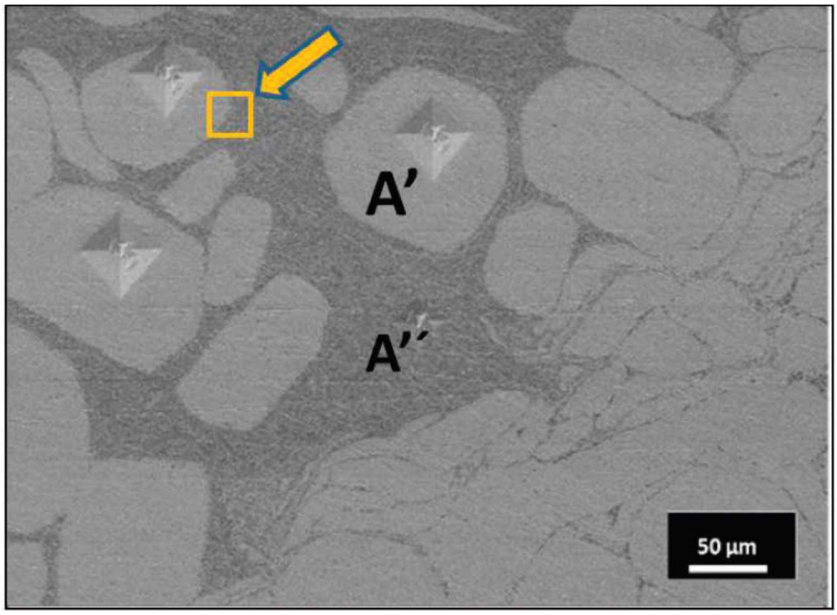

a)

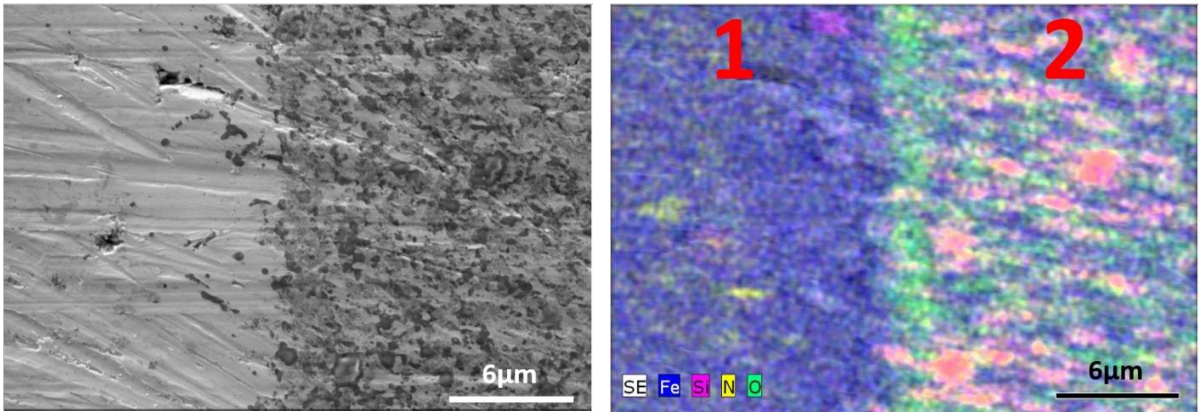

b) c)

Fig 5.29. *Structural characterization of 316L/1 wt% Si_3N_4 sintered sample. a) SEM image, b) detail marked by arrow in a) and c) elemental map.*

The starting powders, the milled powder mixtures and the sintered samples with two different amounts of the ceramic addition have been investigated by XRD in order to analyze the present phases. The XRD results are shown in Fig 5.30. In the case of 316L/0.33 wt% Si_3N_4 (Fig. 5.30a), the XRD confirmed that the starting powder is austenitic phase of γ-Fe_3Ni_2 phase (JPC2:03-065-5131) with main 2θ lines 43.532°, 50.705°, 74.535°. I observed the same γ-Fe_3Ni_2 with the presence of minor ferrite α-Fe phase (JCP2: 03-065-4899) represented by characteristic 2θ lines 44.663°, 65.008°, 82.314° after milling of ceramic with steel alloy. The presence of this ferrite phase might be due to the contamination from the milling setup (tank, balls, agitator). The

very high peak at 2θ = 69° characteristic for Si may be eliminated as contamination from the sample holder used for XRD measurement. After sintering, the ferrite α-Fe lines cannot be observed. In the case of the 316L/1 wt. % Si_3N_4 (Fig 5.30b), the XRD measurement confirmed that the main phase in the starting powder, the mixture (milled powder), and the sintered sample as well was the austenite γ-Fe_3Ni_2.

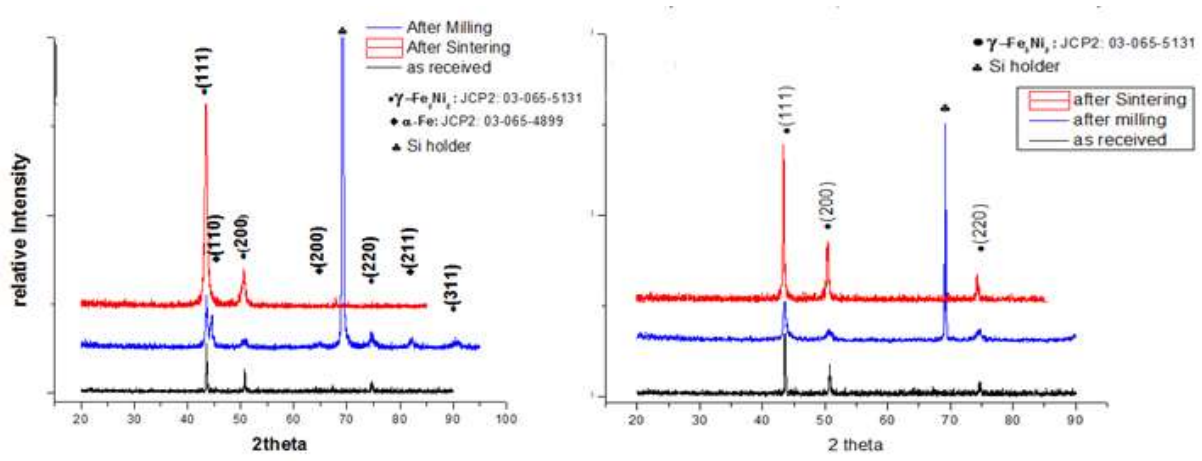

a) *b)*

Fig. 5.30*. XRD measurement of austenitic powders as received, after milling and after sintering. a) 316L/0.33 wt% Si_3N_4; b) 316L/1 wt% Si_3N_4.*

The structural observations of two sintered samples 316L/ 0.33 wt% Si_3N_4 and 316L/1 wt% Si_3N_4 clearly demonstrate the efficient coverage of steel grains by ceramic particles in both cases (Fig 5.31). In the case of 316L/0.33 wt% Si_3N_4 composite, I obtained the structure with finer grains than for 1 wt% Si_3N_4 addition showing a coarser grain structure. This observation is in agreement with structural observations presented in Fig. 5.22 - 5.23, Fig. 5.25 - 5.26, and Fig. 5.28 - 5.29.

The friction coefficient curves were measured for 12 hours (Fig. 5.32). A perturbation in the friction coefficient has been observed in all cases. After analyzing the curves, I noticed that the perturbation started by a drop in the friction coefficient followed by immediate increase of its value. A mean friction coefficient of ~ 0.962 (Fig. 5.32a) has been recorded in the case of the reference sample. The 316L/1wt% Si_3N_4 (Fig. 5.32b) and the 316L/0.33 wt% Si_3N_4 (Fig. 5.32.c) composites showed a lower value of the friction coefficient due to their higher hardness, the recorded mean values 0.818 ± 0.62 and 0.803 ± 0.039 have been recorded for the 316L/0.33 wt% Si_3N_4 and the 316L/1 wt% Si_3N_4 respectively.

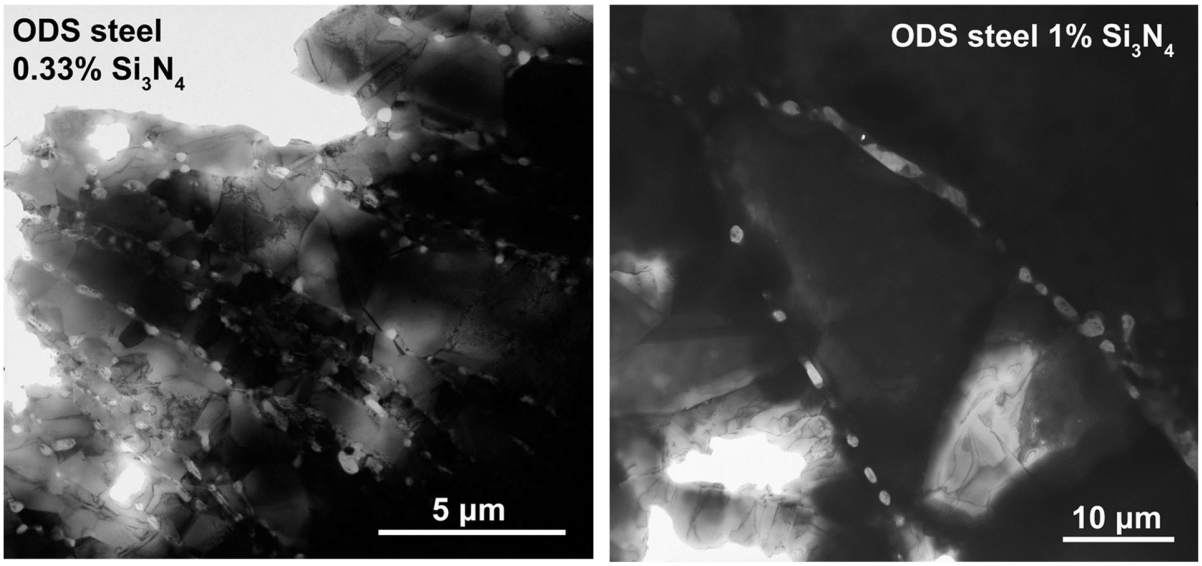

a) b)

Fig. 5.31. *TEM images of sintered samples. a) 316L/0.33 wt% Si_3N_4; b) 316L/1 wt% Si_3N_4.*

The perturbation (down and up striations) in the friction coefficient observed in both cases was related to the debris formation. The evolution of a metallic debris (in form of 316L powder) on the sample surfaces is presented in Fig. 5.33. The decrease in the friction coefficient (Fig. 5.32) is taking place when the removed steel grains are stuck under the Si_3N_4 ball and acting as a temporary lubricant before being ejected by the centrifugal force (Fig. 5.33). This removal of the steel grains from the path of Si_3N_4 balls caused an increasing of the friction coefficient. The damaged surface on the reference sample after the tribology measurement up to 2161m is shown in Fig. 5.34a. The higher magnification of the damaged area (Fig. 5.34b) showed the presence of Si_3N_4 originating from the damaged ball (Fig. 3.35a) embedded in the sample surface and forming a tribolayer.

The investigation of the damaged ball (Fig. 5.35a) showed the presence of embedded 316L particles on the eroded ball surface (Fig. 5.35b). The Fig. 5.36a shows the damaged surface on the 316L/1wt % Si_3N_4 sample. The wear track is not symmetrical to the rotation axis because this last slightly shifting from its position during the measurement. The higher magnification of the damaged area (Fig. 5.36b) shows high erosion of the surface together with Si_3N_4 originating from the damaged ball (Fig. 5.37a) embedded in the sample surface.

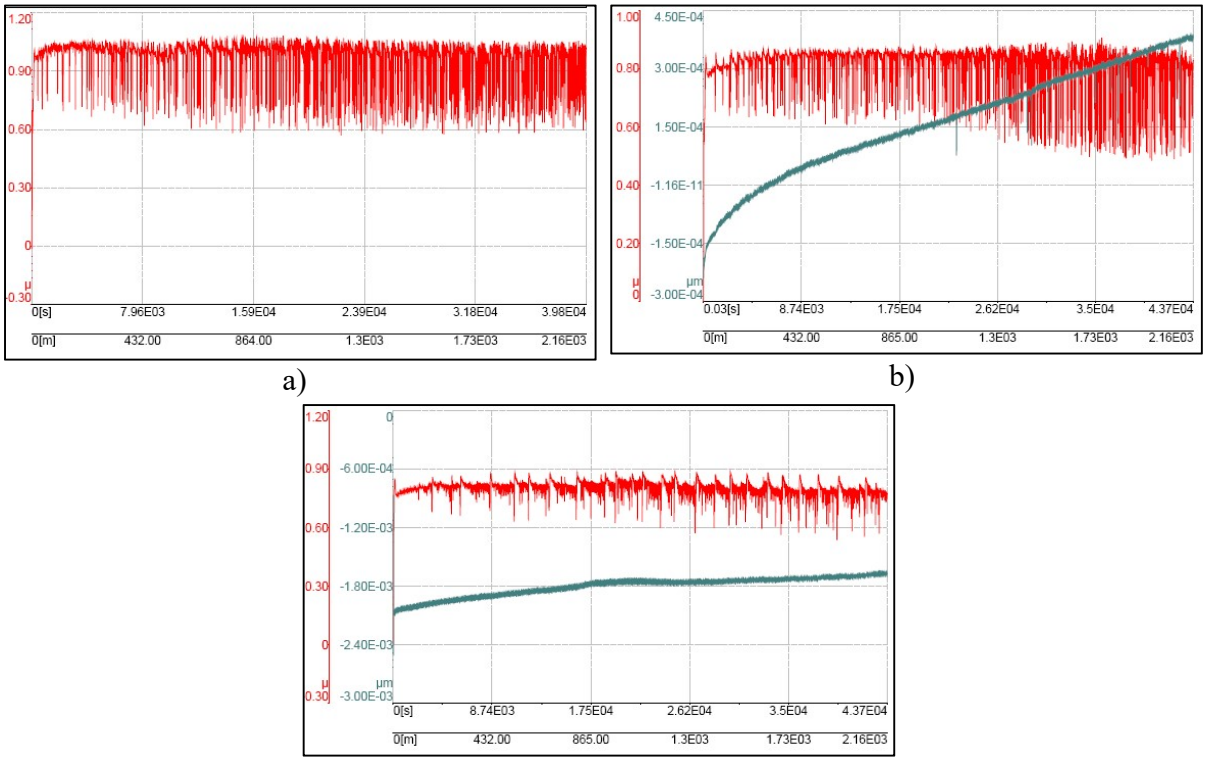

***Fig. 5.32**. Friction coefficient curves after 12hours measurement (2161m). a) 316L reference sample, b) 316L/ 0.33 wt% Si_3N_4. c) 316L/ 1 wt% Si_3N_4.*

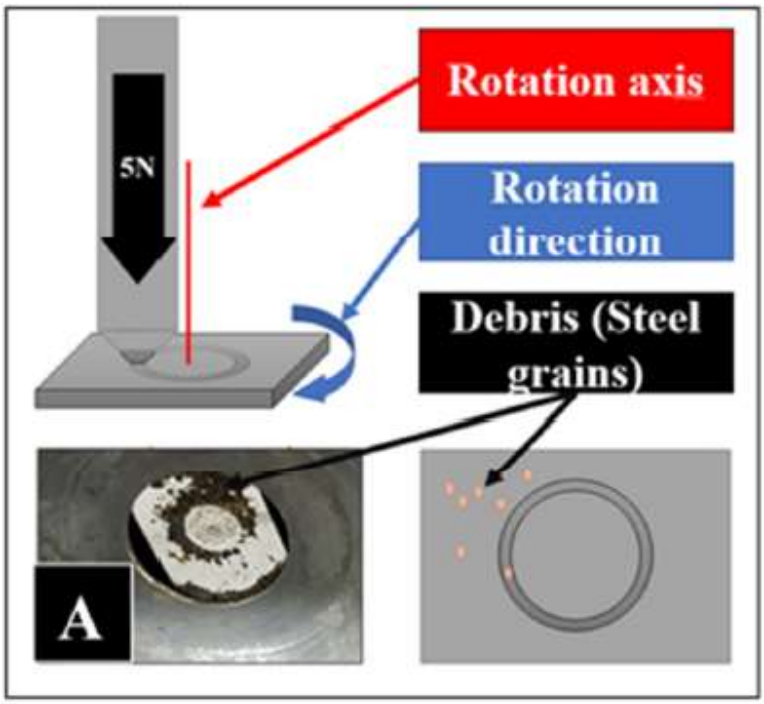

***Fig. 5.33**. Schematic representation of the debris formation.*

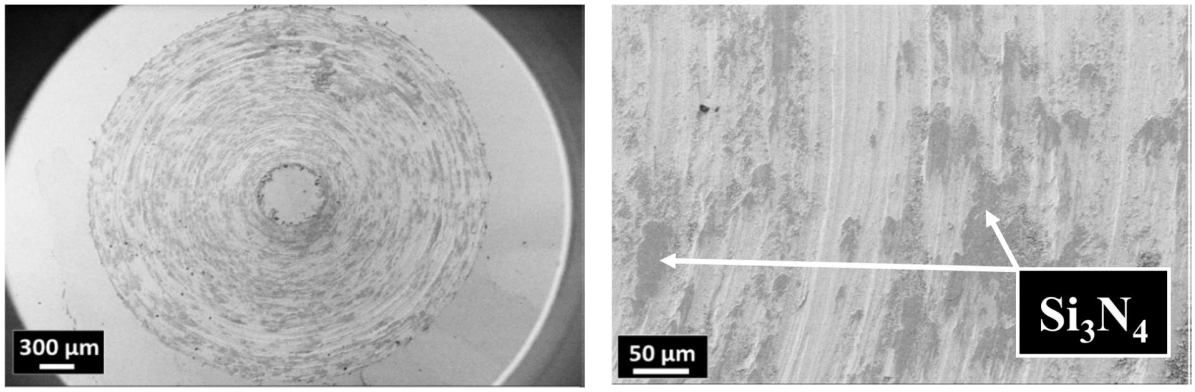

a) b)

Fig. 5.34. *SEM images of the 316L/0.33 wt% Si_3N_4 surface damage after 12 hours tribology measurement. a) tribology wear track, b) higher magnification of the wear track.*

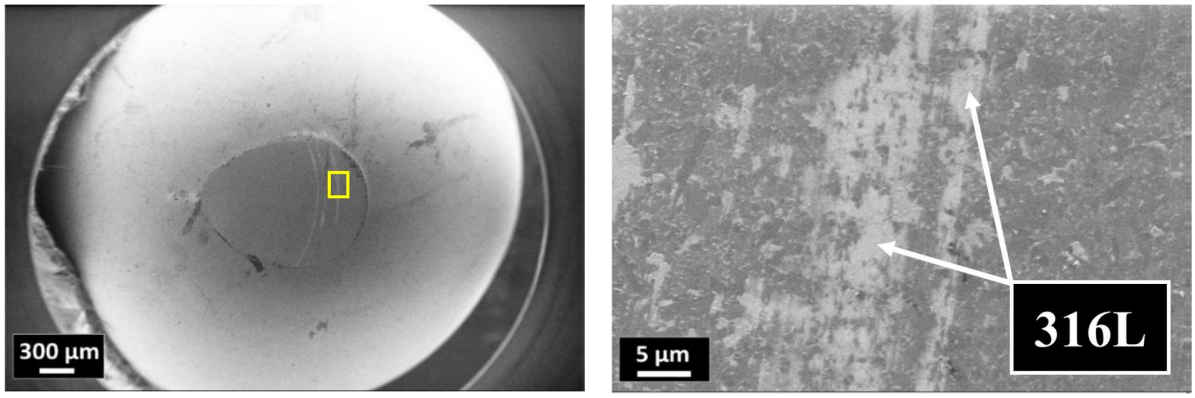

a) b)

Fig. 5.35. *SEM images of a) the damaged Si_3N_4 ball, b) higher magnification of the selected area on (a).*

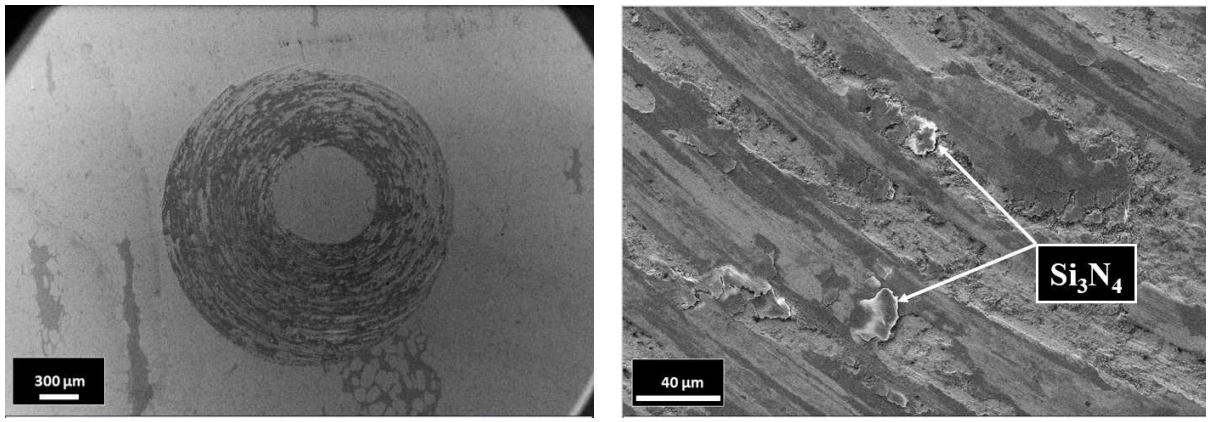

a) b)

Fig. 5.36*. SEM images of the 316L/1wt% Si_3N_4 surface damage after 12 hours tribology measurement. a) tribology wear track, b) higher magnification of the wear track.*

The investigation of the damaged ball (Fig. 5.37a) showed the presence of embedded 316L steel particles on the eroded ball surface (Fig. 5.37b).

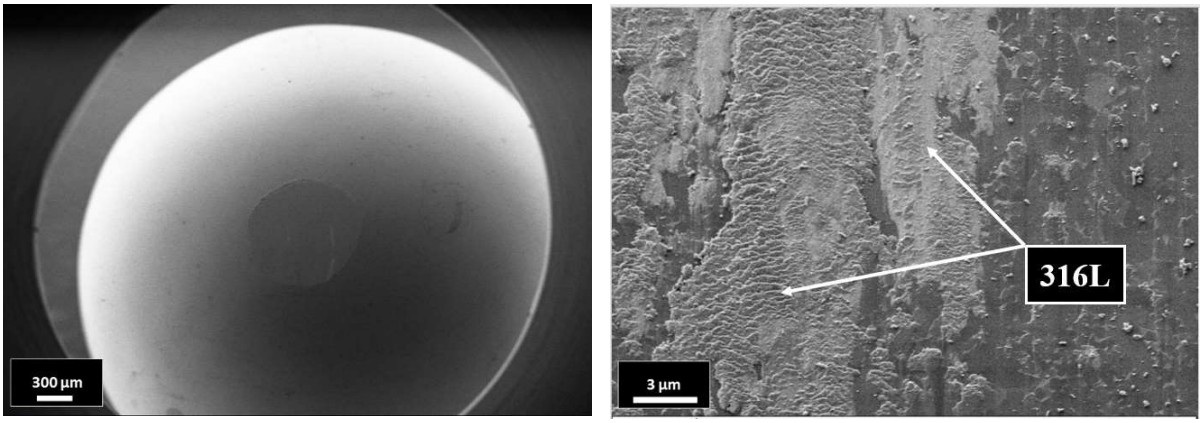

a) b)

Fig. 5.37. *SEM images of the tribology counterpart a) the damaged Si_3N_4 ball, b) higher magnification of the selected area on (a).*

The density of the 316L composites decreased with increasing Si_3N_4 addition (Fig. 5.38). The addition of Si_3N_4 increased the microhardness of the 316L composite compare to reference 316L sample. On the other hand, 1 wt% Si_3N_4 addition resulted in the overall lower microhardness (2.69 GPa) comparing 0.33 wt% Si_3N_4 (3.34 GPa, Fig. 5.38).

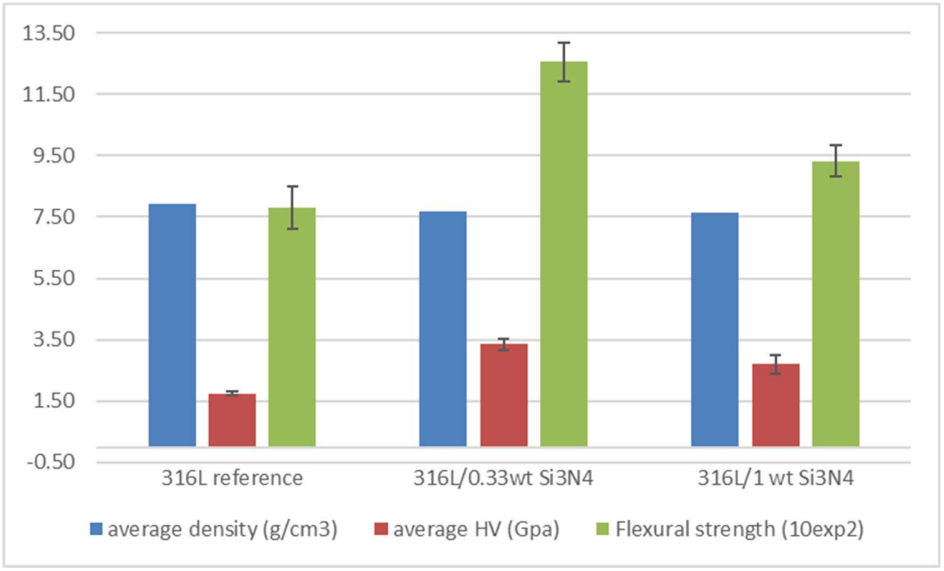

Fig. 5.38*. Density, microhardness, and flexural strength comparison.*

The decrease in the flexural strength in the case of 316L/1 wt% Si_3N_4 (931.8 MPa) comparing to the 316L/0.33 wt% Si_3N_4 (1255 MPa) is due to the induced morphological changes after milling as it was explained above.

Conclusions

The effect of the submicrometer sized Si_3N_4 addition on the morphological and structural properties of the ceramic dispersion strengthened (CDS) 316L stainless steels prepared by powder technology has been studied. Two composites were prepared: 316L/0.33 wt% Si_3N_4 and 316L/1 wt. % Si_3N_4. In order to assure a good dispersion of the ceramic particles in the stainless steel powders and a grain size reduction at the same time, the highly efficient attrition milling has been used. It has been found that 5 h of milling in ethanol at 600 rpm using 3 mm grinding stainless steel balls was sufficient to obtain grains with flake-like shape in case of 316L/0.33 wt% Si_3N_4. SPS was used for fast sintering of milled composites. The samples have been sintered under 50 MPa at 900 °C for 5 min in vacuum. Structural and morphological changes were studied after milling and sintering process. I found that the amount of Si_3N_4 addition influenced the efficiency of milling process resulting in powder mixtures with different 316L stainless steel grain size and shapes. In the case of 0.33 wt% Si_3N_4 addition, the flat 316L stainless steel grains with submicrometer size in thickness have been resulted after milling compared to 1 wt. % Si_3N_4 added powder mixtures which consisted of almost globular 316L stainless steel grains with 50‑100 μm in diameter. The intensive milling assured an optimal coverage of 316L stainless steel grains with Si_3N_4 submicrometer sized particles in both cases as demonstrated by EDS and TEM. On the other hand, the 316L phase has been maintained during and after the milling and sintering. The partial phase transformation of α-Si_3N_4 to SiOx was observed during sintering by EDS.

5.4. Investigation of 316L/ Y_2O_3 composites

In this part, the 316L austenitic steel based milled and sintered composites with 0.33 wt% and 1 wt% Y_2O_3 nanoparticle addition were prepared. The investigation of the atomised 316L stainless steel starting powder by SEM (Fig. 5.39a) shows that it is consisted of ~70 μm globular shape grains with the presence of satellites on their surface.

The Y_2O_3 powder (Fig. 5.39b) is consisting of a flake-like shaped grains with ~700 nm particle size in average. The globular shape grains of 316L starting powder has been transformed into 4 types/shapes (as in Fig. 5.1b, 1-slightly damaged, 2-flattened, 3-flake-like shape and 4-small broken grains) due to the high impact forces implemented by the steel balls during the 5 hours milling. The impact of steel balls is higher in the bottom part of the milling jar comparing the top part, that is why we have different grains morphologies.

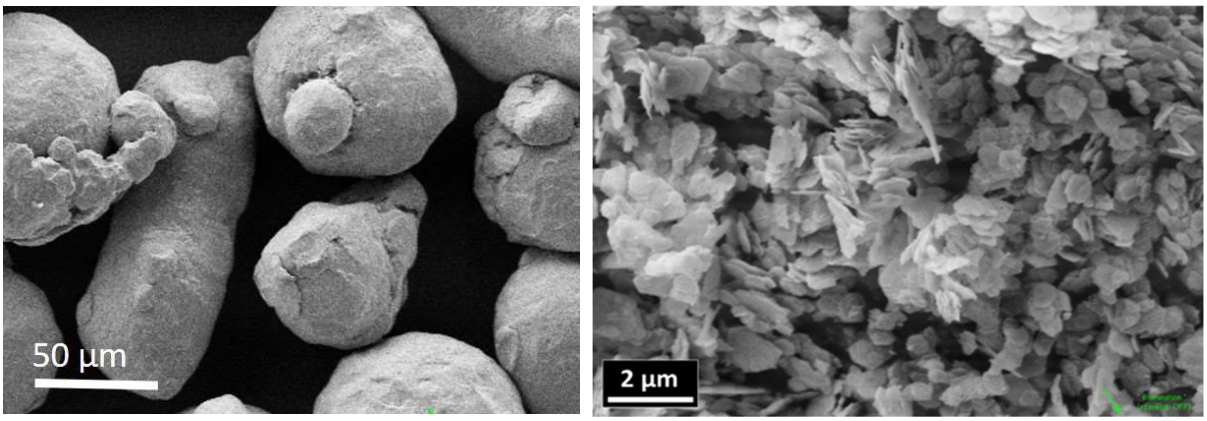

a) b)

Fig. 5.39. *SEM images of the starting powders. a) 316L, b) Y_2O_3.*

The ratio of flake-like shape grains to the flattened and slightly damaged grains is bigger in the case of the Y_2O_3 additions (Fig. 5.40a and Fig. 5.41a) comparing to milled 316L powder (Fig. 5.1b). The presence of the Y_2O_3 is clearly shown on the EDS spectra of the milled composite powders (Fig. 5.40b and Fig. 5.41b). The yttria particles were embedded into the surface of the 316L steel grains making it harder, this increased the impact of milling balls which in turn increased the evolution of flake-like grains.

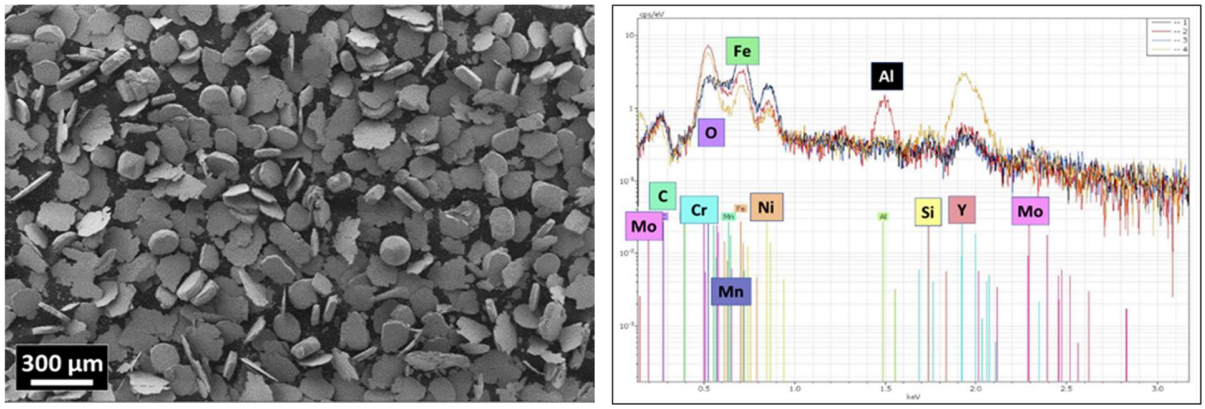

a) b)

Fig. 5.40. *Investigation of the milled 316L/0.33 wt% Y_2O_3 powder mixture. a) SEM image b) EDS spectra.*

The milling efficiency was slightly decreased in the case of the 316L/1 wt% Y_2O_3 composite comparing to the 316L/0.33 wt% Y_2O_3 because the yttria particles agglomerated together which influenced (decreased) the milling efficiency.

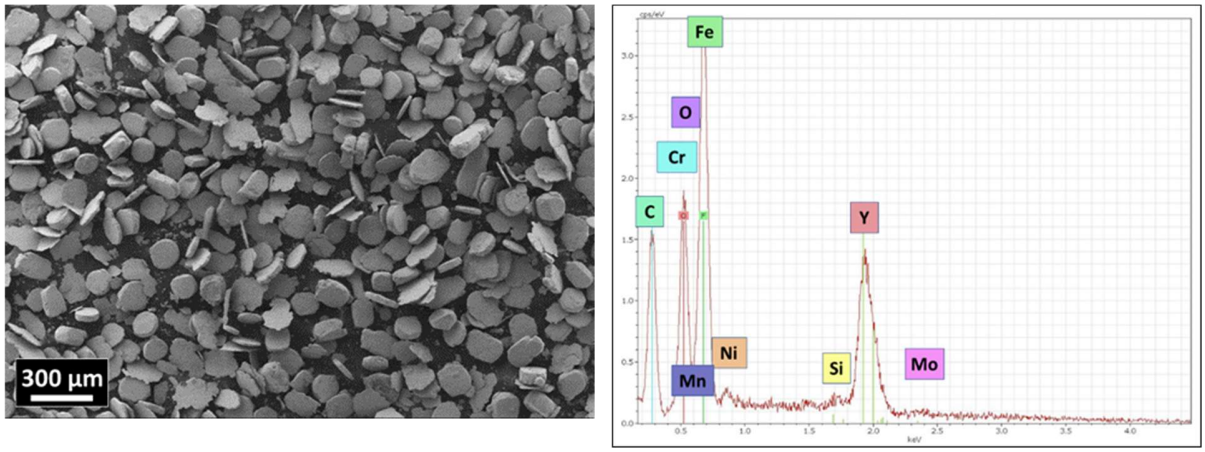

a) b)

Fig. 5.41. *Investigation of the milled 316L/1 wt% Y_2O_3 powder mixture. a) SEM image, b) EDS spectra.*

The XRD results (Fig. 5.42) confirmed that the 316L starting powder is an austenitic powder of ɣ- Fe_3Ni_2 phase (JPC2:03-065-5131) with main lines of (2θ = 43.532º, 50.705º, 74.535º). After milling, I noticed the presence of the ferrite α -Fe phase (JCP2: 03-065-4899) with the characteristic 2θ lines 44.663º, 65.008º. The Y_2O_3 phase (JCPDFWIN 00-041- 1105) with 2θ= 29.150°, 48.541º was clearly detected in the case of the 316L/1 wt% Y_2O_3 milled powder. The presence of Si peak at 2θ= 6° from sample holder was observed.

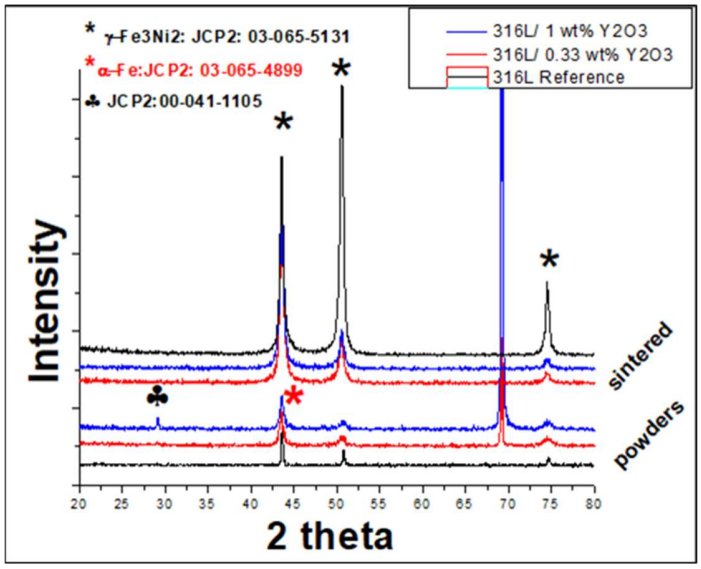

Fig. 5.42. *XRD diffractograms of the starting 316L powder, milled powder mixtures and sintered composites.*

After the sintering process, the ferritic α-Fe phase has been transformed to the austenitic ɣ-Fe_3Ni_2 phase as it was expected. The Y_2O_3 peaks disappeared after sintering. In the case of the reference 316L sample we noticed a reorientation in the direction [200] of the grains after sintering (Fig. 5.42). The sintered sample has the fully densified structure and surface with some inhomogenity and submicron sized roughness (Fig. 5.43a). The elemental composition of the sintered 316L/0.33 wt% Y_2O_3 show the presence of small amount of Y_2O_3 in the composite (Fig. 5.43b). This finding is indicating some diffusion or agglomeration of the yttria particles in the steel matrix, resulting in the decrease of the Y peak intensity in the sintered composite comparing the milled powders.

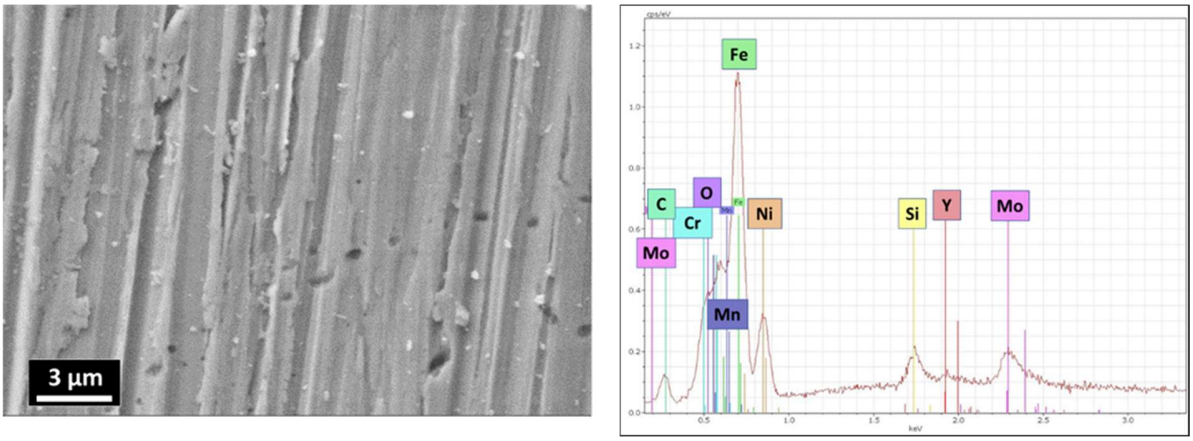

a) b)

Fig. 5.40. *sintered 316L/0.33 wt% Y_2O_3 a) SEM image, b) EDS spectra.*

The Y element was not detectable by EDS measurement in the case of the 1 wt% Y_2O_3 addition (Fig. 5.44b). It can be resulted of the non-homogeneous distribution of the yttria in the steel matrix created the agglomeration of yttria particles during the sintering process (Fig. 5.44b). The detailed structural observation of the sintered composites was studied by TEM measurements (Fig. 5.45). In the case of 0.33 wt% Y_2O_3 addition (Fig. 5.45a), we observed the relatively small steel grains of ~ 5-20 µm with a good and homogeneous distribution of the Y_2O_3 in the grain boundaries. The yttria particles are agglomerated together in higher 1 wt% Y_2O_3 ceramic addition (Fig. 5.45b). Micrometer sized twinned regions can be distinguished in the steel grains in both composites.

After tribology investigation both Si_3N_4 ball and the samples surfaces have been damaged. The damage on the ball was insignificant. The wear track width and depth have been measured for wear volume calculation. The wear rate of the 316L reference, 316L/ 0.33 wt% Y_2O_3 and the 316L/ 1 wt% Y_2O_3 have been calculated (Tab 5.1).

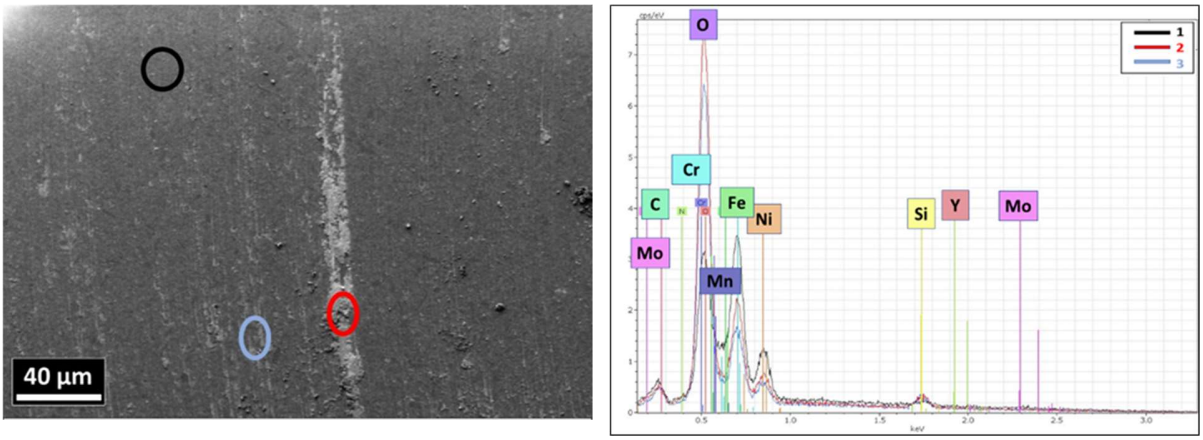

a) b)

Fig. 5.44. *Investigations of the sintered 316L/1 wt% Y_2O_3 composite. a) SEM image, b) EDS spectra.*

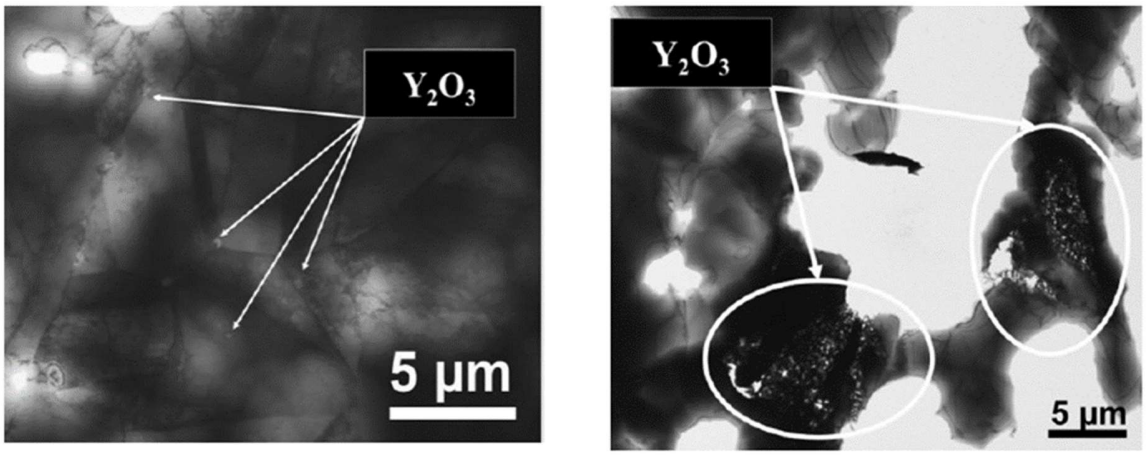

a) b)

Fig 5.45*. TEM images of the sintered composites. a) 316L/0.33 wt% Y_2O_3, b) 316L/1 wt% Y_2O_3.*

Table 5.1 *The wear rate of the sintered composites.*

	316L	316L/ 0.33 wt% Y_2O_3	316L/1 wt% Y_2O_3
Wear rate (m^2/N)	1.36177E-4	5.39844E-14	2.40614E-14

The wear rate has been reduced significantly with the addition of yttria to the matrix. The investigation of the damaged surfaces shows the formation of tribofilms on the sample's surfaces (Fig. 5.46a and Fig. 5.47a). No yttrium content was detected by EDS on the wear track of the two composites (Fig. 5.46b and Fig. 5.47b).

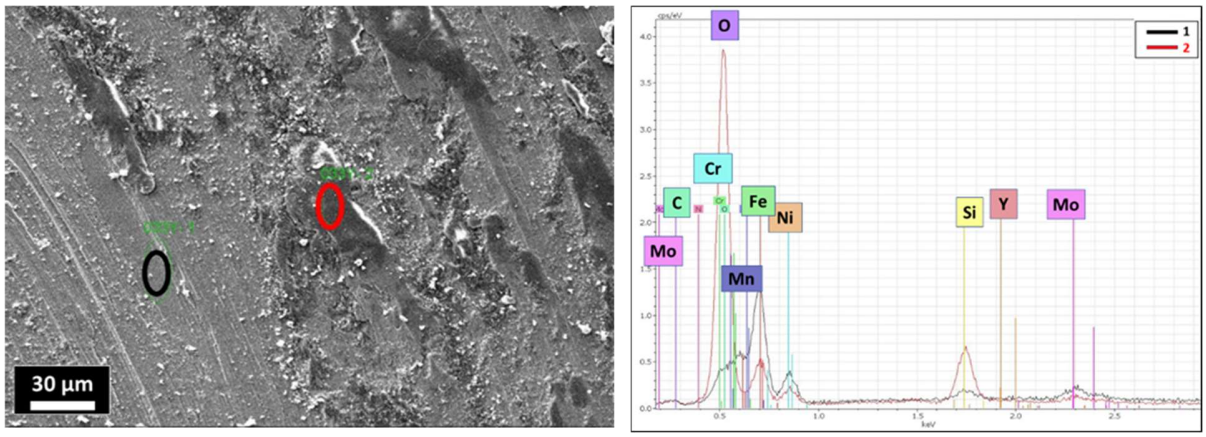

a) b)

Fig. 5.46. *Investigations of the sintered 316L/0.33 wt% Y_2O_3 composite. a) SEM image, b) EDS spectra.*

High content of oxygen and silicon were measured in the same spot of the tribofilm in both composites, which can be explained by the formation of silicon oxide during the tribology test. Silicon oxide formation is a result of temperature increase in the contact zone as a result of a relatively high sliding speed. The lower intensity peaks of the 316L components in zone 2 (Fig 5.47b and Fig. 5.48b) is due to the coverage of 316L composite by the tribo-film. The friction coefficients are represented in Fig. 5.49. The 316L/Y_2O_3 composites are showing higher densities comparing with the elaborated 316L/Si_3N_4 composite elaborated using the same parameters. The Y_2O_3 addition increased the hardness of composites compare to 316L reference (Fig. 5.49) The HV values 1.75±0.05 GPa (316L reference), 2.63±0.32 GPa (316L/0.33 wt% Y_2O_3) and 2.33± 0.165 GPa (316L/1 wt% Y_2O_3) have been measured. The friction coefficient dropped with addition of Y_2O_3. The value 0.962 ±0.108 was registered for the 316L reference sample, 0.863±0.078 for the 316L/ 0.33 wt% Y_2O_3 and 0.806±0.083 for the 316L/1 wt% Y_2O_3.

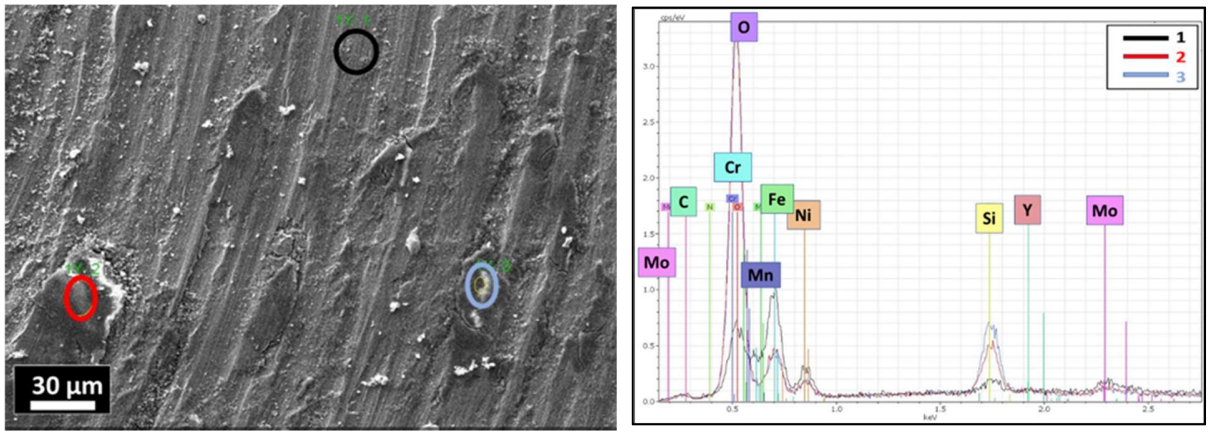

a) b)

***Fig. 5.41**. Investigation of 316L/1 wt% Y_2O_3 sintered composite after tribological measurements. a) SEM image, b) EDS spectra.*

316L	ρ (g/cm³)	7.93
	HV (GPa)	1.75
	σ (MPa)	781
316L / 0.33 wt% Y_2O_3	ρ (g/cm³)	7.89
	HV (GPa)	2.63
	σ (MPa)	974
316L / 0.33 wt% Y_2O_3	ρ (g/cm³)	7.86
	HV (GPa)	2.33
	σ (MPa)	736

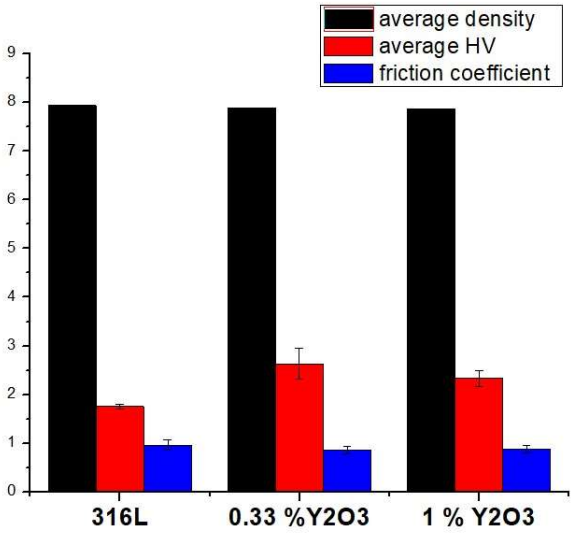

***Fig 5.48**. Mechanical properties of composites vs. 316L reference.*

In the case of the 316L/0.33 wt% Y_2O_3 composite, the samples were ductile and behaved like the reference samples, where the samples just bent and didn't break, unlike the case of the 316L/1 wt% Y_2O_3 where the samples showed different behaviors during the 3-point bending test, 2 out of five samples were brittle and broke during the test, where the remaining 3 samples were ductile and just were bent. It can be expected that this mixed behaviour was resulted to the non-homogeneous distribution of the yttria during the milling process (Fig 5.45b).

The milling efficiency has been improved with the addition of the yttria as it observed clearly in Fig. 5.40a and Fig. 5.41a where the ratio of the flake-like shape grains to the slightly damaged and flattened grains is higher comparing to the milled reference 316L powder (Fig. 5.1). This improvement in the milling efficiency is attributed to the yttria addition which increased impact effect by hardening surface of the steel grains.

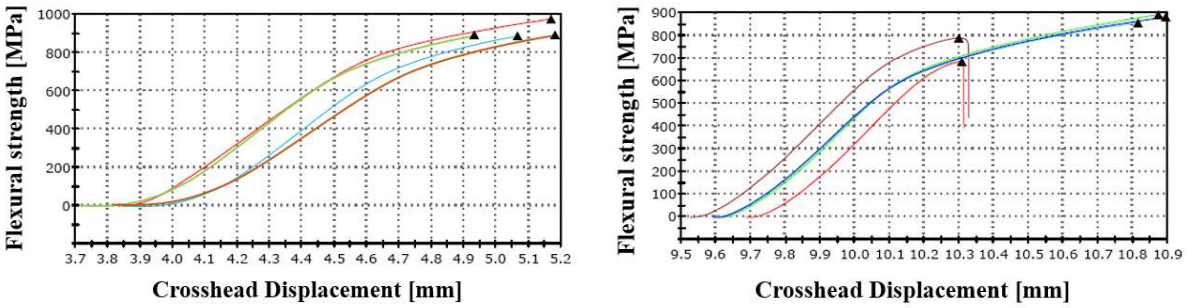

a) **b)**

Fig. 5.49*. 3-point bending test results. a) 316L/0.33 wt% Y_2O_3 b) 316L/1 wt% Y_2O_3.*

The EDS spectra of the milled powder with high intensity yttrium peak (Fig. 5.41b) and the milled powder X-ray diffractograms (Fig. 5.42) show the presence of Y_2O_3 in the 316L/1 wt% Y_2O_3 composite. In the case of sintered samples, no yttria peaks in the XRD and EDS may be observed (Fig. 5.42 and Fig. 5.44b, respectively). This finding proves that the agglomeration of the yttria particles in the 316L/1 wt% Y_2O_3 composite (Fig. 5.45b) took place during the sintering process.

The presence of the ferrite α-Fe phase in the milled composites is a result of an austenitic-martensitic/ferritic transformation during the milling process due to the severe deformation under the high impact of the milling balls or it is due to a contamination from the milling setup. The ferrite phase was transformed to the ɣ-Fe_3Ni_2 as it is shown in Fig. 5.42. Two main lines of yttria have been clearly identified in the case of the 316L/1 wt% Y_2O_3 (Fig. 5.42) unlike in the case of the 316L/ 0.33 wt% Y_2O_3 where the yttria content was under the detection limit. The distribution of the yttria particles in the 316L/1 wt% Y_2O_3 composite is not homogeneous as we can observe in Fig. 5.46b. The TEM results are in correlation with EDS and explain the disappearance of the yttria content in the 316L/1 wt% Y_2O_3 sintered composite (Fig. 5.42). The yttria content slightly dropped the density, however, the 316L/Y_2O_3 composites are showing higher densities comparing to similar composites made by the 3- Dimensional Fiber Deposition (3DFD) technique even when higher sintering temperatures were applied [50]. The prepared 316L/Y_2O_3 composites are showing higher hardness values comparing to the 316L/0.4 wt% Y_2O_3 prepared by electron beam selective melting (EBSM) and Spark Plasma Sintering even after hot rolling [108].

The lower HV value of the 316L/1 wt% Y_2O_3 (2.33 GPa) comparing to the 316L/0.33 wt% Y_2O_3 (2.63 GPa, Fig. 5.48) is due to the non-homogeneous distribution of the yttria particles (Fig. 5.45b). The lower friction coefficient in the case of the 316L/Y_2O_3 composites comparing to the 316L reference sample is due to their higher hardness. The 316L/1wt% Y_2O_3 composite samples showed mixed behaviors during the 3-point bending test due to the difference in yttria content, where this last tends to agglomerate together during the milling process, unlike the case of the

316L/0.33 wt% Y_2O_3 where the yttria nanosized particles where homogeneously distributed but the content was not high enough to change the fracturing behavior.

Conclusions

The elaboration of yttria dispersed strengthened steel using attrition milling and spark plasma sintering has been demonstrated. The effect of changing chemical composition by addition of yttria to the 316L matrix on the structural and mechanical properties has been studied. The addition of yttria improved the milling efficiency. Agglomeration of the yttria particles took place during the sintering process in the case of the 316L/1 wt% Y_2O_3. The 316L hardness and tribological properties have been improved with the addition of yttria. The 316L/0.33 wt% Y_2O_3 show better mechanical properties comparing to the 316L/1 wt% Y_2O_3 and the 316L reference samples.

6. Summary and Conclusions

6.1. Structural properties of novel composites

The preparation, mainly the milling process have a strong effect on the structure of the composites. The morphological changes were observed after 5 hours high efficient milling in all types of novel CDS composites (Fig. 6.1). The reference sample consisted of 70 μm globular particles. During the milling process, the globular shaped-starting powders are plastically deformed/flattened into a very thin flake like shape grains (Fig. 5.1). These thin flake like shape grains are after that broken into smaller particles. As a result of the flattening behavior the average grain size increased. The type (SiC, Si_3N_4, Y_2O_3) and amount (0.33 wt%, 1 wt%) had influence on milling process and structure of final composite.

I estimated the milling efficiency by the ratio of the thin flake-like shape grains to the globular and the flattened grains. The addition of 0.33 wt% SiC (Fig 6.1c), 1wt% SiC (Fig 6.1d) or 0.33 Si_3N_4 (Fig 6.1e) showed the best milling efficiency results among the prepared composites (this is in comparison with the 316L milled powder). Followed by 0.33 wt% Y_2O_3 and 1 wt% Y_2O_3 addition. In the case of the 1 wt% Si_3N_4 addition there was no improvement of the milling efficiency comparing to the milled 316L steel powders.

The difference in the milling efficiency was mainly related to the following:

- The physical properties of the added particles. The density, hardness, size and morphology of the particles, these properties control the velocity, the dispersion of the added particles (top/middle/bottom of the milling jar) and the interaction with the steel grains under the impact forces.
- The chemical properties of the added particles, mainly the reactivity with ethanol and the 316L SS which influence directly the viscosity of the mixture and as the results the milling efficiency.
- The added ceramic particles are embedded in the surface of the steel grains under the strong impact forces which increases the hardness of the grain's surfaces, this last means that higher impact forces are transferred to the grain's cores. The plastic deformability of the grains increases significantly.

A homogeneous distribution of the added non oxide and oxide ceramic particles in the steel matrix was observed in all composites (Fig. 6.1.) except in the case of the 316L/ 1wt% Y_2O_3.

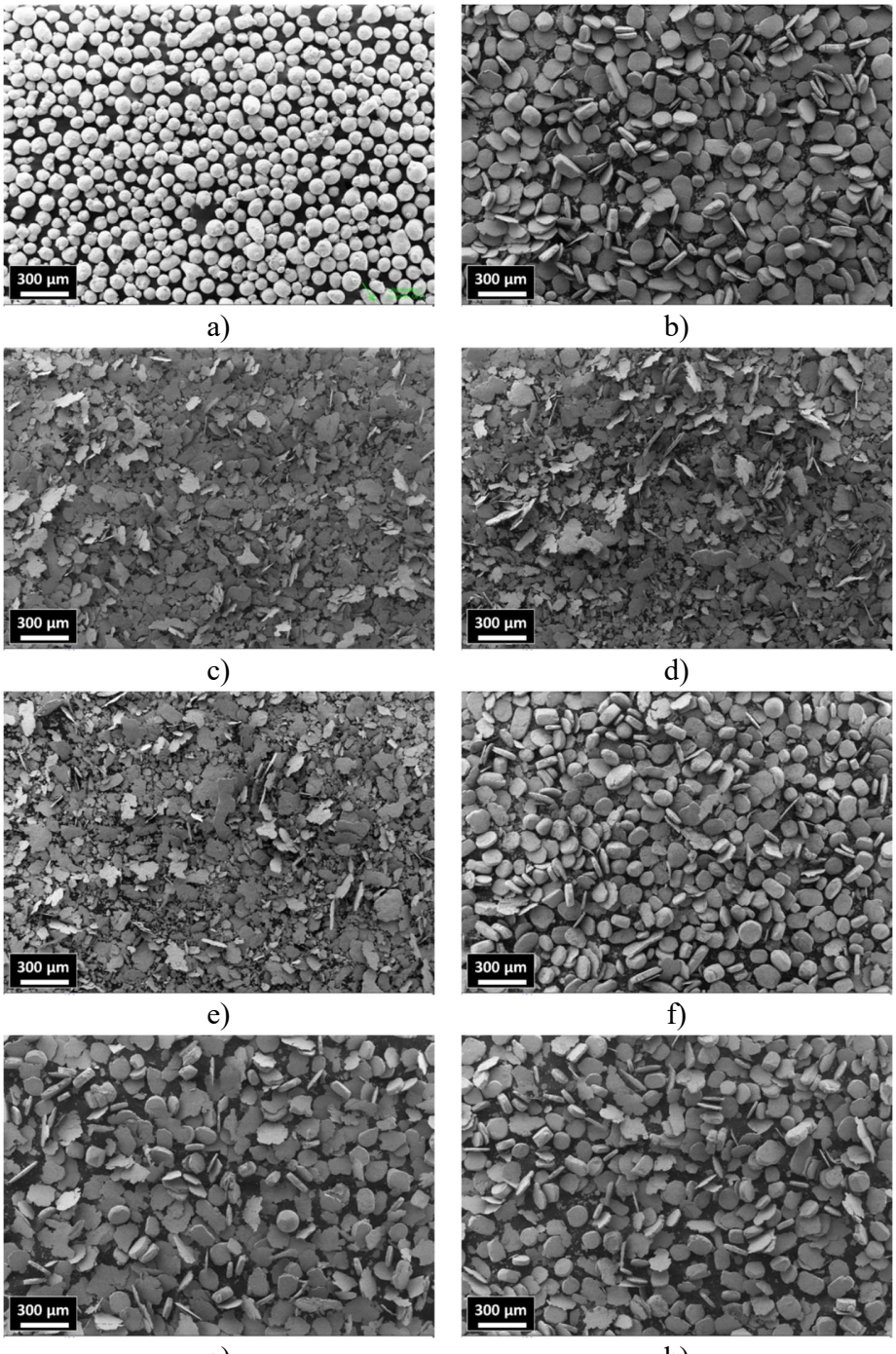

***Fig. 6.1**. Comparison of the morphology of milled powder mixtures and reference. a) 316L starting powder, b) milled 316L powder, c) milled 316L/0.33 wt% SiC, d) milled 316L/1 wt% SiC, e) milled 316L/0.33 wt% Si_3N_4, f) milled 316L/1 wt% Si_3N_4, g) milled 316L/0.33 wt% Y_2O_3, h) milled 316L/1 wt% Y_2O_3.*

The structural observation of the sintered composites showed the nanosized ceramic particles distributed along the grain boundaries in all cases (Fig. 6.2) except in the case of the 316L/1 wt% Y_2O_3 where the yttria particles are agglomerated together (Fig 6.3f).

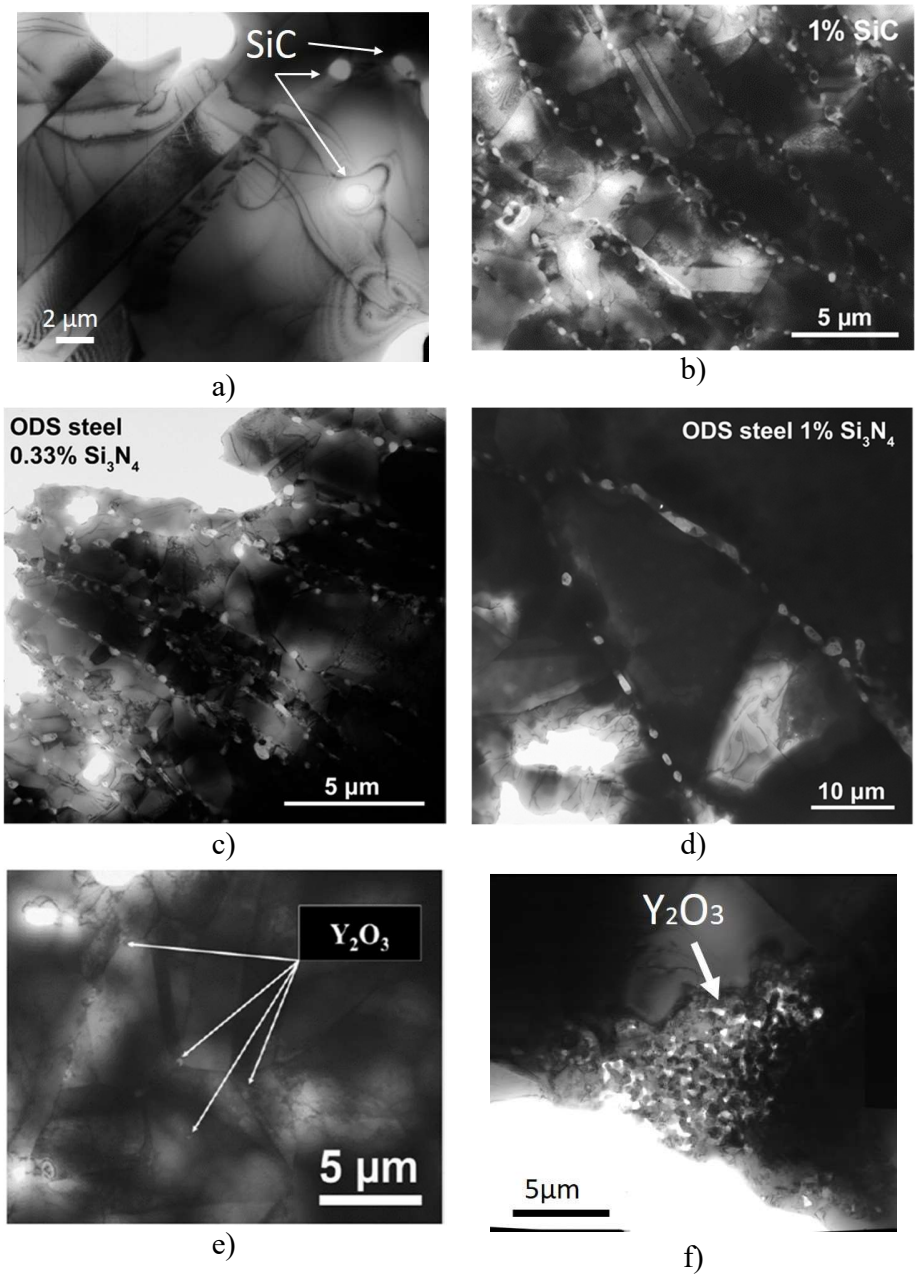

Fig 6.2. *TEM images of the sintered composites. a) 316L/ 0.33 wt% SiC. b) 316L/1 wt% SiC, c) 316L/0.33 wt% Si_3N_4, d) 316L/1 wt% Si_3N_4, e) 316L/0.33 wt% Y_2O_3, f) 316L/1 wt% Y_2O_3.*

6.2. Mechanical properties of CDS composites

The most important property of the novel CDS sintered composites is the mechanical property (Fig. 6.3). The main focus of my PhD work was the enhance of hardness and bending strength of CDS composites compared to the 316L reference.

The milled and sintered reference 316L showed the highest density values and the lowest microhardness value ~ 1.75 GPa. The 0.33wt% Si_3N_4 content caused the highest microhardness ~ 3.34 GPa. A very similar property was obtained by 0.33 wt% SiC addition with microhardness ~ 2.98 GPa. The 1 wt% SiC, Si_3N_4 and Y_2O_3 addition resulted the lower hardness, but almost 1.2-1.5 times higher than reference 316L; 2.79 GPa, 2.69 GPa and 2.33 GPa respectively.

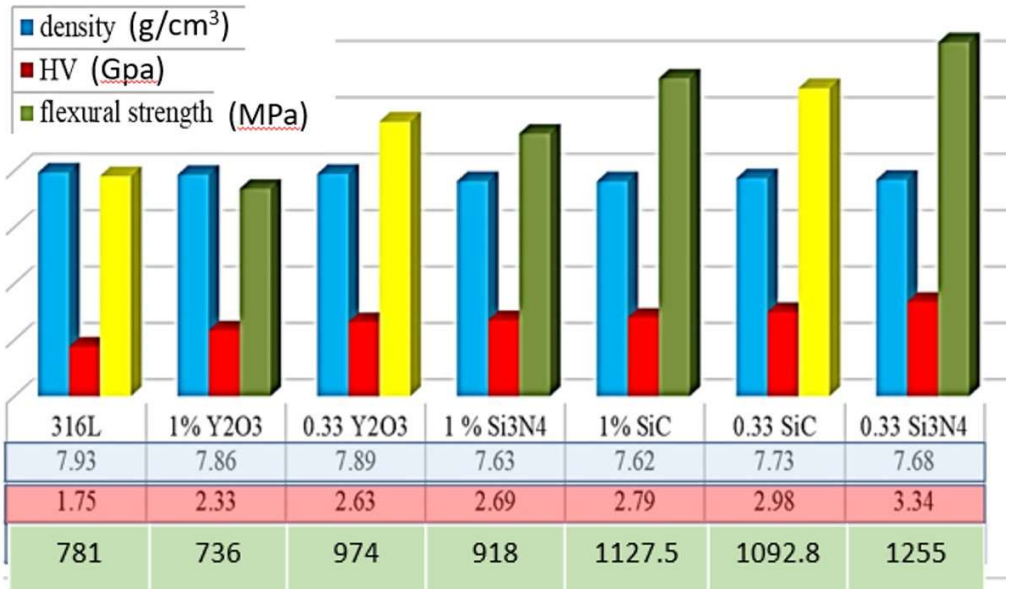

316L	1% Y2O3	0.33 Y2O3	1 % Si3N4	1% SiC	0.33 SiC	0.33 Si3N4
7.93	7.86	7.89	7.63	7.62	7.73	7.68
1.75	2.33	2.63	2.69	2.79	2.98	3.34
781	736	974	918	1127.5	1092.8	1255

Fig. 6.3. *Comparison of mechanical properties of final sintered composites and reference. The yellow bars in the chart means that the samples were broken during the 3-point bending test.*

The 0.33 wt% Si_3N_4 and SiC non oxide ceramic addition provided the best mechanical properties with the highest microhardness and flexural strength values. This was a result of two main factors:

- the complex grain boundaries formed by the thin flake-like shape grains and the smaller broken particles.
- the presence and the homogeneous distribution of the ceramic additives in the grain boundaries which increases the deformability resistance by blocking/slowing down the movement of dislocations and grain boundaries during the deformation process.

The employing the nanosized ceramic additions provides better mechanical properties at room temperature comparing to the composites with nanosized ceramic oxides, which is more promising for applications at high temperatures.

7. Thesis Points

1. **I showed that the combined attrition milling and the spark plasma sintering are promising methods for the novel ceramic dispersed stainless steel composites (CDS) preparation.** The wet attrition milling depending on ceramic content provided homogeneous distribution of the ceramic additives (Si_3N_4, SiC, Y_2O_3) in the steel 316L matrix and imposed significant morphological transformation. The short time consolidation by spark plasma sintering prevented the excessive grains growth and maintained the homogeneous distribution of the additives **[S1, S2, S3, S4, S5, S6].**

2. **I showed that the employment of well dispersed small amounts** (0.33 and 1 wt%) of the **nanosized SiC particles in the 316L SS matrix improves its mechanical properties significantly.** The nanosized SiC particles embedded in the 316L SS grains and covered them homogeneously which increased its surface hardness and improved the milling efficiency resulting in a total morphological transformation of the starting globular shaped grains into larger and thin flake-like shape grains. The flake-like shape grains created complex grain boundaries during the sintering process and controlled the fracturing behavior. **[S5]**

3. **I showed that the Si_3N_4 amount had significant influence on the milling efficiency** resulting in grains with different sizes and shapes. The addition of 0.33 wt% Si_3N_4 gives better milling efficiency results comparing to the 1 wt% Si_3N_4 addition. The intensive milling assured an optimal coverage of 316L stainless steel grains with Si_3N_4 submicrometer sized particles in both cases which in turn resulted in improved mechanical properties (higher hardness, strength, lower friction coefficient) compared to reference sample. **[S2, S3, S7].**

4. **I proved that the addition of Y_2O_3 nanosized particles improved the tribological properties of the 316L SS.** The addition of yttria nanosized particles reduce the wear rate of the 316L significantly. **[S6]**

5. **I proved that the CDS composites with nanosized ceramic particles (SiC and Si_3N_4) resulted better mechanical properties compared to the nanosized ceramic oxide particles (Y_2O_3).** The CDS composites are showing higher microhardness and higher flexural strength due to their more complex induced microstructures and more efficient distribution to the grain boundaries of the matrix. **[S2, S3, S4, S5, S6].**

6. Research Achievements

6.1. Publications

[S1] H.R. Ben Zine, A. Horváth, K. Balázsi, C. Balázsi, Submicron sized sintered ODS steels prepared by high efficient attritor milling and spark plasma sintering, *Courrier Du Savoir* 24 (2017) 93-100.

[S2] H.R. Ben Zine, F. C. Sahin, Zs. E. Horváth, Zs. Czigány, Á. Horváth, K. Balázsi, C. Balázsi, Effect of Si_3N_4 addition on the morphological and structural properties of the 316L stainless steel for nuclear applications, *Resolution and Discovery* 2 (2017) 23-30.

[S3] H.R. Ben Zine, K. Balázsi, C. Balázsi, Effect of the α-Si_3N_4 addition on the tribological properties of 316L stainless steel prepared by attrition milling and spark plasma sintering, *Anyagok Világa (Materials World)* 1 (2018) 9-16.

[S4] H.R. Ben Zine, C. Balázsi, K. Balázsi, Study of the different ceramic additions effect on the 316L morphological properties during attrition milling , *Anyagok Világa (Materials World)* 1 (2018) 36-43.

[S5] H. R. Ben Zine, F. C. Sahin, Zs. Czigány, K. Balázsi, C. Balázsi, Novel SiC dispersion strengthened austenitic steels prepared by powder technology, *Archives of Metallurgy and Materials, (2019) accepted for publication* ***IF 0.7***

[S6] H. R. Ben Zine, K. Balázsi, C. Balázsi, The effect of the chemical composition to the end-properties of ceramic dispersed strengthened 316L/Y_2O_3 composites, *Periodica Polytechnica Chemical Engineering* 63 : 3 (2019) 370-377 ***IF 1.382***

[S7] C. Balázsi, H. R. Ben Zine, M. Furko, Z. Czigány, L. Almásy, V. Ryukhtin, H. Murakami, G. Göller, O. Yucel, F.C. Sahin, K. Balázsi, S. Kobayashi, A. Horváth, Microstructural and magnetic characteristics of ceramic dispersion strengthened sintered stainless steels after thermal ageing, *Fusion Engineering and Design* 145 (2019) 46-53 ***IF 1.437***

6.2. Oral presentations

H.R. Ben Zine, C. Balázsi, K. Balázsi, A. Horváth, **Sixieme ecole sur les techniques de caracterisation des materiaux,** Biskra University12-13 March 2016, Algeria.

H.R. Ben Zine, C. Balázsi, K. Balázsi, A. Horváth, Development of nanostructured ODS steels by powder technology, **NEA International Workshop on Structural Materials for Innovative Nuclear Systems**, 11-14 July 2016, Manchester, UK.

H. R. Ben Zine, Zs. Cigány, F. S. Cinar, A. Horváth, K. Balázsi, C. Balázsi, The first seminar on "thin films and their applications" at Mohamed Khider University, 16 April 2017, Biskra, Algeria.

H. R. Ben Zine, Zs. Cigány, F. S. Cinar, A. Horváth, K. Balázsi, C. Balázsi, Si_3N_4 dispersion strengthened 316L stainless steels: structural and mechanical properties, **International Conference Deformation and Fracture in PM Materials**, 22 – 25 October 2017, High Tatras, Slovakia.

H.R. Ben Zine, F.S. Cinar, O. Yucel, K. Balázsi, A. Horváth, C. Balázsi, Preparation and Investigation of Boron Nitride Dispersion Strengthened Steels, **14th International Symposium on Novel and Nano Materials,** 3-8 July 2016, Budapest, Hungary.

H. R. Ben Zine, Zs. Cigány, F. S. Cinar, A. Horváth, K. Balázsi, C. Balázsi, 316L austenitic steel preparation with ceramic addition, **MMT2017,** 13 May 2017, Siófok, Hungary.

H. R. Ben Zine, Zs. Cigány, F. S. Cinar, Á. Horváth, K. Balázsi, C. Balázsi, Study of Si_3N_4 addition effect on structural and mechanical properties of the 316l stainless steel, **17thPhD Students Materials Science Day",** 4 December 2017, Pannon University, Veszprém, Hungary.

H. R. Ben Zine, Zs. Cigány, F. S. Cinar, A. Horváth, K. Balázsi, C. Balázsi , Preparation and characterization of ODS steels, **"Fine ceramics day" event of Hungarian Scientific Society of Silicate Industry,** 9 April 2018, MTA EK, Budapest, Hungary.

H. R. Ben Zine, K. Balázsi, C. Balázsi, Investigation of silicon carbide dispersion strengthened austenitic steels, **FEMS Junior Euromat**, 08-12 July 2018, Budapest, Hungary.

H. R. Ben Zine, K. Balázsi, C. Balázsi, Investigation of ceramic particle dispersion strengthened austenitic steel, **2nd "Fine ceramics day" event of Hungarian Scientific Society of Silicate Industry,** 19/03/2019, Budapest, Hungary.

6.3. Posters

H.R. Ben Zine, C. Balázsi, K. Balázsi, A. Horváth, Development of nanostructured ODS steels by powder technology, **NEA International Workshop on Structural Materials for Innovative Nuclear Systems**, 11-14 July 2016, Manchester, UK.

H. R. Ben Zine, Zs. Cigány, F. S. Cinar, A. Horváth, K. Balázsi, C. Balázsi, Effect of ceramic addition on structural and mechanical properties of steel alloys. ECERS 2017, Budapest, Hungary.

7. References

[1] J.L. Lin, K. Mo, D. Yun, Y. Miao, X. Liu, H. Zhao, D.T. Hoelzer, J.S. Park, J. Almer, G. Zhang, Z. Zhou, J. F. Stubbins, A.M. Yacout, (2016), "In situ synchrotron tensile investigations on 14YWT, MA957 and 9-Cr ODS alloys", J. of Nuclear Mat. 471, pp. 289-298. https://doi.org/10.1016/j.jnucmat.2015.10.049

[2] S. Ukai, T. YOSHITAKE, S. MIZUTA, Y. MATSUDAIRA, S. HAGI & T. KOBAYASHI, "Preliminary Tube Manufacturing of Oxide Dispersion Strengthened Ferritic Steels with Recrystallized Structure", J. Nucl. Sci. Technol., 36, pp. 710-712, 2012. https://doi.org/10.1080/18811248.1999.9726259

[3] D. K. Mukhopadhyay, F. H. Froes, D. S. Gelles, "Development of oxide dispersion strengthened ferritic steels for fusion, J Nuclear. Mat., vols. 258-263, pp. 1209-1215. (1998). https://doi.org/10.1016/S0022-3115(98)00188-3

[4] R.L. Klueh, P.J. Maziasz, I.S. Kim, L. Heatherly, D.T. Hoelzer, N. Hashimoto, E.A. Kenik, K. Miyahara, "Tensile and creep properties of an oxide dispersion-strengthened ferritic steel", J. of Nuclear Mat. 307-311, pp. 773-777, (2002). https://doi.org/10.1016/S0022-3115(02)01046-2

[5] S. J. Zinkle, N. M. Ghoniem, "Operating temperature windows for fusion reactor structural materials", Fusion Eng. Des., vols. 51-52, pp. 55-71, (2000). https://doi.org/10.1016/S0920-3796(00)00320-3

[6] G. R. Odette, M.J. Alinger, B. D. Wirth, "Recent Developments in Irradiation-Resistant Steels", Annu. Rev. Mater. Res., vol. 38, pp. 471-503, (2008). https://doi.org/10.1146/annurev.matsci.38.060407.130315

[7] Y. Guerin, G. S. Was, S. J. Zinkle, "Materials challenges for advanced nuclear energy systems" MRS Bull., vol. 34, 2009, p. 10-14, (2009). https://doi.org/10.1017/S0883769400100028

[8] C. L. Chen, A. Richter, R. Kögler, G. Talut "Dual beam irradiation of nanostructured FeCrAl oxide dispersion strengthened steel", J. of Nuclear Mat., 412, Issue 3, pp. 350-358(2011). https://doi.org/10.1016/j.jnucmat.2011.03.041

[9] Duffy, DM. Fusion power: a challenge for materials science, Philos. Trans. R. Soc. A, vol. 368, 2010, p. 3315-3328(2010). https://doi.org/10.1098/rsta.2010.0060

[10] H. Sakasegawa, M. Tamura, S. Ohtsuka, "Precipitation behavior of oxide particles in mechanically alloyed powder of oxide-dispersion-strengthened steel", J. Alloys & Compounds,

vol. 452, no. 1, p. 2-6, (2008). https://doi.org/10.1016/j.jallcom.2007.01.177

[11] https://www.azom.com/article.aspx?ArticleID=863

[12] Karthik Desu, R.; Krishnamurthy, H. N.; Balu, A.; Kumar Gupta, A.; Kumar Singh, S. Mechanical properties of Austenitic Stainless Steel 304L and 316L at elevated temperatures, Mater. Res. Techn. 2016, 5, 13-20. https://doi.org/10.1016/j.jmrt.2015.04.001

[13] Biehler, J.; Hoche, H.; Oechsner, Corrosion properties of polished and shot-peened austenitic stainless steel 304L and 316L with and without plasma nitriding, M. Surf. Coat. Technol. 2017, 313, 40-46. https://doi.org/10.1016/j.surfcoat.2017.01.050

[14] Li, H. L.; Liu, D.; Yan, Y. T.; Guo, N.; Feng, J. C, Microstructural characteristics and mechanical properties of underwater wet flux-cored wire welded 316L stainless steel joints, J. Mater. Process. Technol. 2016, 238, 423-430. https://doi.org/10.1016/j.jmatprotec.2016.08.001

[15] S.J. Wang T. Jozaghi, I. Karaman, R. Arroyave, Y.I.Chumlyakov, Hierarchical evolution and thermal stability of microstructure with deformation twins in 316 stainless steel, Materials Science & Engineering A 694 (2017) 121-131 https://doi.org/10.1016/j.msea.2017.03.073

[16] Yinbin Miao, D. Gross, J. Sanders, J. Stubbins, Development of Austenitic ODS Strengthened Alloys for Very High Temperature Applications, Nuclear Energy University programs -final report- 22 April 2015.
DOI: 10.2172/1179825

[17] A. Farid, P. Feng, X. Du, A. S. Jawid, J. Tian, S. Guo, Microstructure and property evolution during the sintering of stainless steel alloy with Si3N4, Mat. Sci. and Eng. A 472 324-331 (2008). https://doi.org/10.1016/j.msea.2007.04.032

[18] Guo, P.; Zou, B.; Huang, C.; Gao, H, Study on microstructure, mechanical properties and machinability of efficiently additive manufactured AISI 316L stainless steel by high-power direct laser deposition, J. Mater. Process. Technol. 2017, 240, 12-22. https://doi.org/10.1016/j.jmatprotec.2016.09.005

[19] C. Suryanarayana and Nasser Al-Aqeeli, Mechanically alloyed nanocomposites, Progress in Materials Science 58 (2013) 383-502 https://doi.org/10.1016/j.pmatsci.2012.10.001

[20] L. Jinlong Y. Meng, H, Miura, L. Tongxiang, The effect of surface enriched chromium and grain refinement by ball milling on corrosion resistance of 316L stainless steel, Materials Research Bulletin 91 (2017) 91-97 https://doi.org/10.1016/j.materresbull.2017.03.022

[21] N. Kurgan and R. Varol, Mechanical properties of P/M 316L stainless, Powder Techn. 201 242-247 (2010). https://doi.org/10.1016/j.powtec.2010.03.041

[22] Zou J, Grasso S, Liu L-F, Ma H-B, Reece M, Binner M, "Flash spark plasma sintering of HfB2 ceramics without pre-sintering", Scripta Materialia 156, pp. 115- 119, 2018. https://doi.org/10.1016/j.scriptamat.2018.07.026

[23] Mahaseni ZH, Germi MD, Ahmadi Z, Asi MS, "Microstructural investigation of spark plasma sintered TiB2 ceramics with Si3N4 addition", Ceramics International 44 (11), pp. 13367-13372, 2018. https://doi.org/10.1016/j.ceramint.2018.04.171

[24] Velmurugan C, Senthilkumara V, Biswas K, Yadavbet S, "Densification and microstructural evolution of spark plasma sintered NiTi shape memory alloy," Advanced Powder Technology, 29 (10), pp. 2456-2462, 2018. https://doi.org/10.1016/j.apt.2018.06.026

[25] Lang E, Madden N, Smith C, Krogstad J, Allaain JP, "Microstructural and compositional effects of transition metal carbide additions on dispersion-strengthened tungsten fabricated via spark plasma sintering", International Journal of Refractory Metals and Hard Materials, 75, pp. 279-286, 2018. https://doi.org/10.1016/j.ijrmhm.2018.04.015

[26] Wei K and Nolas GS, "Enhanced thermoelectric properties of polymer/inorganic bulk composites through EG treatment and spark plasma sintering processing", Scripta Materialia, 150, pp. 70-73, 2018. https://doi.org/10.1016/j.scriptamat.2018.03.001

[27] Lucas R, Davis CE, Clegg WJ, Pizon D, Babonneau F, Foucaud S, Antou G, Maître A, "Elaboration of ZrCSiC composites by spark plasma sintering using polymerderived ceramics", Ceramics International, 40 (10), Part A, pp. 15703-15709, 2014. https://doi.org/10.1016/j.ceramint.2014.07.093

[28] Balázsi C, Gillemot F, Horváth M, Wéber F, Balázsi K, Cinar Sahin F, Onüralp Y, Horváth A, "Preparation and structural investigation of nanostructured oxide dispersed strengthened steels", Journal of Materials Science 46 (13) pp. 4598-4605, 2011. https://doi.org/10.1007/s10853-011-5359-1

[29] Nabeel Jahanzeb, J. Shin, J. Singh, Y. Heo, S. Choia, Effect of microstructure on the hardness heterogeneity of dissimilar metal joints between 316L stainless steel and SS400 steel, Mat. Sci. & Eng. A 700 338-350 (2017). https://doi.org/10.1016/j.msea.2017.06.002

[30] Ankur K. Agrawal and Aparna Singh, Limitations on the hardness increase in 316L stainless steel under dynamic plastic deformation, Mat. Sci. & Eng. A 687 306-312 (2017). https://doi.org/10.1016/j.msea.2017.01.066

[31] Jenő Gubicza, M. El-Tahawy, Y. Huang, H. Choi, H. Choe, J. L.Lábár, T. G. Langdon, Microstructure, phase composition and hardness evolution in 316L stainless steel processed by high-pressure torsion, Mat. Sci. & Eng. A 657 215-223 (2016). https://doi.org/10.1016/j.msea.2016.01.057

[32] Ziętala, T. Durejko, M. Polański, I. Kunce, T. Płociński, W. Zieliński, M. Łazińska, W. Stępniowski, T. Czujko, K. J. Kurzydłowski, Z. Bojara, The microstructure, mechanical properties and corrosion resistance of 316 L stainless steel fabricated using laser engineered net shaping M. Mat. Sci. Eng. A 2016, 677, 1-10. https://doi.org/10.1016/j.msea.2016.09.028

[33] Yadollahi, A.; Shamsaei, N.; Thompson, S. M.; Seely, D. W. "Effects of process time interval and heat treatment on the mechanical and microstructural properties of direct laser deposited 316L stainless steel", Mat. Sci. Eng. A 2015, 644 171-183. https://doi.org/10.1016/j.msea.2015.07.056

[34] Zhong, Y.; Rannar, L.-E.; Liu, L.; Koptyug, A.; Wikman, S.; Olsen, J.; Cui, D.; Shen, Z." Additive manufacturing of 316L stainless steel by electron beam melting for nuclear fusion applications", J. Nucl. Mater. 2017, 486, 234-245. https://doi.org/10.1016/j.jnucmat.2016.12.042

[35] Lavery, N. P.; Cherry, J.; Mehmood, S.; Davies, H.; Girling, B.; Sackett, E.; Brown, S. G. R.; Sienz, "Effects of hot isostatic pressing on the elastic modulus and tensile properties of 316L parts made by powder bed laser fusion", J. Mat. Sci. Eng. A 2017, 693, 186-213. https://doi.org/10.1016/j.msea.2017.03.100

[36] Hajian, M.; Abdollah-zadeh, A.; Rezaei-Nejad, S. S.; Assadi, H.; Hadavi, S. M. M.; Chung, K.; Shokouhimehr, M. "Microstructure and mechanical properties of friction stir processed AISI 316L stainless steel" Mater. Des. 2015, 67, 82-94. https://doi.org/10.1016/j.matdes.2014.10.082

[37] K. Saeidi, M.Neikter, J. Olsen, Z. J. Shen, F.Akhtar, "316L stainless steel designed to withstand intermediate temperature", Mat. and Design 135 1-8 (2017). https://doi.org/10.1016/j.matdes.2017.08.072

[38] Jinhua Yang, J. Trapp, Q. Guo, B. Kieback, “Joining of 316L stainless steel by using spark plasma sintering method”, Materials and Design 52, 179-189 (2013). https://doi.org/10.1016/j.matdes.2013.04.091

[39] A. B. Kale, A. Bag, J. Hwang, E. G.Castle, M. J. Reece, S. Choi, The deformation and fracture behaviors of 316L stainless steels fabricated by spark plasma sintering technique under uniaxial tension, Mat. Sci. & Eng. A 707, 362-372 (2017). https://doi.org/10.1016/j.msea.2017.09.058

[40] Keller, C.; Tabalaiev, K.; Marnier, G.; Noudem, J.; Sauvage, X.; Hug, E.” Influence of spark plasma sintering conditions on the sintering and functional properties of an ultra-fine grained 316L stainless steel obtained from ball-milled powder”, Mat. Sci. Eng. 2016, A665, 125-134. https://doi.org/10.1016/j.msea.2016.04.039

[41] Chao Tan, C. Wang, S. Wang, G. Wang, L. Ji, Y. Tong, X. Duan, “Investigation on 316L/316L-50W/W plate functionally graded materials fabricated by spark plasma sintering” Fusion Eng. and Des. 125 171-177 (2017). https://doi.org/10.1016/j.fusengdes.2017.08.001

[42] Suryawanshia, J.; Prashanth, K. G.; Ramamurtya, U. “Mechanical behavior of selective laser melted 316L stainless steel”, Mat. Sci. Eng. A 2017, 696, 113-121. https://doi.org/10.1016/j.msea.2017.04.058

[43] Röttger, A.; Geenen, K.; Windmann, M.; Binner, F.; Theisen,” Comparison of microstructure and mechanical properties of 316 L austenitic steel processed by selective laser melting with hot-isostatic pressed and cast material”, W. Mat. Sci. Eng. A 2016, 678, 365-376. https://doi.org/10.1016/j.msea.2016.10.012

[44] Miranda, G.; Faria, S.; Bartolomeu, F.; Pinto, E.; Madeira, S.; Mateus, A.; Carreira, P.; Alves, N.; Silva, F. S.; Carvalho, O. “Predictive models for physical and mechanical properties of 316L stainless steel produced by selective laser melting”, Mat. Sci. Eng. 2016, A657, 43-56. https://doi.org/10.1016/j.msea.2016.01.028

[45] J. D. Majumdar, A. Kumar, L. Li, “Direct laser cladding of SiC dispersed AISI 316L stainless steel” Trib. Inter. 42, 750-753 (2009). https://doi.org/10.1016/j.triboint.2008.10.016

[46] Kishore Kumar P, Sai NV, Krishna AG, "Effect of Y2O3 addition and cooling rate on mechanical properties of Fe-24Cr-20Ni-2Mn steels by powder metallurgy route", Composites Communications, 10, pp. 116-121, 2018. https://doi.org/10.1016/j.coco.2018.09.003

[47] Yang J, Trapp J, Guo Q, Kieback B, "Joining of 316L stainless steel by using spark plasma sintering method", Materials & Design (1980-2015), 52, pp. 179-189, 2013. https://doi.org/10.1016/j.matdes.2013.04.091

[48] Raja A, Upadhyaya A, Agrawal DK, "Effect of heating mode and Y2O3 addition on electrochemical response on austenitic and ferritic stainless steels, Corrosion Engineering", Science and Technology 50 (2), pp. 91-102 , 2015. https://doi.org/10.1179/1743278214Y.0000000176

[49] Peruzzo M, Beux TD, Ordoñez MFC, Souza RM, Farias CM, "High-temperature oxidation of sintered austenitic stainless steel containing boron or yttria", Corrosion Science 129, pp. 26 - 37, 2017. https://doi.org/10.1016/j.corsci.2017.09.002

[50] Verhiestade K, Mullens S, De Wispelaere N, Claessens S, DeBremaecker A, Verbeken K, "Nano-yttria dispersed stainless steel composites composed by the 3 dimensional fiber deposition technique", Journal of Nuclear Materials Volume 428 (1-3), pp. 54 - 64, 2012. https://doi.org/10.1016/j.jnucmat.2012.01.025

[51] Verhiest K, Almazouzi A, DeWispelaere N, Petrov R, Claessens R, "Development of oxides dispersion strengthened steels for high temperature nuclear reactor applications", Journal of Nuclear Materials, 385(2), pp. 308-311, 2009. https://doi.org/10.1016/j.jnucmat.2008.12.006 https://doi.org/10.1016/j.jnucmat.2008.12.006

[52] Lindau R, Möslang A, Schirra M, Schlossmacher P, Klimenkov M, "Mechanical and microstructural properties of a hipped RAFM ODS-steel", Journal of Nuclear Materials, 307-311, pp. 769- 772, 2002. https://doi.org/10.1016/S0022-3115(02)01045-0

[53] Baek S-W, Song EJ, Hyun Kim J, Lee Y-H, Ryu KS, Kim S-W, "Hydrogen susceptibility of nano-sized oxide dispersed austenitic steel for fusion reactor", Fusion Engineering and Design, 121, pp. 105 - 110, 2017. https://doi.org/10.1016/j.fusengdes.2017.06.027 https://doi.org/10.1016/j.fusengdes.2017.06.027

[54] Hutař P, Kuběna I, Ševčík M, Šmíd M,Kruml T, Náhlíka L, "Small fatigue crack propagation in Y2O3 strengthened steels", Journal of Nuclear Materials, 452(1-3), pp. 370-377, 2014. https://doi.org/10.1016/j.jnucmat.2014.05.071

[55] Kumar PK, Sai NV, Krishn AG, "Effect of Y2O3 and ZrO2 on the microstructure and mechanical properties of nano-ODS 21Cr-9Mn-6Ni steels", Materials and technology 52 (4), pp. 493-497, 2018. UDK 67.017:620.3:669.1 https://doi.org/10.17222/mit.2017.199

[56] Sun D, Liang C, Shang J, Yin J, Song Y, Li W, Liang T, Zhang X, "Effect of Y2O3 contents on oxidation resistance at 1150 ◦C and mechanical properties at room temperature of ODS Ni-20Cr-5Al alloy", Applied Surface Science, 385, pp- 587 - 596, 2016. https://doi.org/10.1016/j.apsusc.2016.05.143

[57] A.J. London, S. Santra, S. Amirthapandian, B.K. Panigrahi, R.M. Sarguna, S. Balaji, R. Vijay, C.S. Sundar, S. Lozano-Perez, C.R.M. Grovenor, "Effect of Ti and Cr on dispersion, structure and composition of oxide nano-particles in model ODS alloys", Acta Materialia 97, pp. 223-233(2015).
https://doi.org/10.1016/j.actamat.2015.06.032

[58] T. Liu, H. Shen, C. Wang, W. Chou, "Structure evolution of Y2O3 nanoparticle/Fe composite during mechanical milling and annealing", Prog. in Natural Sci.: Mat. Int., 23(4), pp. 434-439(2013).
https://doi.org/10.1016/j.pnsc.2013.06.009

[59] H. Zhang, Y. Huang, H. Ning, C. A.Williams, A. J.London, K. Dawson, Z. Hong, M.J. Gorley, C. R.M.Grovenor, G. J.Tatlock, S.G. Roberts, M. J.Reece, H. Yan, P.S. Granta, "Processing and microstructure characterisation of oxide dispersion strengthened Fe-14Cr-0.4Ti-0.25Y2O3 ferritic steels fabricated by spark plasma sintering", J. of Nuclear Mat. 464, pp. 61-68, (2015).
https://doi.org/10.1016/j.jnucmat.2015.04.029

[60] H. Oka, M. Watanabe, S. Ohnuki, N. Hashimoto, S.Yamashita, S. Ohtsuka, “Effects of milling process and alloying additions on oxide particle dispersion in austenitic stainless steel”, Journal of Nuclear Materials 447 (2014) 248-253
https://doi.org/10.1016/j.jnucmat.2014.01.025

[61] Farid Akhtar, L. Ali, F. Peizhong, J.A. Shah, “Enhanced sintering, microstructure evolution and mechanical properties of 316L stainless steel with MoSi2 addition”, J. of Alloys and Comp. 509 8794- 8797 (2011).
https://doi.org/10.1016/j.jallcom.2011.06.077

[62] C. Keller, K.Tabalaiev, G.Marnier, J.Noudem, X.Sauvage, E.Hug, “Influence of spark plasma sintering conditions on the sintering and functional properties of an ultra-fine grained 316L stainless steel obtained from ball milled powder”, Materials Science & Engineering A665(2016)125-134
https://doi.org/10.1016/j.msea.2016.04.039

[63] B. AlMangour, D. Grzesiak, J. Yang, “In situ formation of TiC-particle-reinforced stainless steel matrix nanocomposites during ball milling: Feedstock powder preparation for selective laser melting at various energy densities”, Powder Technology 326 (2018) 467-478
https://doi.org/10.1016/j.powtec.2017.11.064

[64] C. Tan, C. Wang, S. Wang, G. Wang, L. Ji, Y. Tong, X. Duan, "Investigation on 316L/316L-50W/W plate functionally graded materials fabricated by spark plasma sintering", Fusion Engineering and Design 125 (2017) 171-177 https://doi.org/10.1016/j.fusengdes.2017.08.001

[65] C. Tan, G. Wang, L. Ji, Y. Tong, X. Duan, "Investigation on 316L/W functionally graded materials fabricated by mechanical alloying and spark plasma sintering", Journal of Nuclear Materials 469 (2016) 32- 38 https://doi.org/10.1016/j.jnucmat.2015.11.024

[66] A.L. Garcia-Garcia, M.Alvarez-Vera, L.A.Montoya-Santiyanes, I.Dominguez-Lopez, J.L. Montes-Seguedo, J.C. Sosa-Savedra, J.D.O. Barceinas-Sanchez, "Regression models to predict the behavior of the coefficient of friction of AISI 316L on UHMWPE under ISO 14243-3 conditions", Journal of the Mechanical Behavior of Biomedical Materials 82 (2018) 248-256 https://doi.org/10.1016/j.jmbbm.2018.03.028

[67] J. Meng, N.H. Loh, B.Y. Tay, G. Fu, S.B. Tor, "Tribological behavior of 316L stainless steel fabricated by micro powder injection molding", Wear 268 (2010) 1013-1019 https://doi.org/10.1016/j.wear.2009.12.033

[68] F. Bartolomeu, M.Buciumeanu, E.Pinto, N.Alves, O.Carvalho, F.S.Silva, G.Miranda, "316L stainless steel mechanical and tribological behavior-A comparison between selective laser melting, hot pressing and conventional casting", Additive Manufacturing 16 (2017) 81-89 https://doi.org/10.1016/j.addma.2017.05.007

[69] Y. Li, Y. He, S. Zhang, X. He, W. Wang, B. Hua, Microstructures and tribological behaviour of oxynitrided austenitic stainless steel, Vacuum 146 (2017) 1-7 https://doi.org/10.1016/j.vacuum.2017.09.026

[70] D. Guan, X. He, R. Zhang, R. Li, X. Qu, "Tribological and corrosion properties of PM 316L matrix composites reinforced by in situ polymer-derived ceramics", Vacuum 148 (2018) 319-326 https://doi.org/10.1016/j.vacuum.2017.12.003

[71] P.F.Wang and Z.Han, "Friction and wear behaviors of a gradient nano-grained AISI 316L stainless steel under dry and oil-lubricated conditions", Journal of Materials Science and Technology, Volume 34, Issue 10, October 2018, Pages 1835-1842 https://doi.org/10.1016/j.jmst.2018.01.013

[72] Y. Wang, W. Yue, D. She, Z. Fu, H. Huang, J. Liu, "Effects of surface nanocrystallization on tribological properties of 316L stainless steel under MoDTC/ZDDP lubrications", Tribology International 79 (2014) 42-51. https://doi.org/10.1016/j.triboint.2014.05.021

[73] F. Rotundo, L.Ceschini, C.Martini, R.Montanari, A.Varone, “High temperature tribological behavior and microstructural modifications of the low-temperature carburized AISI 316L austenitic stainless steel”, Surface & Coatings Technology 258 (2014) 772-781. https://doi.org/10.1016/j.surfcoat.2014.07.081

[74] Robert E. Schilling and M. Yang, Attritor grinding mills and new developments, Western Coatings Federation Monthly Dinner Meetings, April 2000

[75] http://www.attritor.in/attritor_working.html

[76] Industrial Applications of Advanced Spark Plasma Sintering, American Ceramic Society Bulletin, Vol. 85, No. 2, February 2006

[77] M. Suárez, A. Fernández, J.L. Menéndez, R. Torrecillas, H. U. Kessel, J. Hennicke, R. Kirchner and T. Kessel, “Challenges and Opportunities for Spark Plasma Sintering: A Key Technology for a New Generation of Materials”, Sintering Applications, Burcu Ertuğ, IntechOpen, February 6th 2013. https://doi.org/10.5772/53706

[78] Jow-Lay Huang and Pramoda K. Nayak, Effect of Nano-TiN on Mechanical Behavior of Si3N4 Based Nanocomposites by Spark Plasma Sintering (SPS), Nanocomposites - New Trends and Developments, Farzad Ebrahimi, IntechOpen, (September 27th 2012). . https://doi.org/10.5772/50547

[79] W.R. Matizamhuka, Spark plasma sintering (SPS) - an advanced sintering technique for structural nanocomposite materials, the journal of the southern african institute of mining and metallurgy. Volume 116, December 2016. https://doi.org/10.17159/2411-9717/2016/v116n12a12

[80] Tokita, Masao. "Spark Plasma Sintering (SPS) Method, Systems, and Applications." Handbook of Advanced Ceramics (2013): 1149-1177. https://doi.org/10.1016/B978-0-12-385469-8.00060-5

[81] A.B. Spierings, M. Schneider, R. Eggenberger, (2011) "Comparison of density measurement techniques for additive manufactured metallic parts", Rapid Prototyping Journal, Vol. 17 Issue: 5.
https://doi.org/10.1108/13552541111156504

[82] R. P. Taylor, S. T. McClain & J. T. Berry (1999) Uncertainty analysis of metalcasting porosity measurements using Archimedes' principle, International Journal of Cast Metals Research, 11:4, 247-257, https://doi.org/10.1080/13640461.1999.11819281

[83] G. Farges and D. Degout, interpretation of the indentation size effect in vickers microhardness measurements-absolute hardness of materials, thin solid films, 181 (1989) 365-374.
https://doi.org/10.1016/0040-6090(89)90505-1

[84] C. Chuenarrom, P. Benjakul; P. Daosodsai, "Effect of indentation load and time on knoop and vickers microhardness tests for enamel and dentin", Mat. Res. vol.12 no.4 São Carlos 2009 https://doi.org/10.1590/S1516-14392009000400016

[85] http://me.aut.ac.ir/staff/solidmechanics/alizadeh/Hardness%20Test.htm

[86] I. Hutchings and P. Shipway, Tribology: Friction and Wear of Engineering Materials second edition, April 2017 https://doi.org/10.1016/B978-0-08-100910-9.00003-9

[87] M.Woydt and K.H. Habig, "high temperature tribology of ceramics", Tribology International, Volume 22, Issue 2, April 1989, Pages 75-88 https://doi.org/10.1016/0301-679X(89)90168-0

[88] F.Mujika, "On the difference between flexural moduli obtained by three-point and four-point bending tests", Polymer Testing,Volume 25, Issue 2, April 2006, Pages 214-220. https://doi.org/10.1016/j.polymertesting.2005.10.006

[89] S. A. Rodrigues Junior, J. L.Ferracane, Á.D. Bona, "Flexural strength and Weibull analysis of a microhybrid and a nanofill composite evaluated by 3- and 4-point bending tests", Dental Materials, Volume 24, Issue 3, March 2008, Pages 426-431 https://doi.org/10.1016/j.dental.2007.05.013

[90] M. Abd Mutalib, M.A.Rahman, M.H.D.Othman, A.F.Ismail, J.Jaafar, "Chapter 9 - Scanning Electron Microscopy (SEM) and Energy-Dispersive X-Ray (EDX) Spectroscopy", Membrane Characterization, 2017, Pages 161-179 https://doi.org/10.1016/B978-0-444-63776-5.00009-7

[91] Ray F. Egerton, Physical Principles of Electron Microscopy: An Introduction to TEM, SEM, and AEM, ISBN-10: 0-387-25800-0

[92] Nada MH (2015) Scanning Electron Microscopy. BAOJ Microbio 1: 005, 13 July, 2015 https://doi.org/10.24947/baojm/1/1/00105

[93] Bob Hafner, Energy Dispersive Spectroscopy on the SEM: A Primer, Characterization Facility, University of Minnesota-Twin Cities

[94] Bob Hafner, Scanning Electron Microscopy Primer, Characterization Facility, University of Minnesota-Twin Cities 4/16/2007

[95] John Goodge, Energy-Dispersive X-Ray Spectroscopy (EDS), University of Minnesota-Duluth

[96] Andrei A. Bunaciu, Elena gabriela Udriştioiu & Hassan Y. Aboul-Enein (2015) X-Ray Diffraction: Instrumentation and Applications, Critical Reviews in Analytical Chemistry, 45:4, 289-299, DOI: 10.1080/10408347.2014.949616 https://doi.org/10.1080/10408347.2014.949616

[97] B.J.Inkson, 2 - Scanning electron microscopy (SEM) and transmission electron microscopy (TEM) for materials characterization, Materials Characterization Using Nondestructive Evaluation (NDE) Methods 2016, Pages 17-43 https://doi.org/10.1016/B978-0-08-100040-3.00002-X

[98] B. AlMangour, D. Grzesiak, J. Yanga, "Selective laser melting of TiC reinforced 316L stainless steel matrix nanocomposites: Influence of starting TiC particle size and volume content ", Mat. and Design 104 141-151 (2016).
https://doi.org/10.1016/j.matdes.2016.05.018

[99] B. AlMangour, D. Grzesiak, T. Borkar, J. Yangd, "Densification behavior, microstructural evolution, and mechanical properties of TiC/316L stainless steel nanocomposites fabricated by selective laser melting" Mat. and Design 138 119-128 (2018).
https://doi.org/10.1016/j.matdes.2017.10.039

[100] J. W. Oh, S.K. Ryu, W.S. Lee, S.J. Park, "Analysis of compaction and sintering behavior of 316L stainless steel nano/micro bimodal powder", Powder Technology 322 1-8 (2017). https://doi.org/10.1016/j.powtec.2017.08.055

[101] K. Verhiest, S.Mullens, N.De Wispelaere, S.Claessens, A.DeBremaecker, K.Verbeken, "Nano-yttria dispersed stainless steel composites composed by the 3 dimensional fiber deposition technique", J. of Nucl. Mat. 428 54-64 (2012). https://doi.org/10.1016/j.jnucmat.2012.01.025

[102] M. Rafi Raza, F.Ahmad, M.A.Omar, R.M.German, "Effects of cooling rate on mechanical properties and corrosion resistance of vacuum sintered powder injection molded 316L stainless steel", J. of Mat. Proc. Tech. 212 164- 170 (2012).
https://doi.org/10.1016/j.jmatprotec.2011.08.019

[103] Z. Shuming, S. Xianfeng, Y. Jialin, T. Wenhua, W. Yingying, "Densification behavior and mechanical properties of nanocrystalline TiC reinforced 316L stainless steel composite parts

fabricated by selective laser melting", Optics and Laser Techn. 103 239-250 (2018). https://doi.org/10.1016/j.optlastec.2018.01.005

[104] B. AlMangour, D. Grzesiak, J. Yang, "In-situ formation of novel TiC-particle-reinforced 316L stainless steel bulk-form composites by selective laser melting", J. of Alloys and Comp. 706 409-418 (2017).
https://doi.org/10.1016/j.jallcom.2017.01.149

[105] X. Li, H.J. Willy, S. Chang, W. Lu, T.S. Herng, J. Ding," Selective laser melting of stainless steel and alumina composite: Experimental and simulation studies on processing parameters, microstructure and mechanical properties", Mat. and Design 145 1-10 (2018).
https://doi.org/10.1016/j.matdes.2018.02.050

[106] K. Park, J. Park, H. Kwon, "Fabrication and characterization of Al-SUS316L composite materials manufactured by the spark plasma sintering process", Mat. Sci. & Eng. A 691 8-15 (2017).
https://doi.org/10.1016/j.msea.2017.03.029

[107] D. Guan, X. He, R. Zhang, R. Li, X. Qu, "Tribological and corrosion properties of PM 316L matrix composites reinforced by in situ polymer-derived ceramics" Vacuum 148 319-326 (2018).
https://doi.org/10.1016/j.vacuum.2017.12.003

[108] Gao, R., Ge, W., Miao, S. Zhang T, Wang, X, Fang Q, Hot rolling and annealing effects on the microstructure and mechanical properties of ODS austenitic steel fabricated by electron beam selective melting", Frontiers of Materials Science, 10, pp. 73- , 2016.
https://doi.org/10.1007/s11706-016-0327-y